Gadolinium-148 and Other Spallation Production Cross Section Measurements for Accelerator Target Facilities

A Dissertation
Presented to
The Academic Faculty

by

Karen Corzine Kelley

In Partial Fulfillment
of the Requirements for the Degree
Doctor of Philosophy

Nuclear and Radiological Engineering
Georgia Institute of Technology
March 2004

Gadolinium-148 and Other Spallation Production Cross Section Measurements for Accelerator Target Facilities

Approved by:

Professor Nolan Hertel, Committee Chair	Professor John Wood (Physics)
Professor Chris Wang	Dr. Matthew Devlin (LANL)
Professor Ratib Karam	Dr. Eric Pitcher (LANL)

Date Approved: 17 March 2004

ACKNOWLEDGEMENTS

I would like to express my utmost gratitude to three individuals who made my graduate education successful. They have shown continued support, guidance, and encouragement during this work. To my advisor, Prof. Nolan Hertel, I am sincerely grateful for the opportunity to work with him. His expertise and advisement were essential. To my mentors at Los Alamos National Laboratory, Drs. Matt Devlin and Eric Pitcher, thank you for the endless hours of help with the irradiations and measurements, and countless discussions.

I wish to thank Prof. Donald Dudziak and Dr. Phillip Ferguson for urging me to continue my graduate education. Many thanks to Drs. Robert Haight, John Ullmann, Steve Wender, Guenter Muhrer, Gary Russell and technician Gregg Chaparro for insight and help with irradiations and measurements. I would also like to thank Stepan Mashnik for his discussions on CEM2k+GEM2.

To Tim, my husband and best friend, thank you for your continued love, support, and understanding of the pressures of graduate school.

To my parents, Rhonda and Bobby Peedin and Robert and Nancy Corzine, and family thank you for your unyielding love and support.

To Linn-Marie Nordh and Shannon McDaniel, thanks for all of your advice, both professionally and personally, and for lending an ear when I most needed it.

TABLE OF CONTENTS

LIST OF TABLES

LIST OF FIGURES

SUMMARY

At the Los Alamos Neutron Science Center accelerator complex, protons are accelerated to 800 MeV and directed to two tungsten targets, Target 4 at the Weapons Neutron Research facility and the 1L target at the Lujan Center. The Department of Energy requires hazard classification analyses to be performed on these targets and places limits on certain radionuclide inventories in the targets to avoid characterizing the facilities as "nuclear facilities." Gadolinium-148 is a radionuclide created from the spallation of tungsten. Allowed isotopic inventories are particularly low for this isotope because it is an alpha-particle emitter with a 75-year half-life. The activity level of Gadolinium-148 is low, but it encompasses almost two-thirds of the total dose burden for the two tungsten targets based on present yield estimates. From a hazard classification standpoint, this severely limits the lifetime of these tungsten targets. The cross section is not well-established experimentally and this is the motivation for measuring the Gadolinium-148 production cross section from tungsten.

In a series of experiments at the Weapons Neutron Research facility, Gadolinium-148 production was measured for 600- and 800-MeV protons on tungsten, tantalum, and gold. These experiments used 3 μm thin tungsten, tantalum, and gold foils and 10 μm thin aluminum activation foils. In addition, spallation yields were determined for many short-lived and long-lived spallation products with these foils using gamma and alpha spectroscopy and compared with predictions of the Los Alamos National Laboratory codes CEM2k+GEM2 and MCNPX.

The cumulative Gadolinium-148 production cross section measured from tantalum, tungsten, and gold for incident 600-MeV protons were 15.2±4.0, 8.31±0.92, and 0.591±0.155, respectively. The average production cross sections measured at 800 MeV were 28.6±3.5, 19.4±1.8, and 3.69±0.50 for tantalum, tungsten, and gold, respectively. These cumulative measurements compared best with Bertini and were within a factor of two to three of CEM2k+GEM2.

CHAPTER I

INTRODUCTION

"Fundamentally, you have a straightforward thesis." Prof. Nolan Hertel, 2002.

At present, no new nuclear reactors are being built in the United States, which leaves us with aging reactors that do not offer any great flexibility in neutron production. Therefore a new technology must be used to produce broad ranges of neutron sources. Accelerator-based facilities are fulfilling this goal with neutrons being produced by high-energy protons ($E \gtrsim 1$ GeV), including spallation of nuclei in a heavy metal target. Accelerators offer greater flexibility in terms of particle energies and types, which can lead to a variety of applications. Accelerator-based neutron scattering facilities in the U. S. currently in operation are the Los Alamos Neutron Science Center (LANSCE) at Los Alamos National Laboratory (LANL) in New Mexico and the Intense Pulsed Neutron Source at Argonne National Laboratory in Illinois. These facilities use tungsten and uranium, respectively, as accelerator targets. The Spallation Neutron Source (SNS) being built at Oak Ridge National Laboratory in Tennessee will provide North America with the most intense pulsed neutron beams using a liquid mercury target when it comes online, planned for 2006.

Spallation occurs when incident particles ($E \gtrsim 100$ MeV) interact with individual nucleons in the target nuclei and cause reactions, consisting of an intranuclear cascade and an evaporation-fission stage (Figure 1). The intranuclear cascade is initiated when incoming particles collide with individual nucleons, as opposed to the nucleus as a whole, leaving the nucleus in an excited state. The nucleus can relieve its excitation energy by processes of fission or evaporation of nucleons or small groups of nucleons until the excitation energy falls below the nucleon binding energy of several MeV, when gamma-ray emission removes the final few MeV of excitation energy. During the intranuclear cascade phase, several high-energy particles can leave the nucleus and initiate a spallation reaction in neighboring

nuclei, resulting in a 'fission-like' chain reaction process that eventually dies out when secondary particles no longer have enough energy to initiate a spallation event.

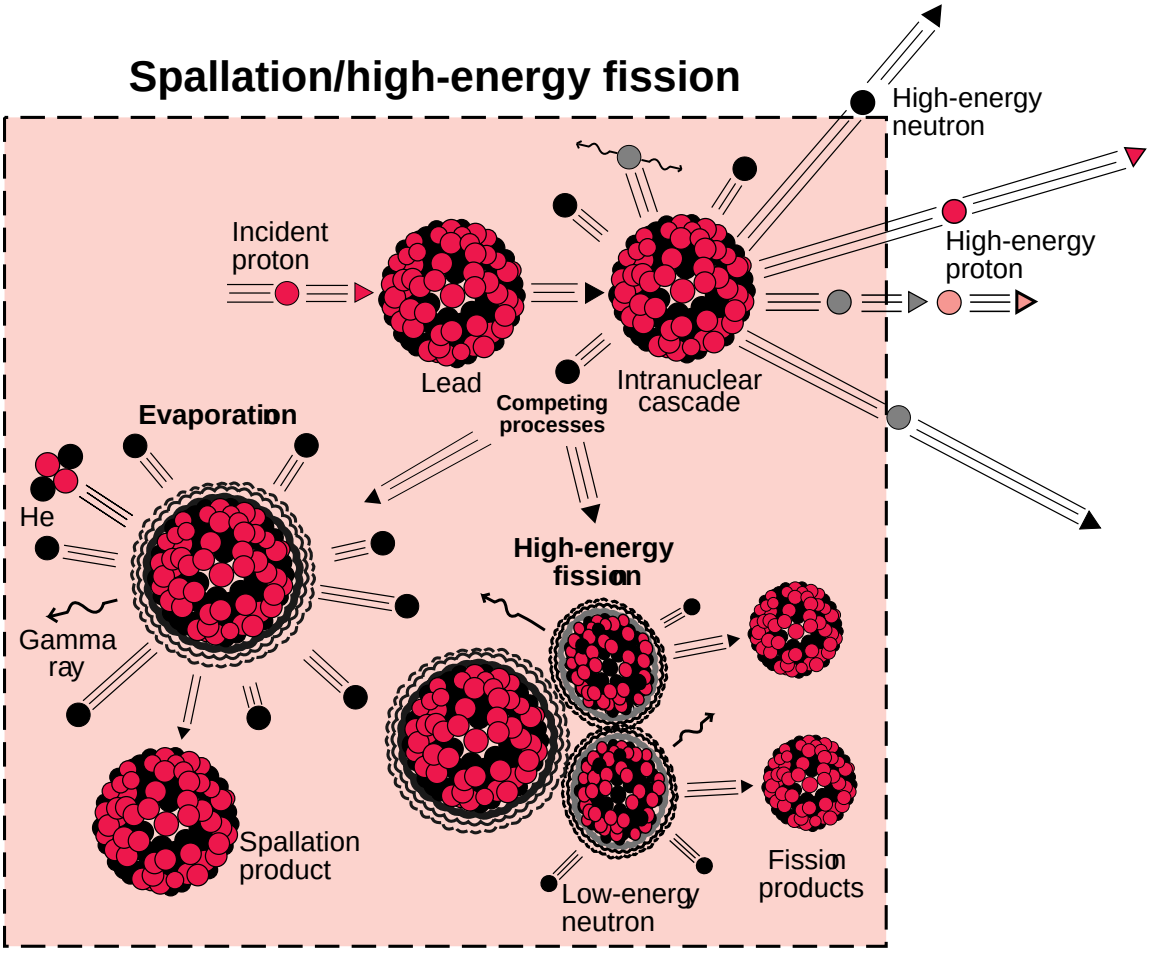

Figure 1: Spallation interaction processes

When heavy metal targets, such as tungsten, are bombarded with protons greater than a few hundred MeV, hundreds of different nuclides are produced, ranging from the atomic number of hydrogen to nuclides with atomic number just above that of the target material. These nuclides are both stable and radioactive and are created by spallation or secondary reactions with neutrons and other nuclear particles made in the target. These products are distributed somewhat heterogeneously throughout a thick target because of the energy dependence of the cross sections and energy loss of the proton beam within the target.

From this standpoint, it is difficult to measure nuclide production cross sections for a given energy proton in a thick target.

At the LANSCE accelerator complex, protons are accelerated to 800 MeV and directed to two tungsten targets, Target 4 at the Weapons Neutron Research (WNR) facility and 1L target at the Manuel Lujan Jr. Neutron Scattering Center (Figure 2). The U. S. Department of Energy (DOE) requires hazard classification analyses to be performed on these targets and places limits on radionuclide inventories in the targets as a means of determining the "nuclear facility" category level (Table 1) [1]. When a facility becomes a "nuclear facility," more engineering safeguards and administrative measures are required. So it is advantageous for a facility to maintain a low hazard classification. A Category-3 nuclear facility is considered to represent a low hazard, where there is only potential for "significant localized consequences" due to presence of radionuclides. The threshold values of radionuclide inventory of a Category-3 facility represent levels of material which, if released, would produce less than 10 rem effective whole body dose at 30 meters based on 24 hour exposure and no radioactive decay.

In an accident scenario, radiological inventory from one of the tungsten targets would be dispersed as a result of loss of cooling, oxidation of the target and dispersal with a 100% airborne release fraction. This accident scenario drives the hazard classification for the two tungsten targets at LANSCE. Presently, WNR Target 4 is a non-nuclear facility while the Lujan 1L target is classified as a Category-3 nuclear facility, one level above a non-nuclear facility. To be a non-nuclear facility, DOE requires the cumulative sum of all radionuclides produced in WNR's Target 4 to be less than 0.6 of the Category-3 threshold [2].

Table 1: Nuclide inventory limits for the 1L target [5].

nuclide	half-life	decay mode	Curies
53 I 131	8.04 d	β^-	1.3E-01
53 I 126	13.02 d	$\epsilon + \beta^+$, β^-	2.7E-01
53 I 124	4.18 d	$\epsilon + \beta^+$	7.6E-01
64 Gd 148	75 y	α	1.3E+00
53 I 125	60.14 d	ϵ	3.4E+00
75 Re 182b	64.0 h	$\epsilon + \beta^+$	6.8E+01
72 Hf 181	42.4 d	β^-	8.1E+01

(Table 1 continued)

nuclide	half-life	decay mode	Curies
75 Re 184	38.0 d	$\epsilon + \beta^+$	8.2E+01
63 Eu 145	5.94 d	$\epsilon + \beta^+$	1.0E+02
64 Gd 146	48.3 d	ϵ	1.1E+02
64 Gd 147	38.1 h	$\epsilon + \beta^+$	1.1E+02
64 Gd 153	242 d	ϵ	1.1E+02
63 Eu 147	24.1 d	$\epsilon + \beta^+$	1.4E+02
63 Eu 146	4.61 d	ϵ	1.5E+02
64 Gd 149	9.4 d	$\epsilon + \beta^+$	1.5E+02
65 Tb 151	17.6 h	$\epsilon + \beta^+$	1.6E+02
73 Ta 184	8.7 h	β^-	2.6E+02
66 Dy 155	10.0 h	$\epsilon + \beta^+$	2.7E+02
66 Dy 157	8.1 h	$\epsilon + \beta^+$	3.0E+02
66 Dy 159	144.4 d	ϵ	3.0E+02
72 Hf 172	1.87 y	ϵ	3.0E+02
75 Re 181	20 h	$\epsilon + \beta^+$	3.1E+02
68 Er 161	3.24 h	$\epsilon + \beta^+$	4.0E+02
71 Lu 172	6.70 d	$\epsilon + \beta^+$	4.0E+02
71 Lu 173	1.37 y	ϵ	4.7E+02
73 Ta 182	115.0 d	β^-	5.5E+02
69 Tm 167	9.24 d	ϵ	6.6E+02
70 Yb 166	56.7 h	ϵ	7.1E+02
69 Tm 166	7.70 h	$\epsilon + \beta^+$	7.3E+02
72 Hf 170	16.01 h	ϵ	7.6E+02
73 Ta 183	5.1 d	β^-	7.8E+02
71 Lu 169	34.06 h	$\epsilon + \beta^+$	8.0E+02
70 Yb 169	32.01 d	ϵ	9.3E+02
71 Lu 170	2.00 d	$\epsilon + \beta^+$	9.4E+02
73 Ta 173	3.65 h	$\epsilon + \beta^+$	9.5E+02
71 Lu 171	8.22 d	$\epsilon + \beta^+$	1.1E+03
73 Ta 174	1.2 h	$\epsilon + \beta^+$	1.1E+03
72 Hf 173	24.0 h	$\epsilon + \beta^+$	1.2E+03
74 W 177	135 m	$\epsilon + \beta^+$	1.2E+03
73 Ta 175	10.5 h	$\epsilon + \beta^+$	1.3E+03
72 Hf 175	70 d	ϵ	1.5E+03
73 Ta 176	8.08 h	$\epsilon + \beta^+$	1.6E+03
74 W 178	21.7 d	ϵ	2.0E+03
74 W 181	121.2 d	ϵ	5.7E+03
74 W 185	75.1 d	β^-	1.6E+04
74 W 187	23.9 h	β^-	3.4E+04

Gadolinium-148 is a radionuclide created from the spallation of tungsten and other heavy elements. Allowable isotopic inventories in the target are particularly low for this isotope

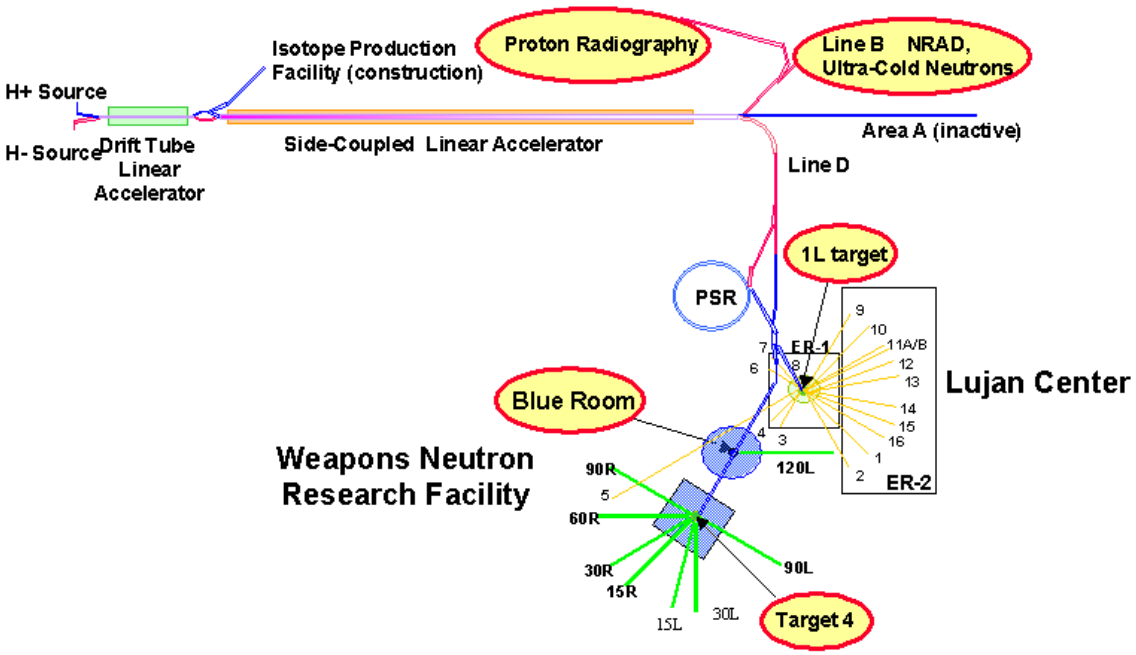

Figure 2: LANSCE accelerator complex, indicating the location of Target 4 at WNR and the 1L Target at the Lujan Center

($8.2\text{x}10^{-2}$ Ci for Category-3 threshold) because it is an alpha-particle emitter with a 75-year half-life. When α-particle emitters are inhaled, the emitted α particles deposit all of their energy locally, and, because of their high linear energy transfer have ten to twenty times the dose equivalent as β- and γ-rays depositing the same amount of energy. The activity level of ^{148}Gd is generally low, but it encompasses almost two-thirds of the total inhalation dose burden in an accident scenario for the two tungsten targets at LANSCE based on present yield estimates (Table 2) [3–5]. The total dose burden is defined as the sum of the acute dose from submersion in the radioactive aerosol plus the committed dose due to inhalation of the nuclides. From a hazard classification standpoint, this severely limits the irradiation lifetime of these tungsten targets.

As 800-MeV protons pass through the tungsten target at WNR and the upper tungsten target at the Lujan Center, the proton energy is degraded to 600 MeV upon exiting the target. Since the facility classification is partly driven by the inventory of ^{148}Gd, a better estimate of the true production rate in tungsten targets is needed.

Table 2: Committed Effective Dose Equivalent (CEDE) per Unit Release at 960 m from the 1L Target [5]

nuclide	CEDE at 960 m (Sv/Ci)	nuclide	CEDE at 960 m (Sv/Ci)
64 Gd 148	3.20E-02	69 Tm 167	1.08E-06
72 Hf 172	1.12E-04	64 Gd 149	8.28E-07
73 Ta 182	1.54E-05	66 Dy 159	8.28E-07
53 I 126	1.54E-05	64 Gd 147	6.53E-07
53 I 131	1.13E-05	71 Lu 169	5.75E-07
53 I 125	8.28E-06	73 Ta 184	5.39E-07
64 Gd 146	8.12E-06	72 Hf 170	3.33E-07
71 Lu 173	8.12E-06	73 Ta 176	3.31E-07
53 I 124	7.33E-06	65 Tb 151	3.15E-07
72 Hf 181	5.75E-06	69 Tm 166	3.15E-07
64 Gd 153	3.33E-06	75 Re 181	3.14E-07
70 Yb 169	2.87E-06	74 W 185	2.47E-07
72 Hf 175	2.11E-06	74 W 187	2.44E-07
71 Lu 172	2.09E-06	73 Ta 175	2.17E-07
75 Re 184	1.89E-06	72 Hf 173	1.66E-07
73 Ta 183	1.89E-06	73 Ta 173	1.55E-07
63 Eu 146	1.54E-06	66 Dy 155	1.15E-07
63 Eu 147	1.15E-06	74 W 178	1.12E-07
71 Lu 170	1.12E-06	68 Er 161	1.10E-07
71 Lu 171	1.12E-06	74 W 177	9.44E-08
75 Re 182b	1.12E-06	73 Ta 174	6.14E-08
63 Eu 145	1.12E-06	66 Dy 157	5.80E-08
70 Yb 166	1.08E-06	74 W 181	5.75E-08

From a basic nuclear physics standpoint, the ideal strategy would be to measure the ^{148}Gd production cross sections individually for each tungsten isotope. However, obtaining isotopically pure tungsten foils is costly. An alternative is to perform measurements with a mono-isotopic element with an atomic number close to that of tungsten (Z=74). Tantalum (Z=73), which is 99.988% ^{181}Ta, provides a good alternative for testing the physics models used to estimate spallation products at these energies. Furthermore, tantalum is used as target cladding materials at the KENS (Japan) and ISIS (United Kingdom) spallation neutron source facilities. These facilities operate at 500 MeV and 800 MeV, respectively. By measuring production from Ta, nuclear physics models can be used in conjuction with production cross section measurements from elemental W, to gain a better understanding of production rates for individual W isotopes. Gold, another monoisotopic element (Z=79), is also of interest to the Spallation Neutron Source project because of its proximity to mercury (Z=80), the candidate target material, in the periodic table. Therefore, measuring production from Ta and Au will help evaluate dose burdens at other spallation neutron source facilities, as well as test the physics models used to estimate spallation products.

CHAPTER II

BACKGROUND

"All models are wrong; some models are useful." Vic Reis

2.1 Theoretical predictions

Because the accuracy of predicting the cumulative ^{148}Gd production cross section by the available physics models is unknown, the procedure approved by DOE regulators for calculating the ^{148}Gd inventory in the targets requires the predicted value be multiplied by a factor of 1.5 in order to account for this uncertainty. The magnitude of this uncertainty factor further limits the lifetime of the target. Two LANL physics codes used for calculating nuclide production are MCNPX [6] and CEM2k+GEM2 [7, 8]. The three stages of spallation, the intranuclear cascade (INC), preequilibrium, and the fission/evaporation stage, all contribute to nuclide production in these codes and experimentally. A description of each code and their stages follows in the next sections.

2.1.1 MCNPX

MCNPX is a general purpose Monte Carlo radiation transport code that started as an extension of MCNP and LAHET. Monte Carlo n-Particle (MCNP) code transports neutrons from 10^{-11} to 20 MeV, photons from 1 keV to 100 GeV, and electrons from 1 keV to 1 GeV. [9]. Los Alamos High Energy Transport (LAHET) is the LANL modification of the HETC Monte Carlo code for transport and interaction of nucleons, pions, and muons, originally developed at Oak Ridge National Laboratory [10]. The LAHET portion of MCNPX has generally been used above 20 MeV. With the extension of tabular neutron cross-section data between 20 and 150 MeV for select nuclides of interest [11], the LAHET portion is now used above 150 MeV where it is more reliable. Below 150 MeV, tabular cross section data are used for neutron transport. For each feature in the portion of MCNPX above tabular

regions, there are typically at least two different physics models to choose from. The nuclide yields predicted by MCNPX depend on the physics models chosen to simulate high-energy (>150 MeV) nucleon interaction. For this reason, this study focuses on the default physics models of MCNPX: Bertini intranuclear cascade [12,13], the multi-stage preequilibrium exciton model (MPM) [14], Dresner evaporation with Gilbert-Cameron-Cook-Ignatyuk (GCCI) level density [15], and the Rutherford Appleton Laboratory (RAL) fission model [16].

The Bertini intranuclear cascade model describes the nucleon-nucleus interaction below 3.5 GeV and the pion-nucleon interaction below 2.5 GeV. Instead of tracking trajectories of individual nucleons, Bertini uses approximations, but has proven to be applicable for most design applications. The cascade model starts when an incident particle enters the nucleus at a point uniformly selected over the projection area. The total particle-particle cross sections and region-dependent nucleon densities are used to select a path length for the projectile particle. The momentum of the struck nucleon, the type of reaction, momentum, and scattering angle of the reaction product are then determined using statistical sampling. The particle interactions considered include scattering, charge exchange scattering (for π-nucleon reactions), production of π-mesons, and pion absorption. The cascade continues until the energy of the excited nucleus is $\sim$7 to 10 MeV above the Fermi breakup energy, a rather crude approximation. The Fermi breakup energy can be described in terms of the Pauli exclusion principle, which forbids interactions where the collision products would be in occupied states. For a Fermi gas, levels are filled starting from the lowest level. The Fermi breakup energy is the minimum energy allowed for the low-energy product of a collision, which corresponds to the lowest unfilled level of the system. Below the Fermi energy, particles are considered to be absorbed by the nucleus.

In the Bertini model, the density distribution inside the nucleus is described by three concentric spheres (one central sphere and two surrounding spherical shells), each with uniform density of neutrons and protons. The radii of the spheres are determined by distances at which the Fermi-type charge-distribution function reached various fractions of the central density. As cascade particles crossed region boundaries, they gained or lost kinetic energy in the amount in which the potential was more negative or less negative. Cascade particles

move through the nucleus with velocity greater than the velocity with which a disturbance is likely to be propagated. Most of the time, cascade particles pass through undisturbed nuclear matter.

The MPM preequilibrium model is invoked at the end of the INC with an initial hole-particle exchange, an excitation energy, and exciton number (sum of excited holes and pairs) determined by the INC. If this exciton number is greater than the equilibrium exciton number, then the further emission of fragments are simulated. At each stage, the excited nucleus may emit a neutron, proton, deuteron, triton, ^{3}He, or alpha particle and does not allow fission. The fragment kinetic energy, scattering angle (using isotropic angular distribution), and momentum are sampled by Monte Carlo techniques. The characteristics of the residual nucleus are then updated and the process repeats. The model ends when reaching the equilibrium exciton number, at which point an evaporation or Fermi-breakup model is applied to the residual nucleus with the remaining excitation energy.

In the Dresner evaporation model, energy is relieved by evaporation of n, p, d, t, ^{3}He, and α particles. The other option in the evaporation/fission stage is to use the Rutherford Appleton Laboratory (RAL) fission model by Atchison. This model allows fission for $Z \geq 71$ and has different routines for actinides ($Z \geq 89$) and subactinides ($71 \leq Z \leq 88$). For the actinide case, a fixed fission barrier of 6 MeV is used and the probability of fission is based solely on the charge of fissioning the nucleus, not on its energy. These approximations are based on experimental data. For subactinides, a statistical model is used with a probability of fission based fission barrier energy. Fission barriers are determined as differences between the saddle-point and ground state masses and are a function of A, Z, and excitation energies of fissioning nuclei. Only when a neutron is chosen for evaporation in the Dresner model is fission considered. Then, fission or evaporation is chosen according to the probability of fission. The subactinide fission routine has been determined to suppress fission for some subactinides at intermediate energies.

These physics models have been well accepted and used for many design applications in projects such as the Spallation Neutron Source (SNS), European Spallation Source (ESS),

and the Japanese Spallation Neutron Source (JSNS). These default physics models in MCNPX will hereafter be referred to as "Bertini."

2.1.2 CEM2k+GEM2

The Cascade Exciton Model (CEM) by Stepan Mashnik *et al.* has been merged with the Generalized Evaporation Model (GEM) code [17] by Furihata to become the CEM2k+GEM2 model. CEM was developed to describe the yields of spallation products and spectra of secondary nucleons. The intranuclear cascade model is based on the Boltzmann equation with two exceptions. The cascade particles and target-nucleus nucleons are considered as two different types of particles, and the collisions between particles of the same type are neglected. At each step in the cascade, the type of interaction, momentum, and scattering angle are decided by Monte Carlo techniques. Cascade particles are described by the equation of state for an ideal gas. The nuclear radial density is described by the Fermi distribution with two parameters taken from the analysis of electron-nucleus scattering. The nucleus is described by seven concentric spheres of equal density [18]. The end of the INC cascade in CEM is determined by a cutoff energy of 1 MeV above the Fermi breakup energy for incident energies above 150 MeV. The excited residual nucleus at the end of the INC determines the particle-hole configuration in the preequilibrium model, modified excition model (MEM) [19]. This preequilibrium model works similarly to MPM except that the equilibrium exciton number (sum of excited particles and holes) is determined by the probability of increasing energy equalling the probability of decreasing energy. The MPM only considers increasing energy. The level density model used is essentially the Ignatyuk model [20] modified by Sierk and Mashnik [21]. CEM2k also includes real binding energies, whereas Bertini uses 7 MeV.

Subsequent evaporation and fission takes place in GEM2. The GEM model is an extension and modification by Furihata of the evaporation and fission models used in MCNPX. One of the extensions includes the evaporation of up to 66 types of particles and fragments, compared to the six that are allowed in MCNPX, which increases the run time. The 66 types include naturally existing isotopes or isotopes close to the line of stability, with $Z \leq 12$,

and half-lives longer than 1 ms. The subactinide fission model is the same as that of Atchison. The actinide model was updated from the Atchison model with newer experimental fission-fragment mass distributions, charge distributions, and kinetic energy distributions. The GEM2 model was modified slightly for use with CEM2k by adjusting the level density parameter to yield the proper fission cross section. At the present time, some production reactions at the borders between fission and fragmentation or between fission and emission of heavy fragments like Na or Mg are poorly described. Otherwise CEM2k+GEM2 describes reasonably well many spallation, fission, and fragmentation reactions.

The independent production cross sections as a function of mass number for Bertini and CEM2k+GEM2 for 800-MeV protons interacting with tungsten are compared in Figure 3. There are two distinct humps, one for production by spallation without fission for higher masses and charge, and another for nuclide production by spallation followed by fission for lower masses and charge. In both mass and charge curves, ^{148}Gd does not have a significant contribution from fission and is produced by evaporation. In general, CEM2k+GEM2 has higher predictions for production than CEM2k+GEM2, with Bertini predicting higher yields only in the transition region from evaporation to fission. At the lower end of the curves, CEM2k+GEM2 predicts higher production cross sections for $Z \leq 10$ and $A \leq 20$ because the GEM2 evaporation/fission model includes up to 66 types of particles and fragments, compared to the six in Bertini.

2.2 Previous measurements

The ^{148}Gd inventory in a thick target is difficult to deduce because ^{148}Gd decays only by alpha-particle emission with no associated gamma-ray emission. To date, only one measurement of the number of ^{148}Gd atoms produced in tungsten has been made. A radiochemistry analysis, done as part of the APT Project decay heat experiment, measured the number of ^{148}Gd atoms in the center of three tungsten foils irradiated with 800-MeV protons [22,23]. Assuming that the isotope is only produced within the beam spot, a cumulative cross section of 16.40±0.41 mb can be inferred from this measurement. Cumulative

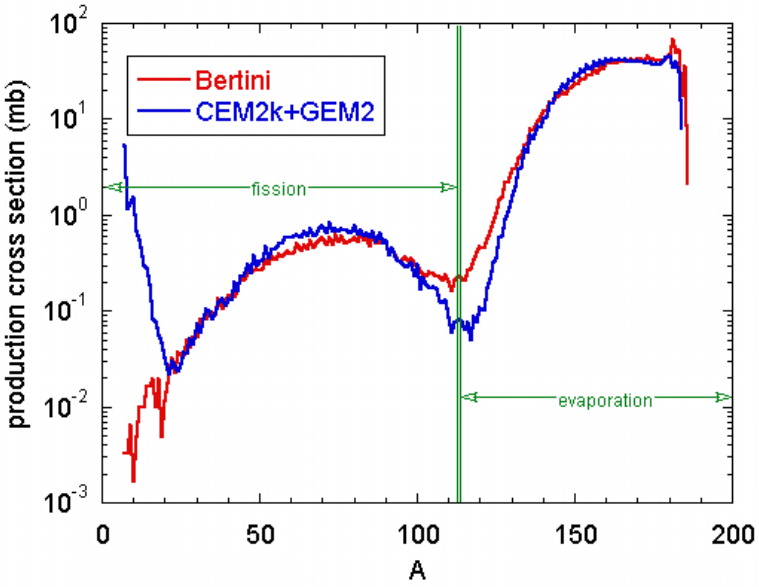

(a)

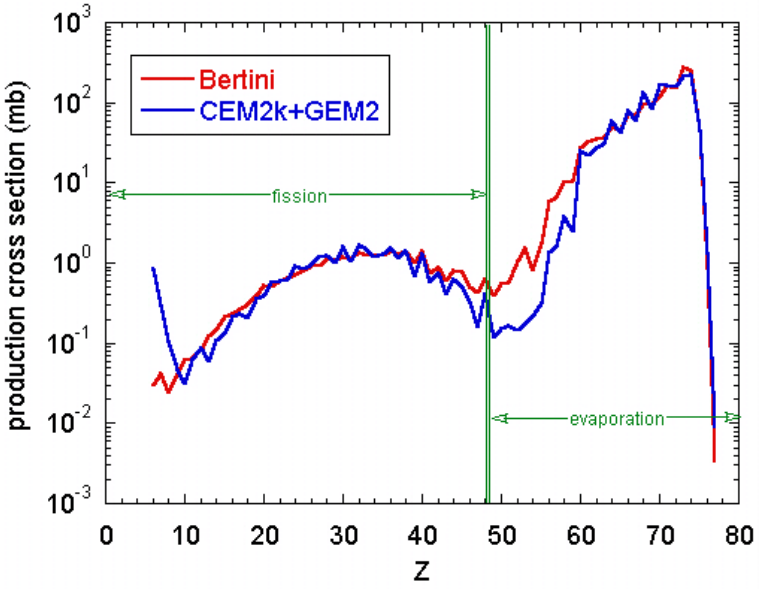

(b)

Figure 3: Production cross section curves of 800 MeV p + W for Bertini and CEM2k+GEM2 as a function of (a) mass and (b) charge.

yields include production from the decay of radioactive parents. Appendix A shows the decay scheme feeding ^{148}Gd with all the modes of decay and half-lives. A current theoretical estimate by CEM2k+GEM2 for cumulative production from tungsten is 41.38±0.39 mb at 800 MeV and 21.63±0.28 mb at 600 MeV. The Bertini model yields 20.87±1.59 mb at 800 MeV and 10.92±0.16 at 600 MeV for cumulative production from tungsten. A comparison of independent and cumulative production yields from CEM2k+GEM2, Bertini, and the APT measurement can be found in Figure 4. This figure shows that the independent ^{148}Gd production contribution is only 5 to 15% of the cumulative ^{148}Gd production for CEM2k+GEM2, whereas Bertini indicates that this contribution is 30 to 45%. The dominant factor between the cumulative ^{148}Gd production cross sections is the difference in ^{152}Er production (Table 3). Figure 5 shows the independent production cross sections as a function of product mass and Z for Z=64 to 72. These rare earth curves indicate that CEM2k+GEM2 typically predicts a higher cross section for the lower masses than Bertini for a given Z, whereas Bertini predicts a higher cross section for the higher masses for a given Z. These figures and tables demonstrate how different these two intranuclear cascade models are in calculating production yields for the rare earth metals.

Several other measurements of spallation product yields exist for intermediate-energy protons on W, Ta, and Au foils (Table 4) [24–33]. Previous measurements used gamma spectroscopy, radiochemical analysis, or a fragment separator to determine independent and cumulative spallation product yields. Bertini and CEM2k+GEM2 have been compared with some of these measurements and are generally within a factor of two of the measurement. For 800-MeV proton-irradiated ^{197}Au, a comparison was made between measurements at Gesellschaft fuer Schwerionenforschung (GSI) in Darmstadt, Germany; Institute for Theoretical and Experimental Physics (ITEP) in Russia; and Zentrum fuer Strahlenschutz und Radiooekologie Universitaet (ZSR) in Germany and the LAHET and CEM2k simulations [34]. There is general agreement between the measured data with an average mean squared deviation factor $< F >= 1.5$ [30]. However the agreement between simulations was much worse. The average $< F >$ for CEM2k compared with the three measurements was 2.1, and for LAHET was 2.8. It is important to note that the paper did

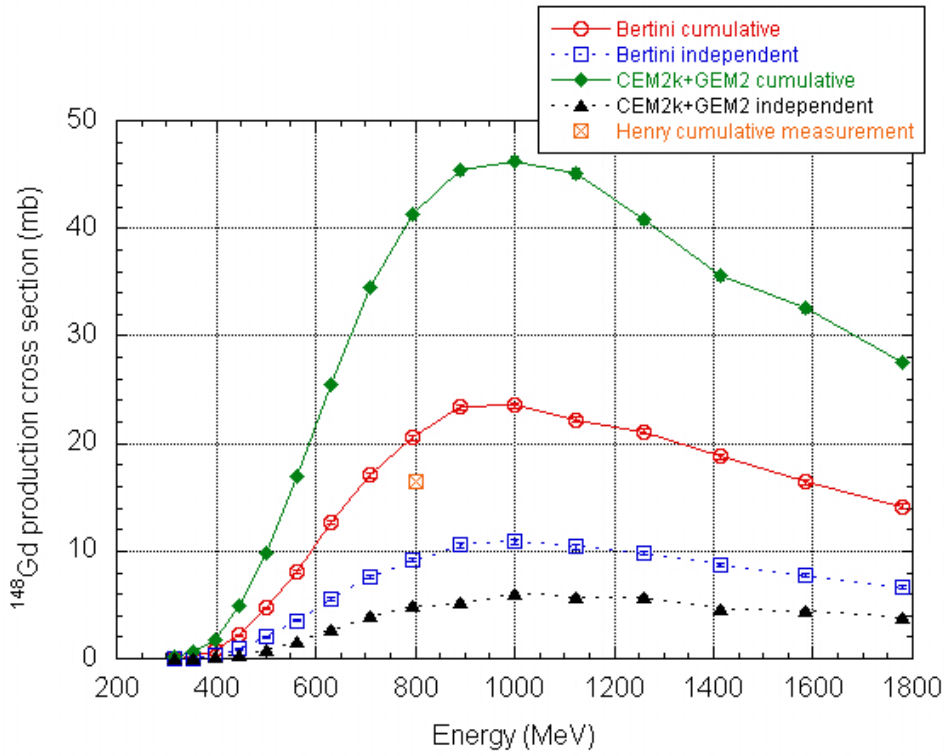

Figure 4: Calculated ^{148}Gd production cross sections for W(p,x)^{148}Gd by CEM2k+GEM2, Bertini in MCNPX, and an inferred measurement from APT [23]. Error bars are smaller than point ticks.

Table 3: Comparison of independent radionuclide production cross sections used in calculating the cumulative ^{148}Gd production cross sections from 800-MeV protons incident on tungsten for Bertini and CEM2k.

	% contribution	Independent cross section (mb)		Bertini/CEM2k
	to cumulative	Bertini	CEM2k	ratio
^{148}Gd	100	9.26±1.58	4.65±0.14	1.99
^{148}Tb	100	5.59±0.13	6.98±0.17	0.80
^{148}Dy	100	3.28±0.10	12.9±0.2	0.25
^{148}Ho	100	0.003±0.003	0.812±0.058	0.003
^{152}Dy	0.1	13.9±0.19	8.17±0.18	1.71
^{152}Ho	23.0	4.87±0.12	9.56±0.20	0.51
^{152}Er	91.2	1.72±0.07	13.7±0.2	0.13
^{152}Tm	91.2	0.003±0.003	0.428±0.042	0.006
^{156}Tm	0.007	3.08±0.09	7.07±0.17	0.44
^{156}Yb	9.13	0.455±0.035	9.52±0.20	0.048
^{156}Lu	86.6	0.000±0.000	0.093±0.019	0.00
^{160}Hf	0.064	0.011±0.005	1.11±0.07	0.010

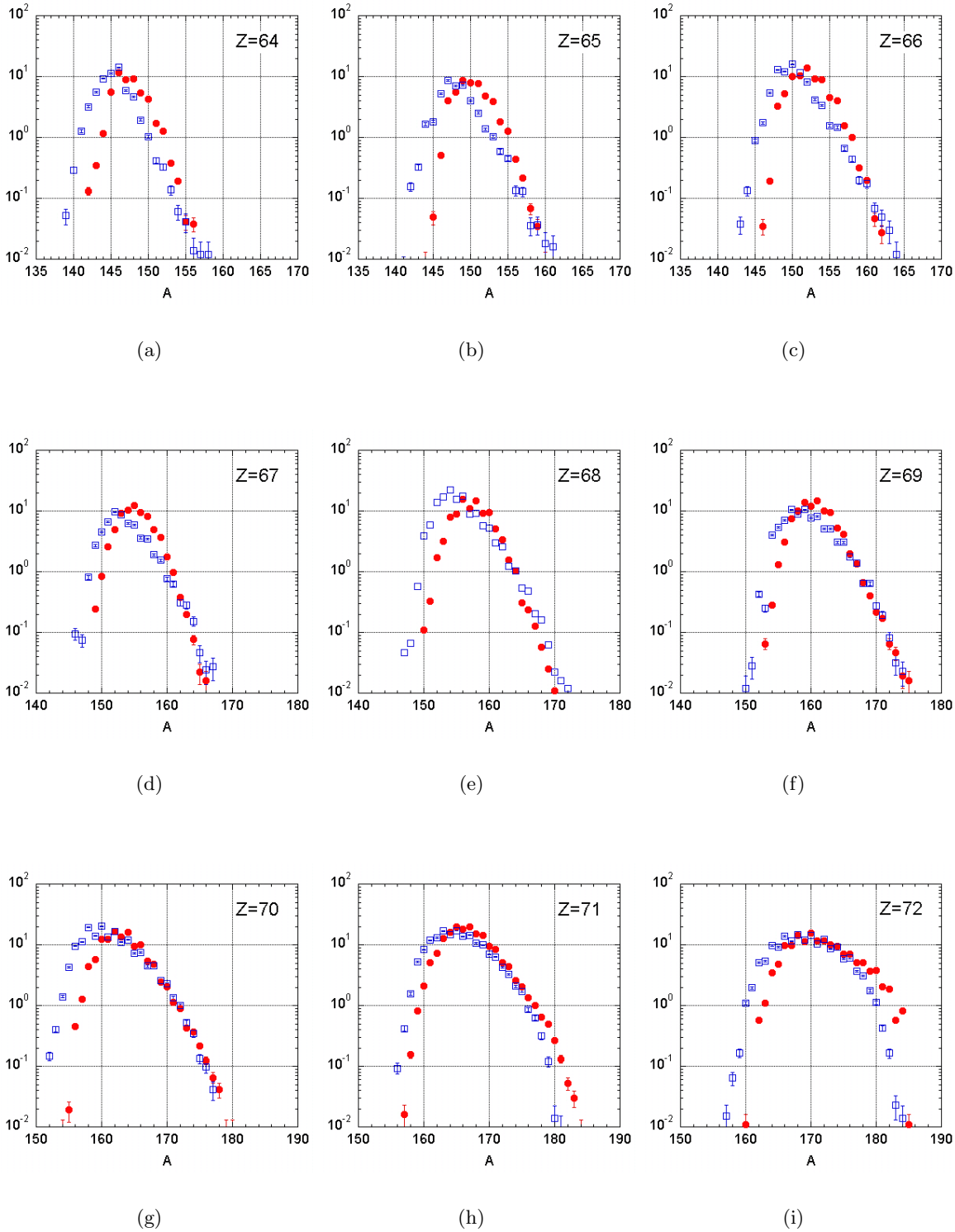

Figure 5: Independent radionuclide production curves from 800 MeV protons incident on tungsten for Z=64 to 72. Open blue squares represent CEM2k+GEM2 and red-filled circles represent Bertini.

not state which LAHET physics models were used, clouding the meaning of the LAHET comparison. Another simulation/measurement comparison paper by Mashnik et al. [35] found that in general the simulations were reasonable for most of the nuclides in the spallation region not far from the target nuclide. The predictive power in the low fission region is worse.

Table 4: Number of previous measurements of spallation product yields and their methods of analysis

Target Material	Energy (MeV)	γ spectroscopy	radiochemical analysis	fragment separator
Tungsten	500	1		
	800	2	1	
Tantalum	500	1		
	660		1	
	800		1	
Gold	500	1		
	550	1		
	580	1		
	660	1		
	760	1		
	800	1		2

CHAPTER III

METHODS

"...there are known knowns; there are things we know we know. We also know there are known unknowns; that is to say we know there are some things we do not know. But there are also unknown unknowns - the ones we don't know we don't know." –Donald Rumsfeld

In order to accurately assess the production of ^{148}Gd in a thick target within the incident proton range of 600 to 800 MeV, a series of thin or thick target experiments within the energy range of interest must be performed. There are several methods by which ^{148}Gd production can be determined. One method is a thick target experiment, where a cylindrical target similar to the ones at LANSCE is irradiated. The target would be cut into thin slices to determine production within small proton energy intervals since the initial proton energy is degraded as it passes through the target. The irradiated target would then be destructively assayed to determine quantities of isotopes produced. By measuring the production rate of ^{148}Gd as a function of depth in a target, the amount of this isotope created as a function of proton energy can be deduced. The primary drawback to this method is contamination by high-energy secondary protons.

Another method is to irradiate thin foils at specific proton energies to obtain production cross sections. Nuclear reaction models can then "tune" to more closely match the measured production cross section for an array of heavy metals (tungsten, tantalum, and gold). Thin foil experiments allow foils of different materials to be irradiated at the same time. Since the proton energy loss through each foil is negligible, all foils are essentially exposed to a single proton energy. Not only do the foils need to be thin enough to have negligible energy loss during irradiation, they also need to be thin enough for ^{148}Gd decay alphas to later escape and be detected. It was decided to use the thin foil method for measuring the ^{148}Gd production cross section because it could help evaluate dose burdens at spallation neutron source facilities, as well as provide the nuclear physics modeling community with

cumulative cross sections for a nuclide with mass well below the target nucleus mass.

3.1 ^{148}Gd production cross section derivation

In order to measure the W(p,x)^{148}Gd cross section, the ^{148}Gd production rate in the foil (R), the proton flux (ϕ), and number of W atoms (N) must be known:

$$N\sigma\phi \;=\; R \tag{1}$$

To determine the activity in the foil, one must first determine the activity at the end of the irradiation. During the irradiation, assuming beam fluctuations are infrequent and small, the rate of change in the number of ^{148}Gd atoms (n) is

$$dn = R\ dt - \lambda n\ dt \tag{2}$$

Solving this equation for $n(t)$ gives

$$n(t) = \frac{R}{\lambda}\left(1 - e^{-\lambda t}\right) + n_0 e^{-\lambda t} \tag{3}$$

where λ is the radionuclide decay constant. Since there is no ^{148}Gd initially, $n_0 = 0$ and the activity becomes

$$A_i = \lambda n(t = t_i) = A\left(t = t_i\right) = R\left(1 - e^{-\lambda t_i}\right) \tag{4}$$

where t_i is the irradiation time. For a counting time $t_1 > t_i$ to $t_2 > t_1$, the cumulative alpha emission is related to the alpha detection rate (C) by

$$\frac{C}{\epsilon} = \int_{t_1}^{t_2} A_i e^{-\lambda t} dt \tag{5}$$

where ϵ is the overall detection efficiency. Integrating over the counting time, t_1 to t_2, gives

$$\frac{C}{\epsilon} = \frac{A_i}{\lambda}\left(e^{-\lambda t_1} - e^{-\lambda t_2}\right) \tag{6}$$

Substituting A_i from equation (4) and rearranging the resulting equations yields

$$R = \frac{C\lambda}{\epsilon\left(1 - e^{-\lambda t_i}\right)\left(e^{-\lambda t_1} - e^{-\lambda t_2}\right)} = N\sigma\phi \tag{7}$$

In addition to relating the ^{148}Gd activity to the ^{148}Gd production cross section, this equation can be used to determine the proton flux by using the known reaction cross section of ^{27}Al(p,x)^{22}Na.

$$\phi_p = \frac{1}{N_{Al}\ \sigma_{Na}}\ \frac{C_{Na}\ \lambda_{Na}}{\epsilon_{Na}\ \left(1 - e^{-\lambda_{Na} t_i}\right)\ \left(e^{-\lambda_{Na} t_1} - e^{-\lambda_{Na} t_2}\right)} \tag{8}$$

This proton flux can in turn be used to determine a production cross section for W(p,x)^{148}Gd.

$$\sigma_{Gd148} = \frac{1}{N_W\ \phi_p}\ \frac{C_{Gd}\ \lambda_{Gd}}{\epsilon_{Gd}\ \left(1 - e^{-\lambda_{Gd} t_i}\right)\ \left(e^{-\lambda_{Gd} t_1} - e^{-\lambda_{Gd} t_2}\right)} \tag{9}$$

3.2 ^{22}Na Activation

In order to determine the proton flux given in equation (8) of the previous section, aluminum foils would be irradiated with the tungsten, tantalum, and gold foils. Protons interact with aluminum to produce the ^{27}Al(p,x)^{22}Na reaction, where (p,x) represents a combination of any number of reactions from incident protons to produce the radionuclide. The ^{22}Na radionuclide produced emits a 1274 keV photon that can be counted with a γ-ray detector.

Seven measurements of this reaction cross section exist for 800 MeV protons, and five measurements for 600 MeV protons (Figure 6) [36–46]. The conclusion from surveying the available experimental data is that Tobailem *et al.*'s measurement in 1981 at 600 MeV [38] and George Morgan *et al.*'s recent measurement at 800 MeV [40] are the most reliable. These cross section values, 16.0±1.1 mb and 14.3±0.4 mb, at 600 and 800 MeV, respectively, were used in this analysis. The average of the cross section data at 800 MeV is 14.3±0.4 mb, which is the value of George Morgan *et al.*'s measurement and the average cross section data at 600 MeV is 15.9±0.8 mb, close to Tobailem *et al.*'s measurement. However, the other 600 and 800 MeV cross section data are not reliable for reasons such as how the absolute proton flux measurement is done or variations of the cross section with respect to other energies.

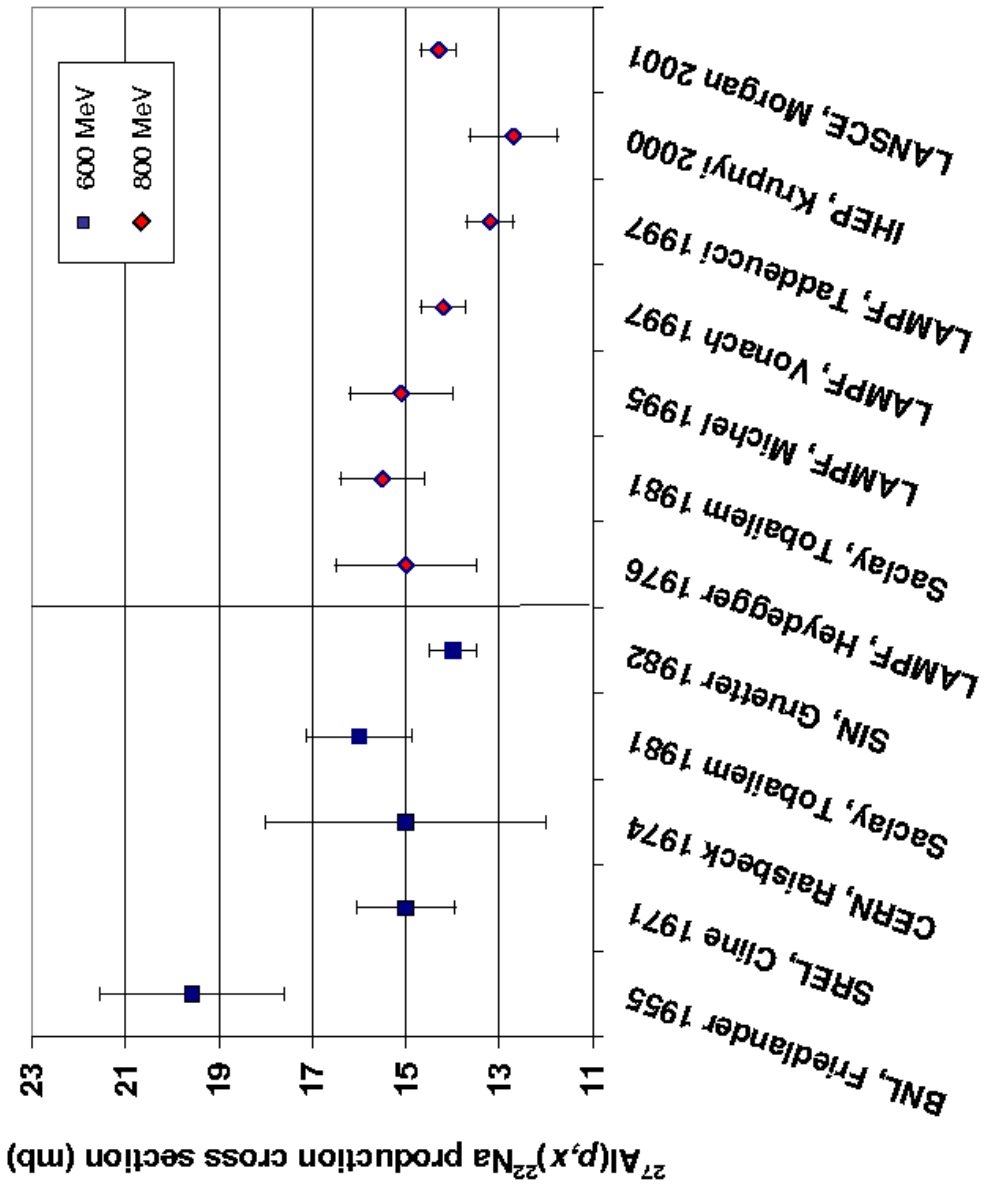

Figure 6: Previous measurements for ^{22}Na production cross sections at 600 and 800 MeV.

3.3 Foil setup

Thin foil irradiation was chosen as the preferred method for measuring the ^{148}Gd production cross section from tungsten, tantalum, and gold. A foil stack to be irradiated would consist of one aluminum foil, three tungsten, tantalum, or gold foils, followed by three aluminum foils. Stacks of three foils are used to investigate any possible loss of ^{148}Gd and ^{22}Na recoils in the material of interest. When determining the proton flux and production cross section, only the middle foil in a stack is counted, assuming recoil from the first foil balances the loss by recoil to the third foil.

Another method is to irradiate only one foil, sandwiched between two aluminum catcher foils. In this case, the sum of ^{148}Gd counted from the heavy metal foil and the two aluminum catcher foils would be used to determine the production cross section. This approach is viable because ^{148}Gd is not produced by spallation reactions in Al. The portion of ^{148}Gd recoiling forwards and backwards can be determined by this method.

All foils used in this work were made by Goodfellow Corporation and are 5 cm x 5 cm with a tolerance in size of 2% ($\pm$1 mm). Descriptions of the foils can be found in Table 5. Since the foils are thin, they can have pinholes in them and the theoretical density cannot be used in determining the number of atoms (N) in the foil. Each foil was weighed and the size was measured to obtain the average areal density in mg/cm^2 (Table 6). Assuming the foil has a uniform thickness over the area, N can be obtained from the weight of the foil.

Table 5: Summary of foil information provided by Goodfellow Corporation

Material	Thickness (μm)	Purity (%)	Impurities (wppm)	Pinholes present
Tungsten	3.00±0.75	99.95	Ca<20, Cu<20, Fe 20, Mg<10, Mo 150, Ni<20, Pb<50, Si<50, Sn<30, Ti<20, C 30, H 6, N 10, O 30	yes
Tantalum	3.00±0.75	99.9	Al 5, Ca 2, Co 1, Cr 5, Cu 2, Fe 30, Mg 5, Mn 2, Mo 100, Na 10, Nb<500, Ni 3, Si 10, Sn 2, Ti 20, V	yes
Gold	3.00±0.75	99.9	Ag 300, Al 1, B 1, Bi 2, Ca 4, Cd 4, Cr 5, Cu 500, Fe 2, K 15, Mg 1, Mn 1, Na 1, Ni 100, Pb 15, Pd 7	yes
Aluminum	10.00±1.50	99.0	Cu<1000, Fe<7000, Mn<1000, Si<5000, Zn<1000	no

Table 6: Measurements of the weight and size of each foil

foil	weight (mg)	area (cm^2)	areal density (mg/cm^2)	thickness (μm)
Al1	63.3	26.01	2.43	9.01
Al2	63.0	26.01	2.42	8.97
Al3	62.7	26.01	2.41	8.93
Al4	62.9	26.01	2.42	8.96
Al5	62.4	25.50	2.45	9.06
Al6	62.5	26.01	2.40	8.90
Al7	62.8	26.01	2.41	8.94
Al8	61.8	25.50	2.42	8.98
Al9	62.5	26.01	2.40	8.90
Al10	63.1	26.01	2.43	8.99
Al11	62.0	25.76	2.41	8.92
Al12	62.4	26.01	2.40	8.89
Al13	62.3	25.76	2.42	8.96
Al14	62.8	26.01	2.41	8.94
Al15	62.1	25.50	2.44	9.02
Al16	63.1	26.01	2.43	8.99
Al17	61.3	25.50	2.40	8.90
Al18	63.4	26.01	2.44	9.03
Al19	62.3	26.01	2.40	8.87
Al20	62.4	26.01	2.40	8.89
Al21	64.7	25.00	2.59	9.59
Al22	65.7	25.50	2.58	9.54
Al23	65.3	25.50	2.56	9.48
Al24	66.4	26.01	2.55	9.46
Al25	66.0	25.50	2.59	9.59
Al26	66.9	26.01	2.57	9.53
Al27	65.7	26.01	2.53	9.36
Al28	65.3	25.00	2.61	9.67
Al29	65.0	25.00	2.60	9.63
Al30	66.4	25.75	2.58	9.55
Al31	66.4	25.75	2.58	9.55
Al32	70.5	27.04	2.61	9.66
Al33	66.1	26.00	2.54	9.42
Al34	62.3	25.00	2.49	9.23
Al35	65.7	26.00	2.53	9.36
Al36	68.6	27.04	2.54	9.40
Ta1	113.2	25.00	4.53	2.73
Ta2	127.0	25.25	5.03	3.03
Ta3	123.5	25.25	4.89	2.95
Ta4	121.9	25.50	4.78	2.88
Ta5	121.4	25.50	4.76	2.87
Ta6	117.7	25.50	4.62	2.78

(Table 5 continued)

foil	weight (mg)	area (cm^2)	areal density (mg/cm^2)	thickness (μm)
Ta7	123.8	25.00	4.95	2.98
Ta8	120.0	25.00	4.80	2.89
W1	172.5	25.00	6.90	3.57
W2	176.2	25.50	6.91	3.58
W3	172.6	25.50	6.77	3.51
W4	194.8	26.01	7.49	3.88
W5	163.8	25.50	6.42	3.33
W6	167.1	25.50	6.55	3.39
W7	177.0	25.50	6.94	3.60
W8	144.5	25.00	5.78	2.99
Au1	164.6	26.01	6.33	3.28
Au2	154.2	25.50	6.05	3.13
Au3	160.7	25.00	6.43	3.33
Au4	154.5	25.25	6.12	3.17
Au5	141.4	25.50	5.55	2.87
Au6	138.1	25.25	5.47	2.83
Au7	150.1	25.25	5.94	3.08
Au8	149.1	25.25	5.90	3.06

Each foil was sandwiched between two aluminum frames for ease of handling, with an exposed area of 4 cm x 4.4 cm. Aluminum was chosen for the frame material because it is a low Z material and if activated, would not produce radionuclides above Z=15, resulting in no ^{148}Gd production. Foils would then be assembled together and irradiated with 600- or 800-MeV protons.

3.4 Detection

After irradiation, the foils are counted by α and γ spectroscopy. The charged-particle spectroscopy system is used to detect the 3.18-MeV α decay from ^{148}Gd. The γ spectroscopy system is used to detect the ^{22}Na (1274-keV line) to determine the proton flux, as well as detect other γ-emitting radioisotopes that have been produced in the tungsten, tantalum, and gold foils.

3.4.1 Charged-particle spectroscopy

The charged-particle spectroscopy system includes a silicon semiconductor diode detector. When a charged particle passes through a semiconductor, electron-hole pairs are produced along the track of the particle. With an applied field, the electrons created on the conduction band and holes created on the valence band move in opposite directions. The charges are collected at either boundary of the semiconductor with blocking electrodes. At the junction between the two bands, there is repulsion of majority carriers (electrons in n-type and holes in p-type) so that a depleted region exists, which is the sensitive detector volume. A reverse bias voltage can be applied in the depleted region to widen the band until the point of voltage breakdown. This extends the volume over which radiation-produced charge carriers can be collected. The semiconductor material in this case is a thin strip of silicon implanted in the detector. A summary of the detector properties can be found in Table 7 [48, 49] and a list of the electronics used can be found in Table 9. The detector and sample are placed in rough vacuum (∼1 torr) since 3.2-MeV α particles can only travel ∼2 cm in air (Figure 7).

Table 7: Properties of ORTEC charged-particle detectors

	ULTRA U-014-050-100	ULTRA-AS U-019-300-AS
Active area (mm^2)	50	300
Range of active thickness (μm)	100-500	100
Diode structure	Implanted boron– N-type Si implanted As partial depletion	Implanted boron– N-type Si implanted As partial depletion
Resolution (keV FWHM) for ^{241}Am at 5.486 MeV	14	19

The overall efficiency of the detector system was determined by using calibrated ^{148}Gd and ^{241}Am sources. Efficiency is a factor of geometry, distance, solid angle, intrinsic detector efficiency (virtually 100% for α particles in Si), electronics, and quality of vacuum. The

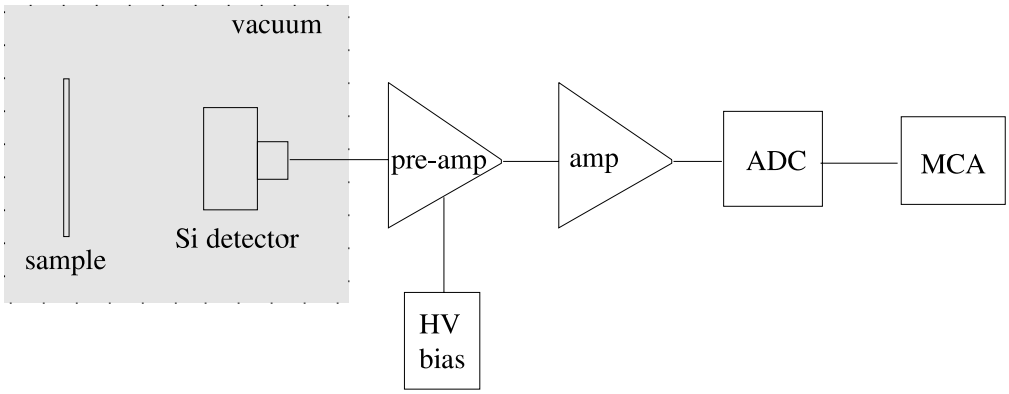

Figure 7: Schematic diagram of the charged-particle spectroscopy system

efficiency curve was essentially linear with respect to energy for the charged-particle system and depended heavily on the distance and solid angle from the sample to the detector.

Gadolinium decays by a single 3.18-MeV α emission. The range of a 3.18-MeV α particle in tungsten (19.3 g/cm^3) is 4.76 μm, according to SRIM [47]. In order to count all of the ^{148}Gd α particles in a foil, the thickness had to be less than this value. Figure 8 shows the stopping power of an alpha particle in tungsten, gold, tantalum, and aluminum. The thinnest foil that could be manufactured without using permanent mylar support backing was 3 μm for tungsten and therefore this thickness was chosen for all three materials. The energy loss of the ^{148}Gd α particle passing through 3 μm of tungsten is 1.7 MeV. In counting, one expects to see a broad peak ranging from $\sim$1.5 to 3.18 MeV for tungsten and gold, since they have the same density. In the counting of tantalum foils, however, a broad peak from $\sim$1.8 to 3.18 MeV should occur, because of its different density. The ^{148}Gd α peak should be almost level over the energy range, since the stopping power is relatively linear over this range (Figure 8). The aluminum foil thickness (10 μm) was chosen to be thicker and less fragile than the heavy metal foil, since α particles can travel much further in aluminum.

A wide energy range of beta particles from various radionuclides are also emitted from the foils and will deposit energy in the detector. Only low energy electrons will deposit all of their energy. Higher energy electrons will deposit only a portion of their energy.

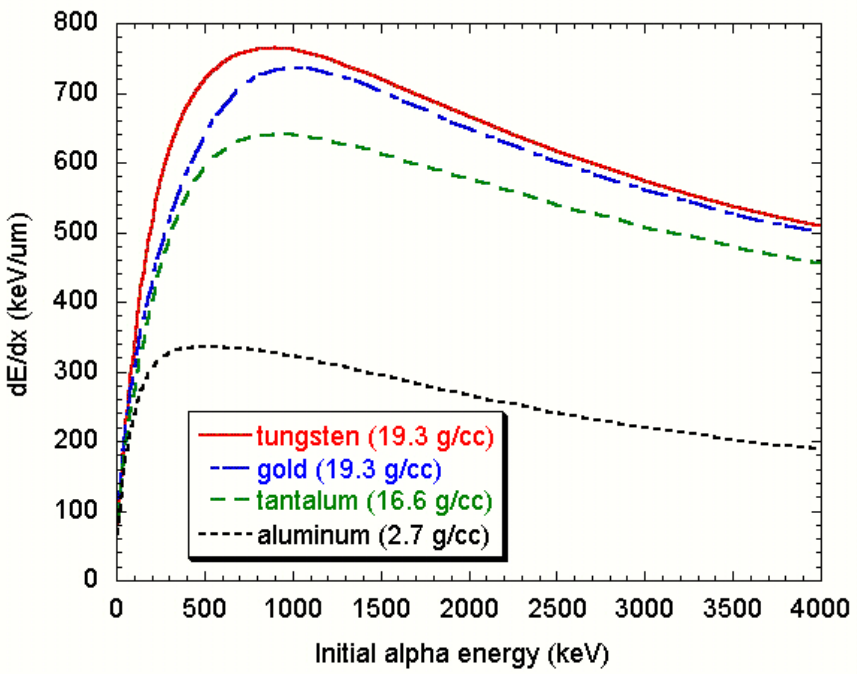

Figure 8: SRIM calculation of the energy loss of an alpha particle through tungsten, gold, tantalum, and aluminum

However, sharp peaks in the beta spectrum can be observed since some electron paths will lie completely in the depleted region of the detector. This complicates the alpha counting since the lower energy portion of the alpha peak is superimposed on a beta background. There are several ways to solve this problem. One method is to place a sufficiently thick aluminum foil in front of the irradiated foil to block all alphas from reaching the detector. The beta spectrum can then be subtracted from the combined alpha/beta spectrum to produce a clean alpha peak. A second method would be to sweep away the betas instead of the alphas by placing a magnet around the foil or detector, taking care not to block the view of alphas reaching the detector.

In addition to charged-particles, the foils will also emit γ-rays, which can be detected by the semiconductor detector. Like the electrons, only low energy photons will deposit all of their energy in the detector. To determine the γ portion of the spectrum, sufficiently thick aluminum is placed in front of the detector to block all alphas and betas from reaching the detector. The γ portion of the spectrum would then have to be corrected for attenuation through the aluminum.

3.4.2 Gamma spectroscopy

A high-purity Ge (HPGe) detector system inside a copper-lined, lead-brick housing is used to detect γ rays. The Ge detector is also a semiconductor and behaves in the same way as the silicon detector regarding charge collection. However, γ spectroscopy behaves in an extremely different manner than charged-particle spectroscopy. In the Si detector, α particles deposit all of their energy so that intrinsic efficiency is near 100%. In the HPGe detector, γ rays can have many different types of interactions and may not deposit all of their energy in the detector, making intrinsic efficiency range from 10 to 100%, depending on the detector. Photoelectric effect, Compton scattering, and pair production cause single escape, double escape, bremsstrahlung, and backscatter peaks along with the full energy peak. When the foils are activated, there are literally hundreds of full-energy peaks in the spectrum, so that care must be taken to consider all the different types of peaks when analyzing spectra. The specifications of the HPGe detector used are found in Table 8 [50]. The electronic setup of the Ge detector system is the same as the Si detector system in Figure 7 except that the counting is not done in vacuum and the preamp is built onto the end of the detector. A complete list of the electronics used can be found in Table 9. To reduce background, a lead crypt was built around the detector and foil counting area and lined with copper sheet to reduce the x-ray fluorescence radiation energy from lead x rays. This reduced the background by several orders of magnitude.

Table 8: Properties of ORTEC GAMMA-X HPGe coaxial detector for a ^{60}Co source

	GMX-20195-P
Relative photopeak efficiency (%)	20
Resolution at 5.9 keV (eV FWHM)	650
Resolution at 1.33 MeV (keV FWHM)	1.90
Peak to Compton ratio	40:1

The γ-spectroscopy system was used not only for measuring ^{22}Na, but also for measuring other radionuclide production cross sections. Hundreds of peaks below 1600 keV were found with an 8192 channel multichannel analyzer. Pulse-height spectrum analyses were performed by PCGAP, a software program by Killian and Hartwell at INEEL [52]. PCGAP provided detector efficiency curve fitting, energy calibration, and photopeak identification and fitting techniques. A library of radioisotopes (see Appendix B) was made for PCGAP to identify peaks. Once PCGAP found photopeaks in a spectrum, they were fitted to a Gaussian shape to determine areas, centroids, widths, and their uncertainties. The fitting procedure is an iterative method that minimizes the sum of the squares of the deviations of data from a Gaussian form. For those peaks that could not be fit with this nonlinear technique, a linear least squares algorithm was used. This algorithm assumes that the photopeak is Gaussian and has a linear background. The Gaussian height and coefficients of a linear spectral background line are determined from the fit. Energy calibration and photopeak width were determined automatically by the program using a ^{152}Eu calibration spectrum. PCGAP located five of the fourteen photopeak lines (121.8, 344.3, 778.9, 1112.1, and 1408.0 keV) in the spectrum, performed a least squares fit of the centroids and photopeak energies to get a second order polynomial energy scale. The widths and centroids were fit with a first order polynomial to determine the coefficients of the FWHM versus channel function. All of the ^{152}Eu energy lines and intensities are listed in Appendix Table B.1.

The overall efficiency of the HPGe detector system was measured using a calibrated ^{152}Eu source (Figure 9) with and without attenuator plates at a distance of 19.5 inches. A stack of aluminum attenuator plates were used so that foils could be counted shortly after irradiation when the count rate was high. In the case of Ge detector systems, the efficiency curve is not linear over the energy range of interest (10-1600 keV). Up to $\sim$40 keV, the interaction efficiency is dominated by the attenuation of photons by materials outside the detector and by any dead layers on the detector edge. Up to 200 keV, virtually all incident photons are detected. Above this energy, the interaction efficiency falls off with the total absorption cross section of Ge, which is dominated by the fall-off in the photoelectric cross section [51].

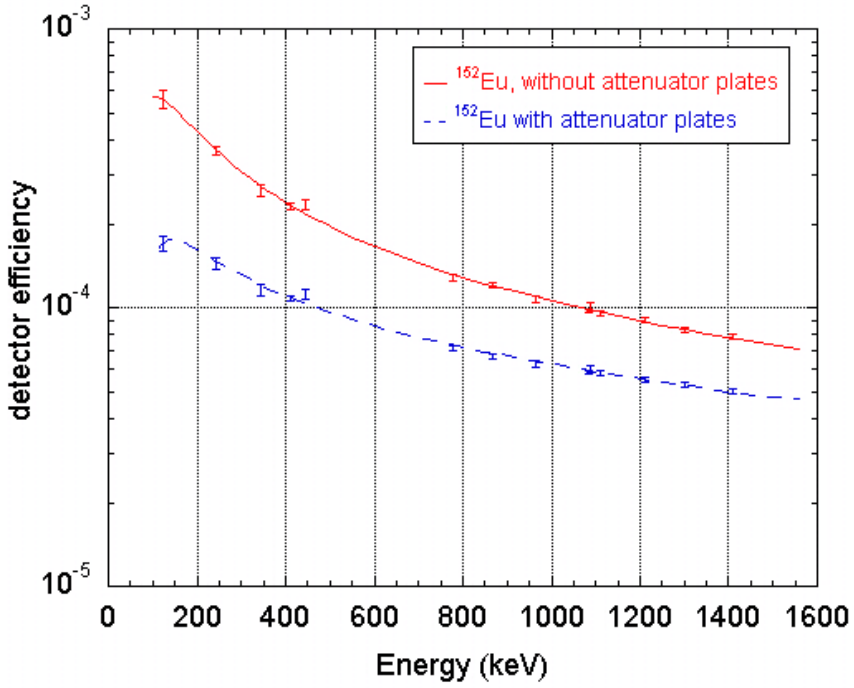

Figure 9: Overall efficiency for the HPGe detector, with and without attenuator plates

Table 9: Electronics for the detector systems

	γ-ray	α-1	α-2
High Voltage	ORTEC 459	ORTEC 556	Tennelec 953
Preamplifier	(with detector)	CSTA1 from Institut fur Kernphysik T. H. Darmstadt	ORTEC 142
Amplifier	ORTEC 672	ORTEC 571	ORTEC 571
ADC	Amptek MCA8000	ORTEC	ORTEC

CHAPTER IV

EXPERIMENTS

"Why think? Why not try the experiment?" John Hunter

A series of foil irradiations with 600- and 800-MeV protons were performed in the Blue Room at WNR (Figures 2 and 10). Anticipated beam spot sizes were 1 cm in diameter, so each foil had to be sufficiently large, 4 cm x 4.4 cm inside the frame, to subtend all of the proton beam. Framed foils were stacked together and mounted on a larger frame that centered the foils inside the vacuum chamber where they were to be irradiated. The vacuum chamber was located at the back of the Blue Room, upstream of the last steering magnet (Dorothy J) for Target 4.

To aid in positioning and shaping the beam spot, a phosphor was mounted on a frame and placed in the vacuum chamber. The vacuum chamber was made so that the foils and phosphor could be pushed in and out of the beam line, without having to break vacuum (Figure 11). At the beginning of each experiment, the foils were placed out of beam while operators tuned onto the phosphor at low current. The phosphor would glow where the proton beam was hitting it, giving a good indication of the size and shape of the beam spot. Once tuning was complete, the phosphor was pulled out of the beam line, and foils were pushed in to the beam line.

After the irradiations, radiograph image plates were exposed to the β- and γ-rays emitted from the foils to determine the exact location, size, and shape of the beam spot. The imaging plate is comprised of a BaFBr:Eu^{2+} ionic crystals where the Ba is replaced with Eu^{2+} to create a solid solution. During exposure to the irradiated foil, part of the Eu^{2+} ions become Eu^{3+} through x-ray ionization. These electrons are trapped into the Br ion empty lattices of the lattice defects, and color centers of the metastable state are formed. When the image plates are read by laser, the light absorbed by the color center is irradiated

and the trapped electrons are liberated again into the conduction band. The light is then collected and guided towards a photomultiplier tube to produce the image. Because of parallax, a geometric distortion effect, the images detected on the image plate were slightly larger than the actual profile. To determine the true profile of the beam, a gaussian profile was assumed and the parallax was modeled in MCNPX with a gaussian source.

Figure 10: Blue room setup for foil irradiation at WNR. Protons enter from the left.

The irradiations took place in two modes, sole use and parasitic. Behind the Dorothy J steering magnet is Target 4 at WNR, where neutrons are produced and scattered to different beamlines for experiments. When in sole use, Target 4 was used as a beam stop, not for production of neutrons. In parasitic mode, the proton beam passed through the foils and then on to Target 4 for neutron production. The energy loss through the foils was negligible ($\leq$0.11 MeV) so all the foils saw essentially the same energy, with no proton energy

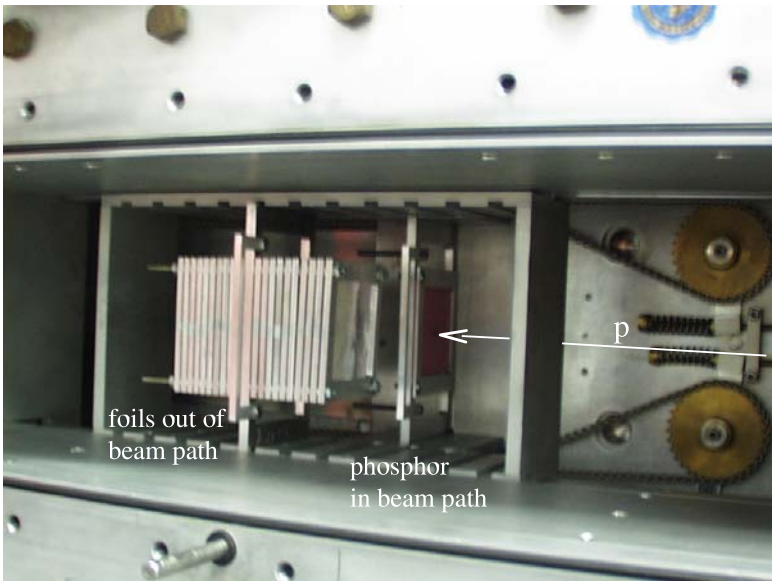

Figure 11: Close up of vacuum box in WNR's Blue Room. The foil pack is out of beam and the phosphor is in the beamline. Protons enter from the right.

loss to Target 4. It was determined that as much as 30 mg/cm^2 could be placed in the beam without significantly degrading the neutron production from Target 4 downstream. Because of the long distance to Target 4 and low probability of backscatter upstream, there was essentially zero probability of neutrons from Target 4 interacting with the foils.

The first irradiation employed sole use of the LANSCE facility and took place July 5-7, 2002. The experiment required reducing the proton energy from a normal operating mode of 800 MeV down to 600 MeV. The foil arrangement front to back was one aluminum, three tungsten, one aluminum, three tantalum, one aluminum, three gold, and three aluminum foils. The aluminum foils between the tungsten, tantalum, and gold foils were to prevent cross-contamination between the three metals. The three aluminum foils at the back were used to determine the proton flux. The proton energy degradation through this foil stack (73 mg/cm^2) was negligible (0.11 MeV) so all the foils saw essentially the same proton energy. The irradiation lasted for two days at 3 μA and activated the foils to >5 rem/hr on contact (Figures 12a, 13a, 14a).

The second irradiation (August 8-9, 2002) ran in parasitic mode, where production of neutrons from Target 4 played an important role. This experiment was scheduled during

Target 4 neutron production, which was of higher priority. A phosphor aided in tuning the beam to just right of center and small in size, but still tuned to Target 4. This 800-MeV experiment irradiated in front-to-back order one aluminum, three tantalum, and three aluminum foils (24 mg/cm^2) for 17 hours at an average current of 2.4 μA. Problems with vacuum and beam spill from our targets caused significant drops in current (from 4.0 μA to 1.5 μA) which reduced the number of neutrons produced from Target 4 and ultimately, the end of the irradiation (Figure 12b). The foils read 600 mrem/hr on contact three days after the irradiation. Radiographing the foils indicated that a small portion ($\sim$5%) of the beam had irradiated the edge of the aluminum frames, which caused the beam spill problems (Figures 13b, 14b).

The third and fourth set of irradiations took place October 12-15, 2002 in parasitic mode at 800 MeV. Tuning the beam to the foil stack and Target 4 required moving the beam from the lower right hand corner of the frame towards the lower center of the foil. The first set of foils irradiated were three gold foils and four aluminum foils (28 mg/cm^2) for 32 hours. Then, three tungsten and four aluminum foils (30 mg/cm^2) were irradiated for 20 hours. Both irradiations received an average current $>$4 μA, without any observed problems with vacuum, beam spill, or significant interference to neutron production on Target 4 (Figure 12c). Both foil stacks read $>$5 rem/hr on contact two hours after beam shutdown. Radiograph images of the foils showed later that during the tungsten irradiation, the beam was moved towards the lower right hand corner, where a small percentage of the beam hit the frame (Figures 13c, 13d, 14c, 14d).

All of the previous irradiations employed the three-foil method. The final irradiation took place January 13-15, 2003 with single foils in Blue Room sole use time, with no production at Target 4. The foil stack was arranged front to back as follows: one aluminum, one tungsten, two aluminum, one tungsten, two aluminum, one tantalum, two aluminum, one tantalum, two aluminum, one gold, two aluminum, one gold, and three aluminum foils. Two aluminum foils were placed in between each single foil to prevent cross-contamination on the aluminum catcher foils. The beam spot was tuned right of center and oblong in shape (Figures 13e, 14e) and the current was steady at 3 μA (Figure 12d). Six days after

the irradiation, the foil packs read 2 rem/hr on contact.

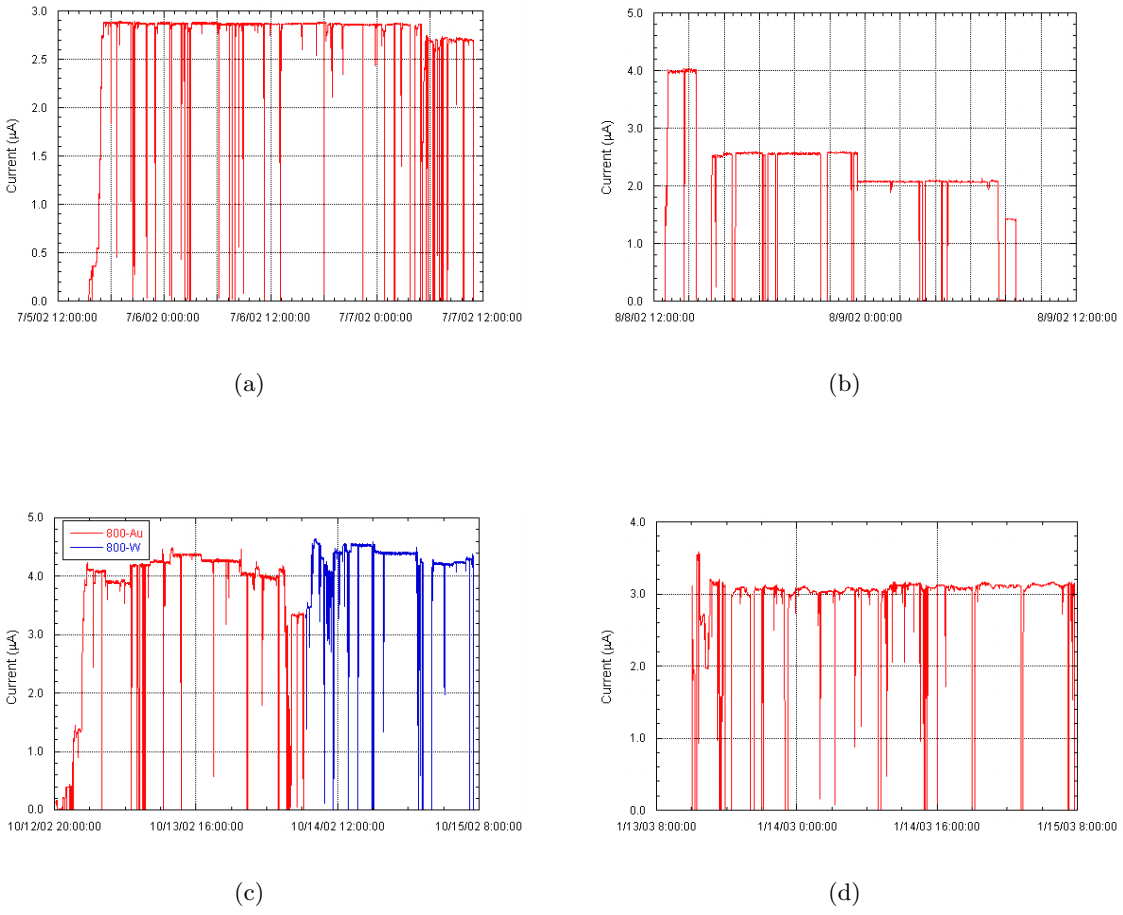

Figure 12: Current monitor readings for the (a) 600-MeV irradiation of stacked W, Ta, Au, (b) 800-MeV irradiation of stacked Ta, (c) 800-MeV irradiation of stacked Au and W, and (d) 800-MeV irradiation of single W, Ta, and Au foils.

During the irradiations, monitors upstream of the Blue Room took current readings every second. These current monitor readings (3% uncertainty) were compared with the measured ^{22}Na activation from the aluminum foils (7.7% uncertainty at 600 MeV and 4.1% uncertainty at 800 MeV) in Table 10. The proton flux measured from ^{22}Na activation was within eight percent of the current monitor, generally on the higher side. The current monitors were upstream of the Blue Room and a small percent of the proton beam could be lost between the monitors and the foils. All of the aluminum foils on irradiated frames were mounted onto unirradiated frames before ^{22}Na counting was done to exclude ^{22}Na produced

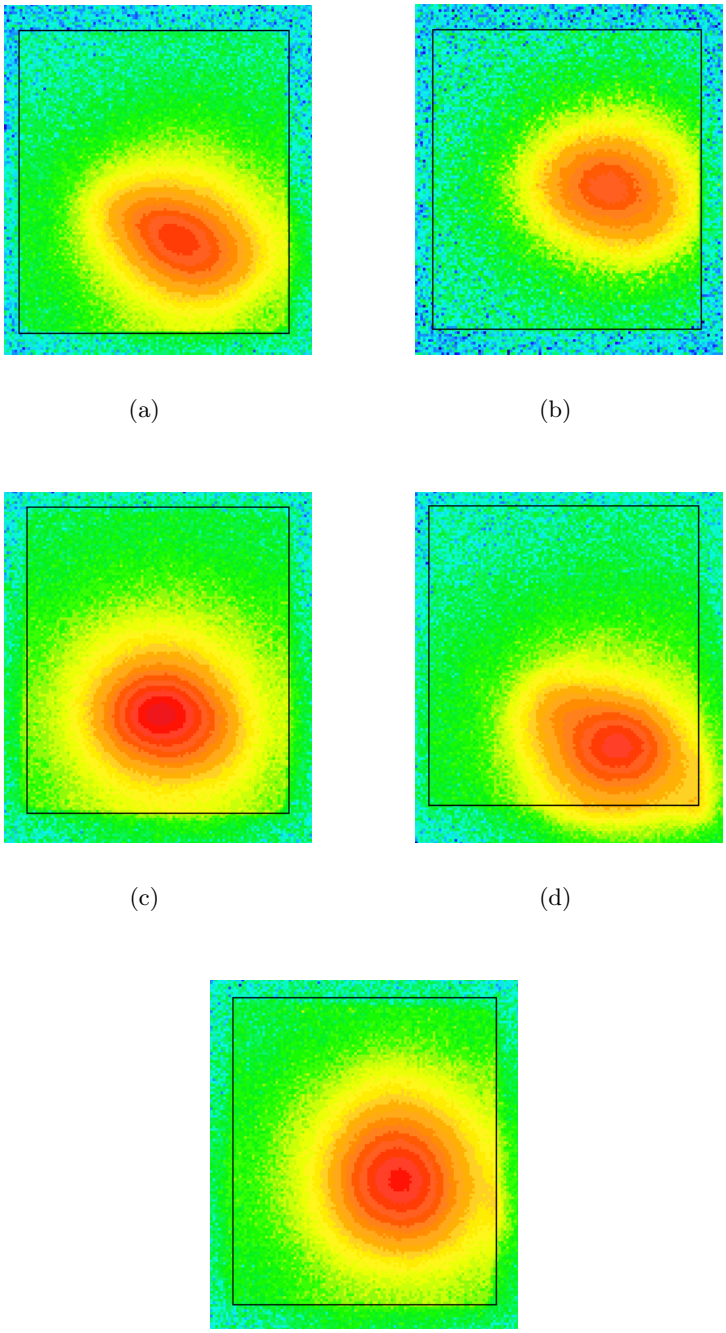

(a) (b)

(c) (d)

(e)

Figure 13: Radiograph images in linear color map of the (a) 600-MeV irradiation of stacked W, Ta, Au, (b) 800-MeV irradiation of stacked Ta, (c) 800-MeV irradiation of stacked Au, (d) 800-MeV irradiation of stacked W, and (e) 800-MeV irradiation of single W, Ta, and Au foils. Orientation shows top as beam up and right as beam right. The inside of the frame is indicated by a rectangle.

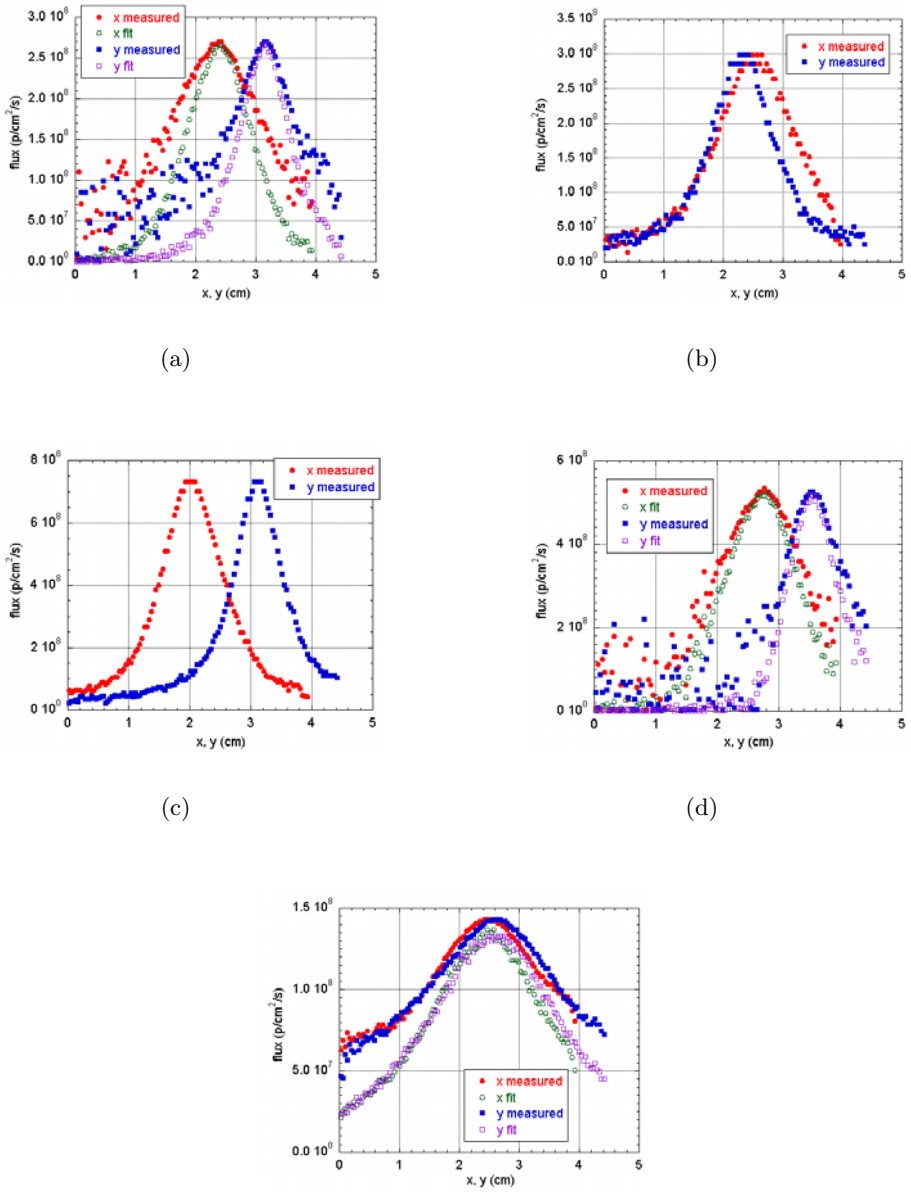

Figure 14: Relative beam profiles from radiograph images and fits of the (a) 600-MeV irradiation of stacked W, Ta, Au, (b) 800-MeV irradiation of stacked Ta, (c) 800-MeV irradiation of stacked Au, (d) 800-MeV irradiation of stacked W, and (e) 800-MeV irradiation of single W, Ta, and Au foils. The x and y profiles show the interior of the frame from 0-4 cm and 0-4.4 cm, respectively.

off the frames.

Table 10: Irradiations performed in the Blue Room at WNR during the 2002-2003 run cycle. Each irradiation measured the proton flux with Al foils for ^{22}Na activation and current monitors upstream of Blue Room

Metal Foils	Singles or Stacked Foils	Mode of operation	E_p (MeV)	Integrated ϕ_p (p/s) ^{22}Na Activation	Integrated ϕ_p (p/s) Current Monitor	Ratio of ^{22}Na to Monitor
W, Ta, Au	stacks of 3	sole use	600	1.76×10^{13}	1.63×10^{13}	1.08±0.09
Ta	stacks of 3	parasitic	800	1.42×10^{13}	1.32×10^{13}	1.08±0.05
Au	stacks of 3	parasitic	800	2.38×10^{13}	2.32×10^{13}	1.03±0.05
W	stacks of 3	parasitic	800	2.41×10^{13}	2.48×10^{13}	0.972±0.049
W, Ta, Au	singles	sole use	800	1.83×10^{13}	1.72×10^{13}	1.06±0.05

CHAPTER V

CROSS SECTION MEASUREMENT RESULTS

"Results! Why man, I have gotten a lot of results. I know several thousand things that won't work." -Thomas A. Edison

5.1 Uncertainty in the measurements

From equations (8) and (9) in chapter 3, the uncertainty (u) in the proton flux and cross section can be given as

$$u_{\phi_p}{}^2 = \left(\frac{A_{\phi_p}}{\epsilon_{Na}\ N_{Al}\ \sigma_{Na}}\right)^2 \left[u_{C_{Na}}{}^2 + C_{Na}{}^2 \left(\frac{u_{\epsilon_{Na}}{}^2}{\epsilon_{Na}{}^2} + \frac{u_{N_{Al}}{}^2}{N_{Al}{}^2} + \frac{u_{\sigma_{Na}}{}^2}{\sigma_{Na}{}^2}\right)\right] \tag{10}$$

$$u_{\sigma_{Gd}}{}^2 = \left(\frac{A_{\sigma_{Gd}}}{\epsilon_{Gd}\ N_W\ \phi_p}\right)^2 \left[u_{C_{Gd}}{}^2 + C_{Gd}{}^2 \left(\frac{u_{\epsilon_{Gd}}{}^2}{\epsilon_{Gd}{}^2} + \frac{u_{N_W}{}^2}{N_W{}^2} + \frac{u_{\phi_p}{}^2}{\phi_p{}^2}\right)\right] \tag{11}$$

where

$$A_{\phi_p} = \frac{\lambda_{Na}}{(1 - e^{-\lambda_{Na} t_i})\,(e^{-\lambda_{Na} t_1} - e^{-\lambda_{Na} t_2})}$$

$$A_{\sigma_{Gd}} = \frac{\lambda_{Gd}}{(1 - e^{-\lambda_{Gd} t_i})\,(e^{-\lambda_{Gd} t_1} - e^{-\lambda_{Gd} t_2})}.$$

Goodfellow Corporation reported a nominal uncertainty of 25% in the thickness of the foils. Prior to the experiments each foil was weighed and the size was measured to determine the areal density in mg/cm^2. This lowered the uncertainty from ∼25% to a few percent, assuming the thickness is uniform over foil. When the ^{148}Gd production cross sections for tungsten were first measured, there was a large variation between the experiments. This raised some doubt that the tungsten foil thicknesses were uniform across the area of the foil, resulting in 25% uncertainty again. Table 11 demonstrates how this uncertainty dominated the uncertainty in the cross section.

To reduce the uncertainty in the areal density of the foils, x-ray fluorescence (XRF) was used to map out the relative thickness pixel-by-pixel over the area of the irradiated foils. The micro-XRF instrument used a polychromatic Mo x-ray source to produce a shower of

Table 11: Sources of error in ^{148}Gd production cross section at 600 and 800 MeV prior to improving the areal density uncertainty

	Uncertainty (%)			
	600 MeV		800 MeV	
	Individual	Total	Individual	Total
Proton flux		7.7		4.1
-Ge detector efficiency	(1.9)		(1.9)	
-Areal density of Al	(2.8)		(2.8)	
-^{22}Na cross section	(6.9)		(2.4)	
-^{22}Na counting statistics	(0.3)		(0.3)	
Si detector efficiency		2.0		2.0
Areal density of W, Ta, Au		25.0		25.0
^{148}Gd counting statistics		0.5		0.5
^{148}Gd production cross section		26.2		25.4

bremsstrahlung in a ∼300 μm spot size [54]. The foil was placed in between the source and detector, which detected the L_α x-ray for the material. The Lα energies were 8.4 keV for W, 8.1 keV for Ta, and 9.7 keV for Au. The more counts the detector collected, the thicker the foil. One second counts were taken for each pixel over a 128x128 pixel array. The color map given by the instrument software was then converted to a numerical array that was scaled to the maximum number (Figure 15). This XRF analysis was performed for three tungsten foils (the middle foils from the 600- and 800-MeV stacked foil irradiations and one from the single foil irradiation) and one tantalum and gold foil, both from the single foil irradiation. It was clear that there was some loss of tungsten within the beam spot, but not so much for the tantalum and gold. During the irradiations, some of the tungsten must have sputtered off. The effect is less for the stacked foil irradiations, meaning that what was lost from this foil was offset by the surrounding foils sputtering onto it.

As can be seen from Figure 15, the analysis had noisy data. To smooth this out, each point in the 105x118 array inside the frame was averaged over a 5x5 array. This reduced the uncertainty in the XRF analysis to ∼1.5% for each foil. The array was then normalized by the average areal density in mg/cm^2, measured by weight and size prior to the irradiations and weighted by the flux profile array obtained from the image plates by

$$< \overline{\rho_A} >= \frac{\int_y \int_x \phi(x,y)\rho_A(x,y)\ \mathrm{d}x\ \mathrm{d}y}{\int_y \int_x \phi(x,y)\ \mathrm{d}x\ \mathrm{d}y}\ . \tag{12}$$

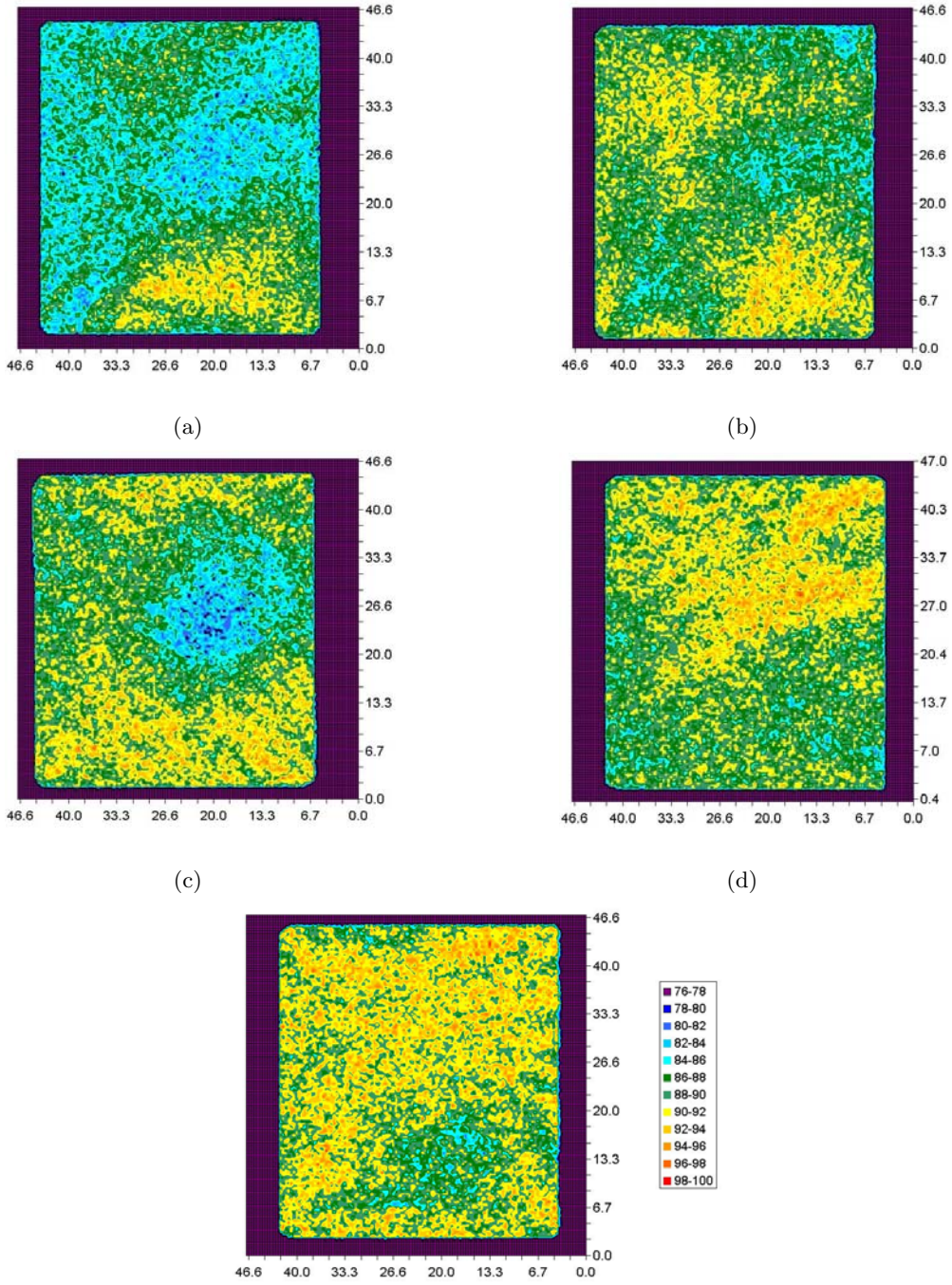

Figure 15: Relative thickness maps of (a) 800-MeV single foil irradiation of Au7 (b) 800-MeV single foil irradiation of Ta7 (c) 800-MeV single foil irradiation of W4 (d) 800-MeV stacked foil irradiation of W7 and (e) 600-MeV stacked foil irradiation of W1.

By weighting the thickness maps by the flux profile, the areal density decreased by two percent, at most (Table 12). This change in areal density increased the cross section measurements by only two percent but decreased the uncertainty in the cross section from 26% to 11% at 600 MeV and from 25% to 6% at 800 MeV, with the uncertainty now being dominated by the uncertainty in the proton flux (Table 13).

Table 12: Change in the areal density and its uncertainty by XRF analysis

		areal density (mg/cm^2)		
foil	irradiation	prior to XRF	after XRF	% change
W1	600 stacked	6.900±1.725	6.891±0.529	-0.14%
W7	800 stacked	6.941±1.735	6.806±0.283	-1.99%
W4	800 single	7.489±1.872	7.327±0.303	-2.21%
Ta7	800 single	4.952±1.238	4.908±0.203	-0.89%
Au7	800 single	5.945±1.486	5.889±0.244	-0.95%

Table 13: Sources of error in ^{148}Gd production cross section at 600 and 800 MeV after improving the areal density uncertainty with XRF

	Uncertainty (%)			
	600 MeV		800 MeV	
	Individual	Total	Individual	Total
Proton flux		7.7		4.1
-Ge detector efficiency	(1.9)		(1.9)	
-Areal density of Al	(2.8)		(2.8)	
-^{22}Na cross section	(6.9)		(2.4)	
-^{22}Na counting statistics	(0.3)		(0.3)	
Si detector efficiency		2.0		2.0
Areal density of W, Ta, Au		7.7		4.1
^{148}Gd counting statistics		0.5		0.5
^{148}Gd production cross section		11.1		6.2

5.2 ^{148}Gd production cross section

Two alpha counting chambers were used to count the charged particle spectra. Each of the tantalum and tungsten foils were counted over a two-to five-day period, and the gold foils were counted for a week to two weeks due to the low count rate. One of the gold

foils from the 800-MeV single foil irradiation, Au5, was not analyzed because it had a large puncture hole in it made before the irradiation. Placing it in the alpha chamber under vacuum might have damaged the foil further and contaminated the chamber.

For the stacked foils, only the middle foils were analyzed; whereas, the single foils plus the aluminum catcher foils had to be analyzed. The low-energy end of the ^{148}Gd plateau is easy to distinguish from the $\beta + \gamma$ spectrum for the tantalum foils, because of its density. However, the end of the ^{148}Gd plateau for the tungsten and gold foils was not separate in energy with the $\beta + \gamma$ curve. To determine the end of the ^{148}Gd plateau, the $\beta + \gamma$ curve was subtracted from the $\alpha + \beta + \gamma$ curve. All Al catcher foil spectra and $\beta + \gamma$ spectra were normalized to the counting times of the $\alpha + \beta + \gamma$ spectra.

The alpha chamber setup was modeled in MCNPX with a 3.18-MeV α source evenly distributed over the beam profile and thickness of each foil. An F8 pulse height tally detected the number of times α's deposited energy in a silicon detector with a brass collimator in a given number of energy bins. In other words, the F8 tally calculates the efficiency of the detector system. These curves are then normalized to a point in the measurement plateau and scaled with the actual measurement. All of the charged particle spectra and MCNPX fits can be seen in Figures 16-26. The MCNPX calculations show the low-energy end of the ^{148}Gd α plateau as higher in energy by several hundred keV than the measurement. This difference can be due to non-uniformity in the foil and that the foils are not perfectly flat. Some α's may have penetrated through more thickness than the actual foil thickness, leaving the α particles with less energy than expected. The low energy end of the plateau predicted by MCNPX agrees well within 100 keV of that predicted by SRIM.

From the 800-MeV single foil irradiation, the distribution of the recoils were determined (Table 14). Recoils on the aluminum catcher foils comprised only 10% of the total counts, with the forward recoils contributing 90-95% to the total recoils, as expected.

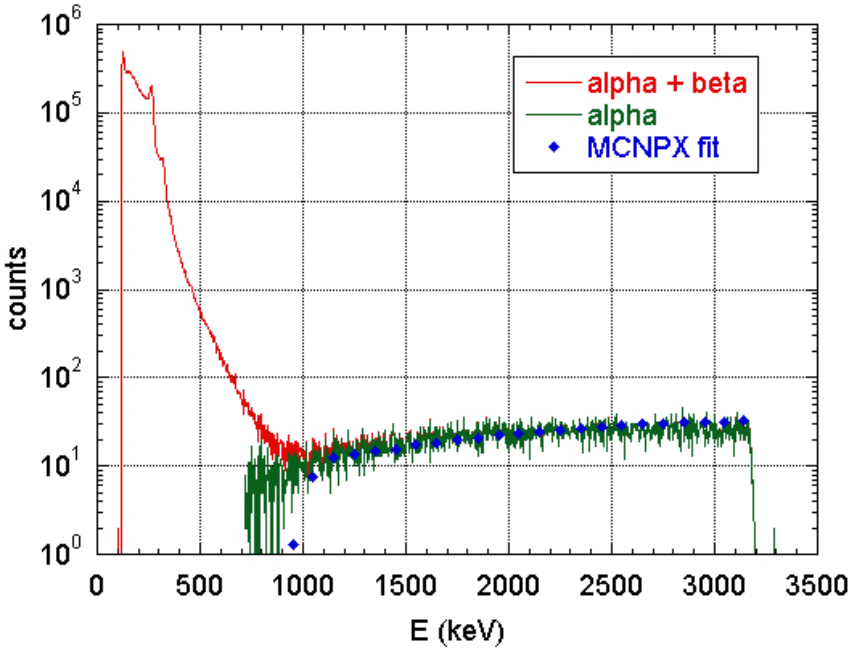

Figure 16: Charged particle spectrum of W1 from the 600-MeV stacked foil irradiation. Counting time was 2 days.

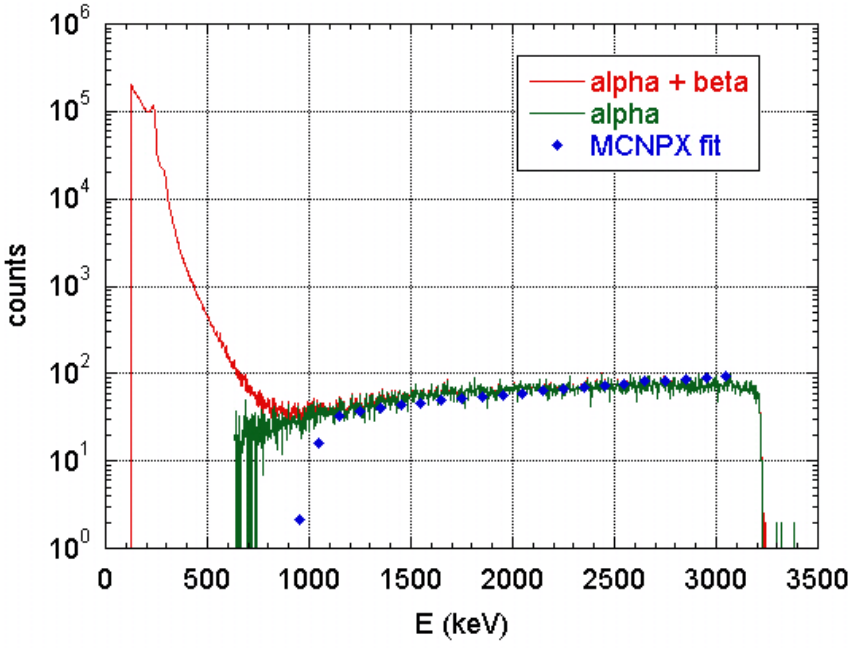

Figure 17: Charged particle spectrum of W7 from the 800-MeV stacked foil irradiation. Counting time was 3 days.

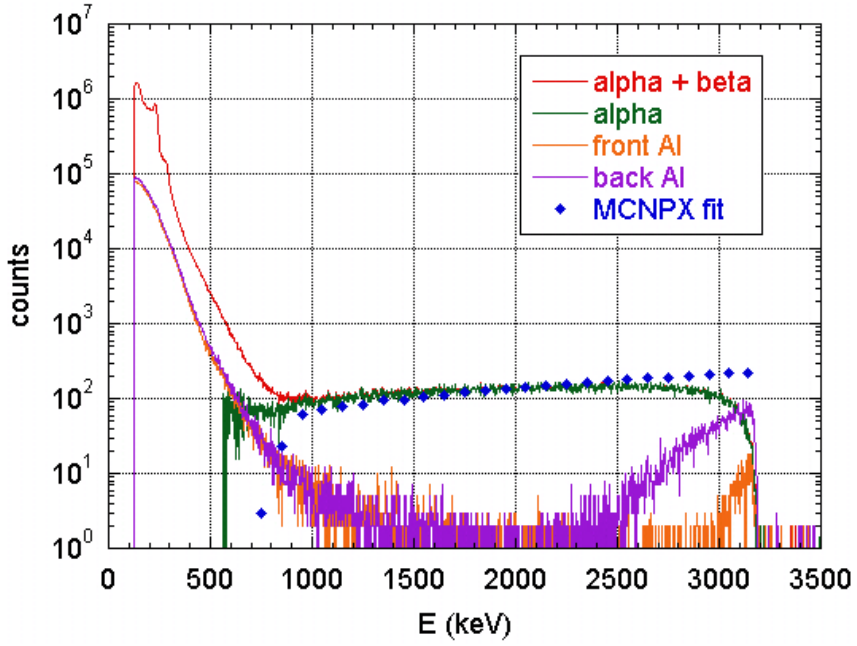

Figure 18: Charged particle spectrum of W4 and the surrounding Al foils from the 800-MeV single foil irradiation. Counting time was 5 days.

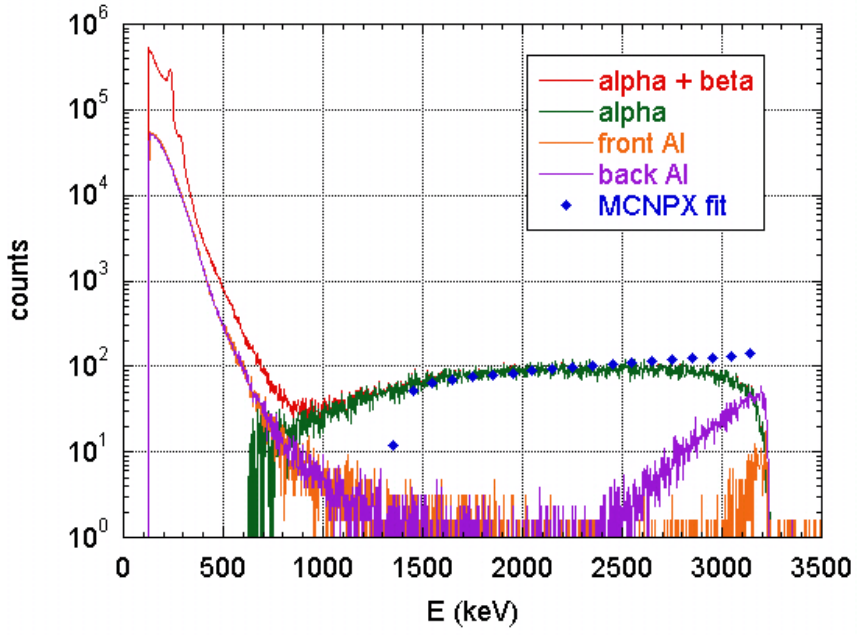

Figure 19: Charged particle spectrum of W8 and the surrounding Al foils from the 800-MeV single foil irradiation. Counting time was 3 days.

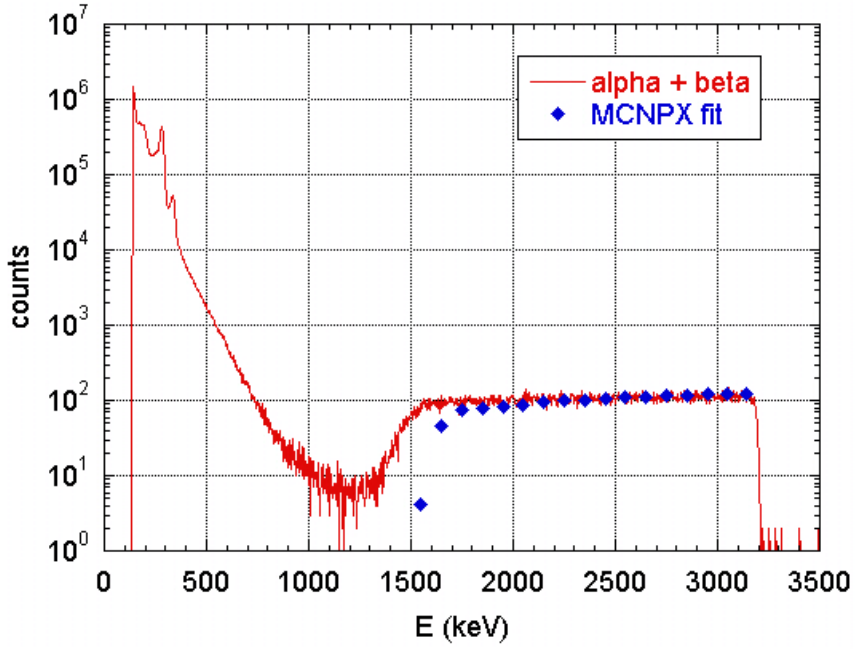

Figure 20: Charged particle spectrum of Ta2 from the 600-MeV stacked foil irradiation. Counting time was 5 days.

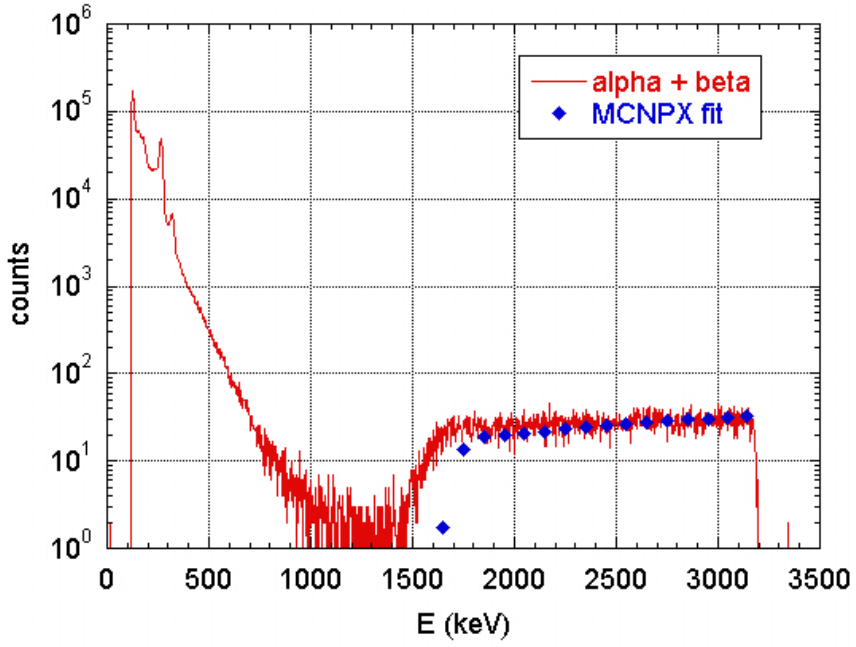

Figure 21: Charged particle spectrum of Ta5 from the 800-MeV stacked foil irradiation. Counting time was 2 days.

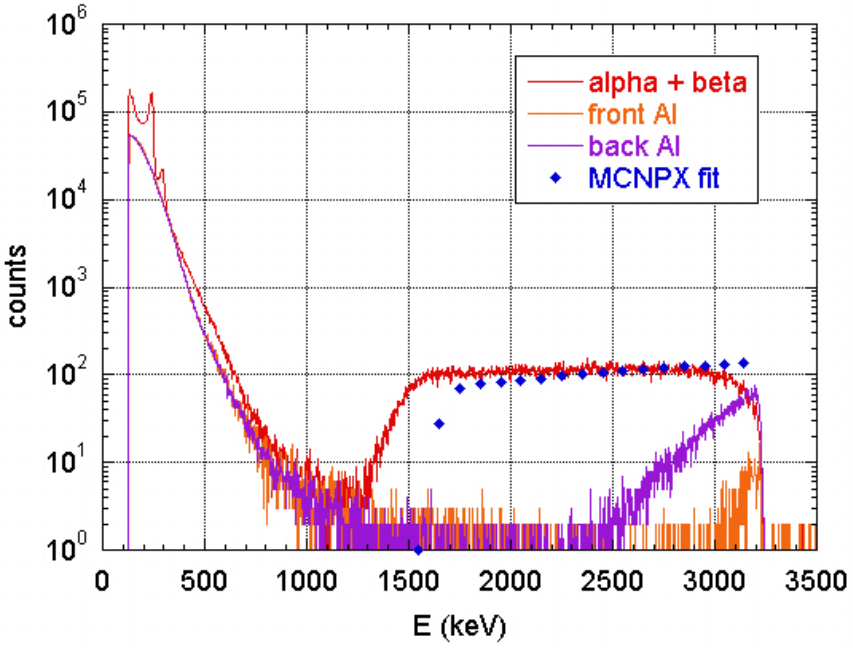

Figure 22: Charged particle spectrum of Ta7 and the surrounding Al foils from the 800-MeV single foil irradiation. Counting time was 3 days.

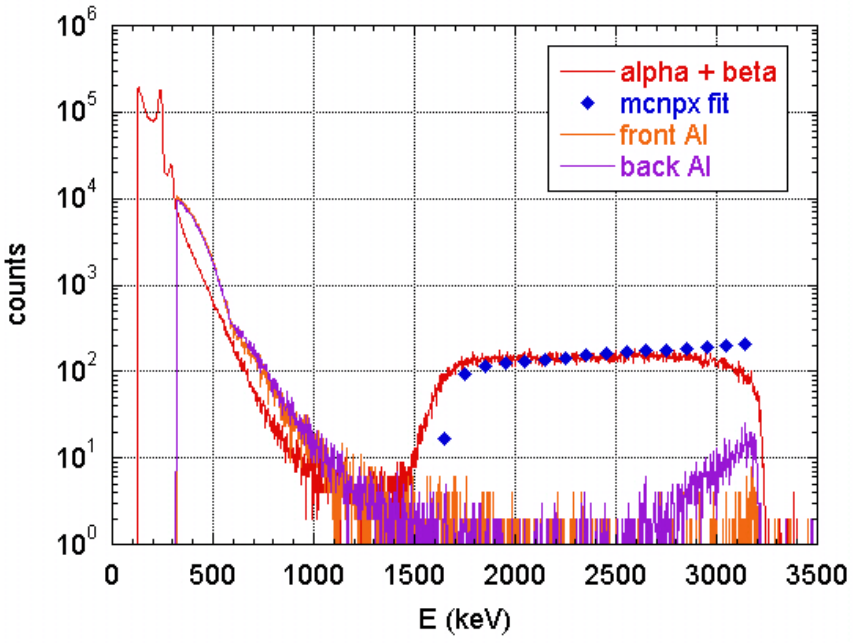

Figure 23: Charged particle spectrum of Ta8 and the surrounding Al foils from the 800-MeV single foil irradiation. Counting time was 4 days.

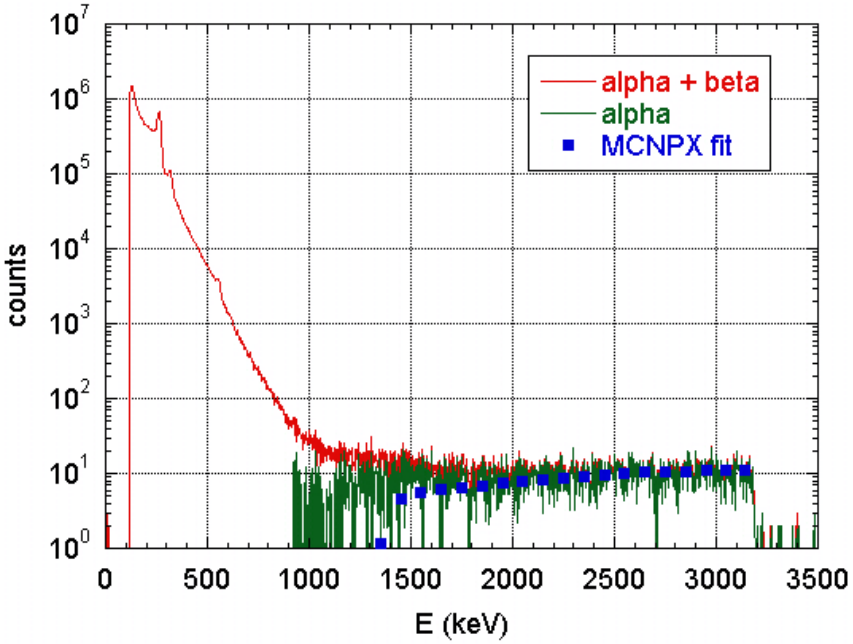

Figure 24: Charged particle spectrum of Au2 from the 600-MeV stacked foil irradiation. Counting time was 13 days.

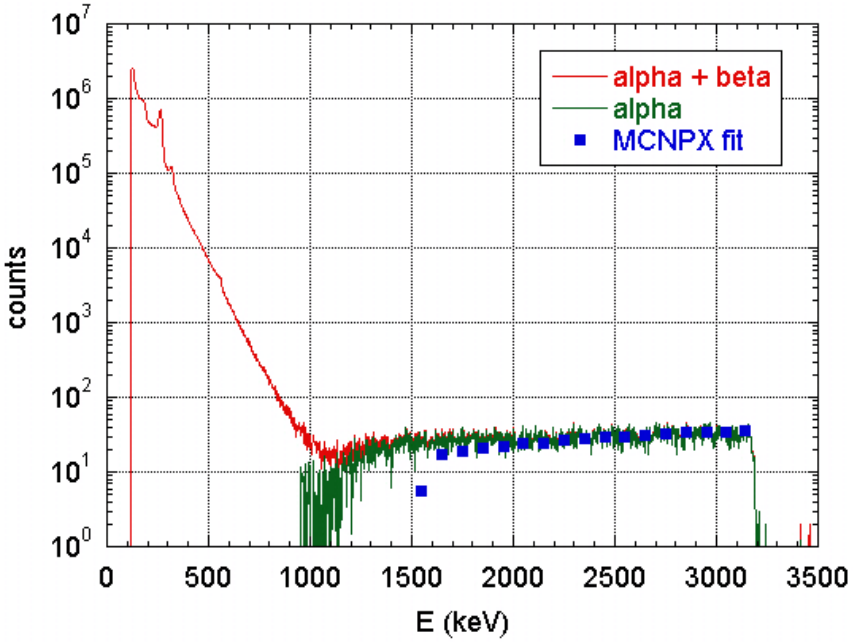

Figure 25: Charged particle spectrum of Au6 from the 800-MeV stacked foil irradiation. Counting time was 6 days.

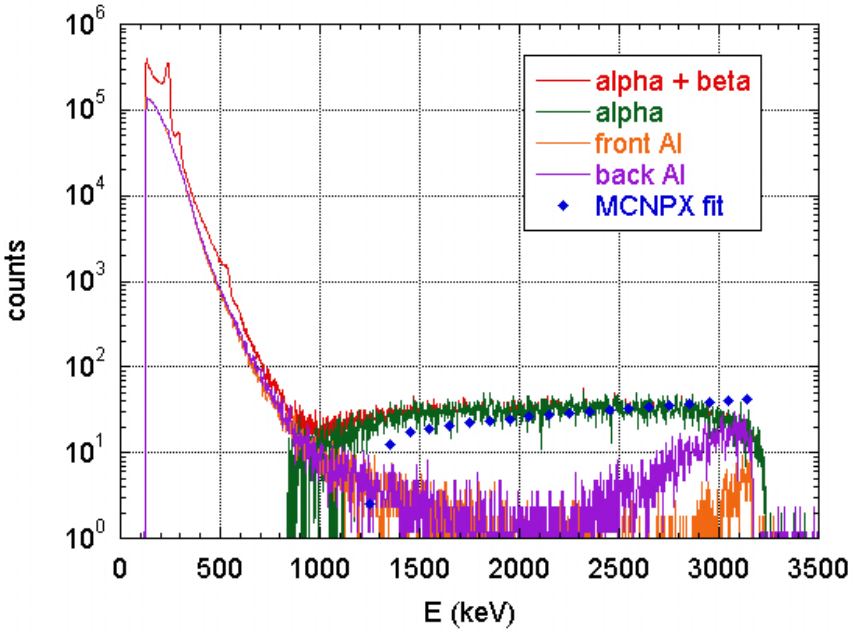

Figure 26: Charged particle spectrum of Au7 and the surrounding Al foils from the 800-MeV single foil irradiation. Counting time was 7 days.

Table 14: The ^{148}Gd α count rate for each middle and catcher foils. Uncertainty in the count rates were less than 1%.

			count rate (cps)			
			middle foil	front Al	back Al	total
Ta2	600 MeV	stacked	0.159			0.159
Ta5		stacked	0.097			0.097
Ta7	800 MeV	single	0.283	0.001	0.025	0.309
Ta8		single	0.256	0.005	0.053	0.313
W1	600 MeV	stacked	0.118			0.118
W7		stacked	0.212			0.212
W4	800 MeV	single	0.276	0.001	0.019	0.297
W8		single	0.248	0.001	0.019	0.268
Au2	600 MeV	stacked	0.007			0.007
Au5	800 MeV	stacked	0.043			0.043
Au7		single	0.040	0.001	0.005	0.046

To determine the ^{148}Gd production cross section, the constant variables in each calculation were the detector efficiency (8.12×10^{-4}) and the half-life of ^{148}Gd (74.6 y). All other variables depended on the irradiation time and current, the mass of the foil, and the counts under the alpha plateau. Tables 15-17 list these variables for each foil analyzed.

Table 15: The ^{148}Gd production cross section for tantalum

	Ta2 600 MeV stacked	Ta5 800 MeV stacked	Ta7 800 MeV single	Ta8 800 MeV single
flux (p/cm^{2}s)	9.98×10^{11}	7.94×10^{11}	1.04×10^{12}	1.04×10^{12}
N (at)	2.95×10^{20}	2.80×10^{20}	2.88×10^{20}	2.82×10^{20}
t_i (s)	149577	62005	156929	156929
t_1 (s)	7674297	8113405	10554089	10899329
t_2 (s)	8113343	8287618	10813528	11236541
counts	70094	16918	80125	105448
^{148}Gd prod σ (mb)	15.2±4.0	29.7±7.6	27.6±1.7	28.6±7.3

Table 16: The ^{148}Gd production cross section for tungsten

	W1 600 MeV stacked	W7 800 MeV stacked	W4 800 MeV single	W8 800 MeV single
flux (p/cm^{2}s)	9.98×10^{11}	1.37×10^{12}	1.04×10^{12}	1.04×10^{12}
N (at)	3.99×10^{20}	3.93×10^{20}	4.23×10^{20}	3.34×10^{20}
t_i (s)	149577	85256	156929	156929
t_1 (s)	11219577	16680600	5715329	9080129
t_2 (s)	11387097	16955970	6132414	9350379
counts	19792	58371	123673	72523
^{148}Gd prod σ (mb)	8.31±0.92	19.5±1.2	18.0±1.1	20.7±5.3

Table 17: The ^{148}Gd production cross section for gold

	Au2 600 MeV stacked	Au6 800 MeV stacked	Au7 800 MeV single
flux (p/s)	9.98×10^{11}	1.35×10^{12}	1.04×10^{12}
N (at)	3.26×10^{20}	2.95×10^{20}	3.18×10^{20}
t_i (s)	149577	117683	156929
t_1 (s)	11823477	5381100	12171929
t_2 (s)	12928599	5899841	12795193
counts	7591	22412	27059
^{148}Gd prod σ (mb)	0.591±0.155	3.86±0.98	3.52±0.22

The ^{148}Gd production cross section measurements were not only calculated for the entire thickness of the foil, but also as a function of depth in the foil. By using the energy loss curve for alpha's through a material in Figure 8 and knowing the thickness of the material, the alpha energy at a particular depth could be determined. For each foil, the counts in each spectrum were summed from a particular energy (1.5, 1.75, 2.0, 2.25, 2.5, or 2.75 MeV) to 3.18 MeV and scaled by the percent depth to determine the cross section at that depth (Tables 18-20). The counts as a function of depth for the aluminum foils behind the single foils were also included. In general, the cross sections as a function of depth agree well within the uncertainty of the cross sections measured for the entire plateau.

Table 18: The ^{148}Gd production cross section as a function of depth for tantalum

range of counts (MeV)	^{148}Gd production cross section (mb)			
	Ta2 600 MeV stacked	Ta5 800 MeV stacked	Ta7 800 MeV single	Ta8 800 MeV single
E>2.75 MeV	15.2	30.2	28.2	37.2
E>2.50 MeV	15.1	30.5	27.8	34.2
E>2.25 MeV	15.1	30.3	27.2	32.0
E>2.00 MeV	15.1	30.2	26.9	31.0
E>1.75 MeV	15.1	30.0	26.7	30.3
E>1.50 MeV	14.9	28.6	26.3	28.4
entire plateau	15.2±4.0	29.7±7.6	27.6±1.7	28.6±7.3

Table 19: The ^{148}Gd production cross section as a function of depth for tungsten

range of counts (MeV)	^{148}Gd production cross section (mb)			
	W1 600 MeV stacked	W7 800 MeV stacked	W4 800 MeV single	W8 800 MeV single
E>2.75	9.12	21.3	18.2	20.4
E>2.50	9.28	21.1	18.9	20.3
E>2.25	9.29	21.0	19.2	20.1
E>2.00	9.31	21.0	19.4	20.2
E>1.75	9.33	20.9	19.5	20.1
E>1.50	9.23	20.7	19.5	19.8
entire plateau	8.31±0.92	19.5±1.2	18.0±1.1	20.7±5.3

Table 20: The ^{148}Gd production cross section as a function of depth for gold

range of counts (MeV)	^{148}Gd production cross section (mb)		
	Au2 600 MeV stacked	Au6 800 MeV stacked	Au7 800 MeV single
E>2.75	0.592	3.57	3.60
E>2.50	0.600	3.55	3.59
E>2.25	0.596	3.57	3.57
E>2.00	0.599	3.54	3.52
E>1.75	0.588	3.55	3.49
E>1.50	0.591	3.54	3.46
entire plateau	0.591±0.155	3.86±0.98	3.52±0.22

The ^{148}Gd production cross section measurements compared well with both previous measurements and theoretical estimates (Table 21). The production cross sections measured at 600 MeV were 15.2±4.0, 8.31±0.92, and 0.591±0.155 for Ta, W, and Au, respectively. The average production cross sections measured at 800 MeV were 28.6±3.5, 19.4±1.8, and 3.69±0.50 for Ta, W, and Au, respectively. The average measurement for W at 800 MeV was 18% higher than the previous measurement by Henry and the average for Au at 800 MeV was 2% less than the previous measurement by Rejmund, et al. Theoretically, Bertini better predicted the ^{148}Gd production than CEM2k+GEM2. Bertini ranged from 2-25% of the Ta and W measurements and 35-50% higher than the Au measurements. The CEM2k+GEM2 predictions were a factor of two to three higher than the measurements. The comparisons for both Bertini and CEM2k+GEM2 were best for Ta and worst for Au. This was possibly due in part to the fact that Ta is closer in nucleon number to Gd, compared to W and Au, and therefore it is easier to predict ^{148}Gd from the spallation of Ta.

Table 21: Cumulative ^{148}Gd production cross section measurements and comparisons to theoretical predictions and previous measurements

			^{148}Gd cumulative production cross section (mb)			
	Energy	Foil	Current	Previous	Theoretical	
Target	(MeV)	Setup	Measurement	Measurement	CEM2k+GEM2	Bertini
Ta	600	stacked	15.2±4.0		29.4±0.2	15.5±0.2
	800	stacked	29.7±7.6		45.6±0.3	24.4±0.3
		single	27.6±1.7			
		single	28.6±7.3			
W	600	stacked	8.31±0.92		21.6±0.3	10.9±0.2
	800	stacked	19.5±1.2		41.4±0.4	20.9±1.6
		single	18.0±1.1	16.4±0.8[a]		
		single	20.7±5.3			
Au	600	stacked	0.591±0.155		1.41±0.04	0.929±0.049
	800	stacked	3.86±0.98	3.74±0.19[b]	12.9±0.1	7.23±0.14
		single	3.52±0.22			

[a] [23] Henry *et al.* APT Internal Report, LLNL 1999.

[b] [29] Rejmund *et al. Nucl Phy A*683 2001 540-565.

5.3 Other radionuclide production cross sections

Many other radionuclides are produced from the spallation of heavy metals and were measured from the Ta, W, and Au foils. This section shows the results from counting with the γ-ray detector system.

Because the foils were too radioactive to handle immediately after irradiation, radionuclides with half-lifes less than 8 days were not considered in the analysis. Radionuclides with emission energies exclusively below 125 keV were also not considered. The ^{152}Eu source used to determine efficiency and energy calibrations of the system did not have a photon emission below 125 keV. In addition, x-rays interfered with photopeak determination below 80 keV.

Each foil was counted at least three times over a period of a few months to over a year, depending on the foil. Cross sections were measured at each emission energy line for a given radionuclide and a given foil. An average radionuclide production cross section was then produced from all the emission energy lines for all single and stacked foils of the same material at 600 and 800 MeV. The following criteria were given to a particular emission energy cross section: (1) the radionuclide must not have decayed more than five half-lifes, (2) no other radionuclide contaminated the emission energy of interest, and (3) if another radionuclide contaminated the emission energy peak of interest, then the contaminant must decay more than five half-lifes before considering the peak of interest. Tables 22-27 show all the cross sections determined for each radionuclide emission energy for W, Ta, and Au for the 600- and 800-MeV irradiations. Blank spaces in the tables indicate that no clean peak could be determined. Values in italics indicate clean peaks but possible contamination from other radionuclides or the radionuclide of interest had decayed over 5 half-lifes.

Some of the cross sections measured for a specific time looked unreasonable compared to cross sections at an earlier or later time period, or compared to neighboring radionuclide measurements. However, a contaminant could not be found and therefore the cross section measured was considered. Examples of this include ^{83}Rb in Table 22; ^{127}Xe and ^{133}Ba in Table 23; ^{83}Rb and ^{85}Sr in Table 24; ^{126}I and ^{131}I in Table 25; and ^{133}Ba in Table 27.

Table 22: Radionuclide production cross section measurements for Ta2 at 600 MeV as function of days after irradiation. Values in italics were not used in the average because of interference from other radionuclides or the radionuclide of interest had decayed over 5 half-lifes.

				cumulative production cross sections (mb)							
				Ta2 (25.3% uncertainty)							
				with plates					without plates		
	t_h	E_γ	branch ratio								
	(d)	(keV)	(%)	32 d	42 d	129 d	144 d	175 d	270 d	319 d	average
Sc-46	83.79	889.28	100.00	0.21	0.16	0.20	0.19	0.15	0.07		0.16
V-48	15.97	944.10	7.76			*0.00*	*0.00*	*0.00*	*0.00*	*0.00*	0.03
		983.52	100.00	0.02		*0.00*	*0.00*	*0.00*	*0.00*	*0.00*	
		1312.10	97.50	0.03	0.03	*0.45*	*0.00*	*0.00*	*0.00*	*0.00*	
Mn-54	312.30	834.85	100.00		0.08	0.19	0.17	0.16	0.16	0.17	0.15
Fe-59	44.50	1099.25	56.50		0.01			0.06	*0.00*	*0.00*	0.033
Zn-65	243.90	1115.55	50.60		0.47	0.48	0.24			0.28	0.37
As-74	17.78	595.85	59.00	0.46	0.20	*12.3*	*10.7*	*9.69*	*203*	*2E+03*	*0.33*
Se-75	119.78	264.66	58.90			0.29	0.40	0.42	0.55	0.70	0.93
		400.66	11.50	0.95	0.63	0.98	1.23	1.17	1.91	1.88	
Rb-83	86.20	520.39	44.70			0.26	0.34	0.35	0.30	0.28	2.34
		529.64	29.30		1.43	2.49		3.35	6.16	8.47	
Zr-88	83.40	392.87	100.00	0.13	0.08	0.18	0.14	0.17	0.19	0.15	0.15
Nb-95	34.98	765.79	100.00			0.20	0.26	*0.33*	*0.00*	*0.00*	0.23

(Table 22: Ta2, 600 MeV continued)

				cumulative production cross sections (mb)							
				Ta2 (25.3% uncertainty)							
				with plates					without plates		
	t_h (d)	E_γ (keV)	branch ratio (%)	32 d	42 d	129 d	144 d	175 d	270 d	319 d	average
Rh-102	207.00	556.41	96.00			0.21					0.21
Xe-127	36.40	202.86	68.30	*0.75*		1.81	2.29	3.91	*25.1*	*62.6*	*2.67*
		374.99	17.20						*0.00*	*0.00*	
Ba-131	11.80	496.33	47.00	0.70	0.58	*0.00*	*0.00*	*0.00*	*0.00*	*0.00*	0.64
Ce-139	137.64	165.85	79.90	1.38	1.11	1.40	1.31	1.40	1.37	1.60	1.37
Pm-146	2017.14	453.88	65.00	*24.2*	*14.7*	1.41	1.11	0.47			1.00
Eu-145	5.93	653.51	15.00	5.92	*5.24*	*0.00*	*0.00*	*0.00*	*0.00*	*0.00*	5.92
Eu-147	23.96	601.45	5.88			*32.9*	*0.00*	*0.00*	*0.00*	*0.00*	0.95
		677.52	9.80			*12.7*	*0.00*	*0.00*	*0.00*	*0.00*	
		1077.04	7.50	0.95	0.95	*11.5*	*0.95*	*0.95*	*0.95*	*0.95*	
Eu-148	54.51	414.04	20.50				0.60	0.56			0.93
		571.96	9.56	2.03	1.58						
		725.67	12.70								
		869.89	5.49	2.24	0.64						
		1033.99	7.77	0.51	0.45		0.49	0.23			
Eu-149	93.06	327.53	4.03	*10.1*	*9.86*	23.0	22.9	20.1	18.7	18.2	20.6

(Table 22: Ta2, 600 MeV continued)

				cumulative production cross sections (mb)							
				Ta2 (25.3% uncertainty)							
				with plates					without plates		
	t_h	E_γ	branch ratio								
	(d)	(keV)	(%)	32 d	42 d	129 d	144 d	175 d	270 d	319 d	average
Gd-149	9.38	149.74	48.20	15.0	11.0	*0.00*	*0.00*	*0.00*	*0.00*	*0.00*	13.3
		298.63	28.60	13.9	11.1	*122*	*0.00*	*0.00*	*0.00*	*0.00*	
		788.88	7.34	15.5	13.5	*928*	*0.00*	*0.00*	*0.00*	*0.00*	
Gd-151	123.96	174.70	2.96						11.8	15.9	13.8
Gd-153	241.60	97.43	27.60	*10.7*	*10.3*	21.6	19.0	20.8	13.0	22.2	19.3
Tm-167	9.24	207.80	41.00	55.4	51.1	*221*	*492*	*4E+03*	*4E+06*	*0.00*	53.3
Tm-168	93.10	184.24	17.50		2.64					1.00	1.30
		447.51	23.00	1.12	0.93	1.14	1.19	1.25	1.31	1.25	
		631.70	8.91							4.44	
		720.39	12.00								
		730.66	5.07			0.58	0.90	0.98		0.91	
		815.99	49.00	1.45	1.32	1.49	1.57	1.62	2.15	2.38	
		821.16	11.50	*0.00*	0.77	1.21	1.07	1.05	0.89	0.71	
		829.96	6.72	0.87	0.48	1.82	1.38	1.42	0.96		
Yb-169	32.01	130.52	11.30	49.1	47.7	65.8	65.4	*63.0*	*68.4*	*58.0*	59.1
		177.21	22.20	54.6	47.3	66.0	65.9	*66.7*	*73.1*	*80.7*	
		307.74	10.10	57.9	48.2	71.3	70.4	*72.4*	*92.4*	*118*	
Lu-171	8.24	667.40	11.00	76.4	73.5	*0.00*	*0.00*	*0.00*	*0.00*	*0.00*	69.2
		739.78	47.80	69.6	57.4	*0.00*	*0.00*	*0.00*	*0.00*	*0.00*	

(Table 22: Ta2, 600 MeV continued)

				cumulative production cross sections (mb)							
				Ta2 (25.3% uncertainty)							
				with plates					without plates		
	t_h	E_γ	branch ratio								
	(d)	(keV)	(%)	32 d	42 d	129 d	144 d	175 d	270 d	319 d	average
Lu-173	500.03	171.40	2.90	75.7	36.6	55.6	45.8	50.1	51.5	62.7	56.7
		272.00	21.20	64.5	48.3	59.3	60.9	59.7	60.9	62.0	
Lu-174	1208.70	1241.85	5.14		4.69	3.36	5.45	2.34	5.78	4.54	4.36
Hf-172	682.87	125.82	11.30			39.7					39.7
Hf-175	70.00	343.40	84.00	44.3	39.6	55.5	56.2	54.5	55.1	56.8	51.7
Hf-181	42.40	133.02	43.30						*0.00*	*0.00*	0.22
		482.18	80.50		0.08	0.22	0.26	0.31	*1.01*	*2.57*	
Ta-182	115.00	222.11	7.49	0.74			0.62		0.92	1.46	0.37
		1189.05	16.20			0.04	0.12				
		1221.41	27.00	0.32	0.21	0.16	0.22	0.18	0.19		
		1231.02	11.40				0.11	0.11	0.20		

Table 23: Radionuclide production cross section measurements for W1 at 600 MeV as function of days after irradiation. Values in italics were not used in the average because of interference from other radionuclides or the radionuclide of interest had decayed over 5 half-lifes.

				cumulative production cross sections (mb)							
				W1 (11.1% uncertainty)							
			branch	with plates				without plates			
	t_h	E_γ	ratio								
	(d)	(keV)	(%)	41 d	127 d	142 d	172 d	269 d	318 d	503 d	average
Sc-46	83.79	889.28	100.00	0.13	0.16	0.17	0.15	0.09	0.07	*0.00*	0.13
V-48	15.97	944.10	7.76		*0.00*	*0.00*	*0.00*	*0.00*	*0.00*	*0.00*	0.04
		983.52	100.00		*0.00*	*0.00*	*0.00*	*0.00*	*0.00*	*0.00*	
		1312.10	97.50	0.04	*0.00*	*0.00*	*0.00*	*0.00*	*0.00*	*0.00*	
Mn-54	312.30	834.85	100.00	0.18	0.06	0.16	0.14	0.18	0.17	0.18	0.15
Fe-59	44.50	1099.25	56.50		0.17	0.19	0.20	*0.11*	*0.28*	*0.00*	0.19
Zn-65	243.90	1115.55	50.60						0.30		0.30
As-74	17.78	595.85	59.00	0.32	*8.31*	*5.52*	*25.1*	*351*	*2E+03*	*9E+06*	0.32
Se-75	119.78	264.66	58.90		0.95	1.00	0.96	1.25	1.53	2.39	1.66
		400.66	11.50	0.45	1.07	1.26	1.32	1.91	2.38	5.09	
Rb-83	86.20	520.39	44.70		0.34	0.41	0.34	0.40	0.38	*0.20*	0.37
		529.64	29.30							*32.9*	
Y-88	106.60	898.04	93.70			0.42					0.42
Zr-88	83.40	392.87	100.00	0.18	0.22	0.21	0.20	0.20	0.19	*0.00*	0.20

(Table 23: W1, 600 MeV continued)

				cumulative production cross sections (mb)							
				W1 (11.1% uncertainty)							
			branch	with plates				without plates			
	t_h	E_γ	ratio								
	(d)	(keV)	(%)	41 d	127 d	142 d	172 d	269 d	318 d	503 d	average
Nb-95	34.98	765.79	100.00	0.34	0.28	0.38	0.43	*0.96*	*0.00*	*0.00*	0.36
Rh-102	207.00	556.41	96.00						0.29	0.41	0.35
Xe-127	36.40	202.86	68.30	*0.52*	2.37	2.68	4.37	*26.3*	*68.2*	*0.00*	3.14
		374.99	17.20	*0.00*				*0.00*	*0.00*	*0.00*	
Ba-131	11.80	496.33	47.00	0.57	*0.00*	*0.00*	*0.00*	*0.00*	*0.00*	*0.00*	0.57
Ba-133	3837.28	302.85	18.30								3.39
		356.02	62.00								
		383.85	8.94				3.39				
Ce-139	137.64	165.85	79.90	0.66	0.66	0.80	0.79	0.82	0.85	0.64	0.75
Pm-144	363.43	618.01	98.60						0.04	0.02	0.03
Pm-146	2017.14	453.88	65.00	*7.19*	0.61	0.59					0.60
Eu-148	54.51	414.04	20.50						*1.04*		0.64
		571.96	9.56								
		725.67	12.70								
		869.89	5.49	0.46		1.49					
		1033.99	7.77	0.23		0.50		0.51			
Eu-149	93.06	327.53	4.03	8.09	18.5	12.8	7.9	10.4	11.4		11.5

(Table 23: W1, 600 MeV continued)

				cumulative production cross sections (mb)							
				W1 (11.1% uncertainty)							
			branch	with plates				without plates			
	t_h	E_γ	ratio								
	(d)	(keV)	(%)	41 d	127 d	142 d	172 d	269 d	318 d	503 d	average
Gd-149	9.38	149.74	48.20	10.3	*0.00*	*0.00*	*0.00*	*0.00*	*0.00*	*0.00*	9.04
		298.63	28.60	9.05	*72.5*	*0.00*	*0.00*	*0.00*	*0.00*	*2E+13*	
		788.88	7.34	7.80	*0.00*	*0.00*	*0.00*	*0.00*	*0.00*	*1E+14*	
Gd-151	123.96	174.70	2.96						10.9	20.7	15.8
Gd-153	241.60	97.43	27.60		8.84	13.3	12.9	13.0	14.5	11.8	12.4
Tm-167	9.24	207.80	41.00	50.1	*142*	*203*	*3E+03*	*0.00*	*0.00*	*2E+13*	50.1
Tm-168	93.10	184.24	17.50						0.36	*0.00*	0.93
		447.51	23.00	0.45	0.65	0.62	0.61	0.52	0.58	*0.87*	
		631.70	8.91						4.42	*11.7*	
		720.39	12.00								
		730.66	5.07			0.44			0.93	*0.00*	
		815.99	49.00	0.86	1.01	1.07	1.11	1.65	1.94	*5.46*	
		821.16	11.50		0.56	0.52	0.48	0.75	0.70	*0.00*	
		829.96	6.72		0.92	0.66	0.64	1.13	0.67	*0.00*	
Yb-169	32.01	130.52	11.30	48.5	65.4	57.2	*55.0*	*53.1*	*58.5*	*0.00*	59.4
		177.21	22.20	51.0	68.7	54.4	*46.7*	*72.8*	*77.6*	*0.00*	
		307.74	10.10	56.9	68.5	64.0	*66.6*	*77.1*	*102*	*1E+03*	
Lu-173	499.69	171.40	18.50	*104*	49.6	48.6	43.3	56.7	62.9	54.1	57.8
		272.00	21.20	58.0	65.6	61.3	61.0	61.7	62.7	66.3	

(Table 23: W1, 600 MeV continued)

				cumulative production cross sections (mb)							
				W1 (11.1% uncertainty)							
			branch	with plates				without plates			
	t_h	E_γ	ratio								
	(d)	(keV)	(%)	41 d	127 d	142 d	172 d	269 d	318 d	503 d	average
Lu-174	1208.70	1241.85	5.14			1.33		1.60	1.64	1.89	1.62
Hf-172	682.40	125.82	11.30	*36.5*	*46.8*	*42.2*	*42.6*	49.0	49.8	51.0	49.9
Hf-175	70.00	343.40	84.00	55.7	63.2	60.2	58.8	58.1	60.4	*62.6*	59.4
Hf-181	42.40	133.02	43.30					*0.00*	*1.27*	*0.00*	1.17
		482.18	80.50	0.94	1.15	1.17	1.41	*2.22*	*3.96*	*54.0*	
Ta-182	115.00	222.11	7.49	8.68	12.5	11.4	11.2	12.2	12.2	14.8	11.6
		1189.05	16.20	11.3	12.2	11.4	11.3	11.1	11.4	11.7	
		1221.41	27.00	11.0	12.4	11.4	11.5	11.3	11.2	11.9	
		1231.02	11.40	11.1	12.3	11.5	11.4	11.3	11.4	11.1	
Re-183	70.02	162.33	23.30	3.03	2.88	2.54	2.57	2.48	2.80	6.34	3.23
Re-184	37.96	792.07	37.50	0.55	1.39	1.51	1.77	*3.87*	*7.34*	*75.3*	1.40
		894.76	15.60	2.69	0.48			*0.00*	*0.00*	*0.00*	
		903.28	37.90					*0.00*	*0.00*	*0.00*	

Table 24: Radionuclide production cross section measurements for Au2 at 600 MeV as function of days after irradiation. Values in italics were not used in the average because of interference from other radionuclides or the radionuclide of interest had decayed over 5 half-lifes.

				cumulative production cross sections (mb)						
				Au2 (26.3% uncertainty)						
	t_h	E_γ	branch ratio	with plates				without plates		
	(d)	(keV)	(%)	31 d	47 d	128 d	178 d	271 d	322 d	average
Sc-46	83.8	889.3	100.0		0.08	0.06	0.08	0.08	0.04	0.07
Mn-54	312.3	834.9	100.0			0.25	0.22	0.19	0.22	0.22
Fe-59	44.5	1099.3	56.5			0.44	0.33	*0.00*	*0.30*	0.38
Zn-65	243.9	1115.6	50.6	*2.39*	0.42	0.28	0.31	0.40	0.40	0.36
As-74	17.8	595.9	59.0	0.54	1.14	*6.95*	*0.00*	*0.00*	*0.00*	0.84
Se-75	119.8	264.7	58.9		0.67	0.77	0.78	0.91	1.00	1.07
		400.7	11.5			0.76	1.14	1.50	2.13	
Rb-83	86.2	520.4	44.7	*8.24*	*0.00*	1.45	1.54	1.64	1.72	2.87
		529.6	29.3	1.64	2.29	2.98	3.55	5.19	6.65	
Sr-85	64.8	514.0	96.0	3.13		1.94	1.89			2.32
Y-88	106.6	898.0	93.7	1.10		1.86	1.92	2.15		1.76
Zr-88	83.4	392.9	100.0	0.39	0.54	0.55	0.61	0.46	0.80	0.56
Nb-95	35.0	765.8	100.0	1.65	1.39	2.52	*3.83*	*9.27*	*14.9*	1.85

(Table 24: Au2, 600 MeV continued)

				cumulative production cross sections (mb)						
				Au2 (26.3% uncertainty)						
				with plates				without plates		
	t_h	E_γ	branch ratio							
	(d)	(keV)	(%)	31 d	47 d	128 d	178 d	271 d	322 d	average
Rh-102	207.0	556.4	96.0			0.15	0.13	0.17	0.17	0.15
Xe-127	36.4	202.9	68.3		0.48	1.75	3.52	*17.3*	*42.0*	2.21
		375.0	17.2			3.08		*0.00*	*0.00*	
Ba-131	11.8	496.3	47.0	2.61	3.61	*101*	*796*	*4E+04*	*2E+05*	3.11
Ba-133	3837.3	302.9	18.3							0.92
		356.0	62.0	*2E+03*	*313*					
		383.8	8.9	*2E+03*	*619*				0.92	
Eu-148	54.5	414.0	20.5				0.36	*0.00*	*0.00*	0.36
		572.0	9.6	*0.00*	*0.00*			*0.00*	*6.71*	
		725.7	12.7					*0.00*	*0.00*	
		869.9	5.5					*0.00*	*0.00*	
		1034.0	7.8					*0.00*	*0.00*	
Eu-149	93.1	327.5	4.0					6.22		6.22
Eu-150	13459.6	334.0	96.0	*2E+03*						3.23
		439.4	80.4							
		584.3	52.6					3.41	3.05	
Gd-149	9.4	149.7	48.2		1.82	*0.00*	*0.00*	*0.00*	*0.00*	1.82
		298.6	28.6			*0.00*	*0.00*	*0.00*	*0.00*	
		788.9	7.3			*0.00*	*0.00*	*0.00*	*0.00*	

(Table 24: Au2, 600 MeV continued)

	t_h (d)	E_γ (keV)	branch ratio (%)	cumulative production cross sections (mb) Au2 (26.3% uncertainty) with plates 31 d	47 d	128 d	178 d	without plates 271 d	322 d	average
Tm-168	93.1	184.2	17.5							1.31
		447.5	23.0	1.74	0.95					
		631.7	8.9			2.07	1.93	1.38	3.94	
		720.4	12.0							
		730.7	5.1							
		816.0	49.0		0.16	0.29	0.37	0.69	0.89	
		821.2	11.5							
		830.0	6.7	*85.8*	*27.5*					
Yb-169	32.0	130.5	11.3	27.7	24.3	26.6	*39.2*	*105*	*0.00*	24.7
		177.2	22.2	26.6	19.1	23.9	*18.2*	*27.4*	*0.00*	
Lu-171	8.2	667.4	11.0	40.4	*39.6*	*0.00*	*0.00*	*0.00*	*0.00*	39.8
		739.8	47.8	39.2	*36.5*	*0.00*	*0.00*	*0.00*	*0.00*	
Lu-173	500.0	171.4	18.5		38.9	35.0	27.6	35.3	37.7	35.1
		272.0	21.2	35.4	28.1	36.5	36.0	37.6	38.0	
Hf-172	682.9	125.8	11.3		*39.5*	*32.9*	*35.8*	33.6	32.0	32.8
Hf-175	70.0	343.4	84.0	47.6	35.0	44.9	42.6	43.3	45.3	43.1
Hf-181	42.4	133.0	43.3					*0.00*	*0.00*	0.40
		482.2	80.5			0.28	0.52	*2.04*	*4.32*	

(Table 24: Au2, 600 MeV continued)

				cumulative production cross sections (mb)						
				Au2 (26.3% uncertainty)						
				with plates				without plates		
	t_h	E_γ	branch ratio							
	(d)	(keV)	(%)	31 d	47 d	128 d	178 d	271 d	322 d	average
Ta-182	115.0	222.1	7.5						0.49	0.40
		1189.1	16.2							
		1221.4	27.0		0.07					
		1231.0	11.4	0.83	0.20					
Re-183	70.0	162.3	23.3	71.1	48.8	63.9	60.5	60.6	60.0	60.8
Re-184	38.0	792.1	37.5	0.33	0.60	1.07	1.83	*6.79*	*13.0*	0.96
		894.8	15.6							
		903.3	37.9							
Os-185	93.6	646.1	78.0	64.5	51.9	61.3	61.3	61.5	61.6	60.5
		874.8	6.3	60.2	58.0	60.6	59.8	61.8	62.0	
		880.5	5.2	*97.6*	*85.8*	*70.2*	60.3	60.7	61.4	
Ir-190	11.8	361.1	13.0	3.65	2.84	*0.00*	*0.00*	*0.00*	*0.00*	5.24
		397.4	6.5	5.59		*0.00*	*0.00*	*0.00*	*0.00*	
		407.2	28.5	6.68	3.71	*0.00*	*0.00*	*0.00*	*0.00*	
		518.6	34.0	7.39	6.81	*0.00*	*0.00*	*0.00*	*0.00*	
		569.3	28.5	*5.45*	*3.66*	*0.00*	*0.00*	*0.00*	*0.00*	
Ir-192	73.8	296.0	28.7	*3.80*	*2.36*	2.43	2.38	2.29	2.61	2.42
		308.5	30.0	*16.9*	*10.9*	*6.28*	4.45	3.02	2.79	
		316.5	82.8	1.91	1.67	2.30	2.35	2.42	2.40	
		468.1	47.8	2.19	2.03	2.17	2.23	2.09	2.18	
		604.4	8.2	*0.00*	*13.18*			2.59		

(Table 24: Au2, 600 MeV continued)

				cumulative production cross sections (mb)						
				Au2 (26.3% uncertainty)						
				with plates				without plates		
	t_h	E_γ	branch ratio							
	(d)	(keV)	(%)	31 d	47 d	128 d	178 d	271 d	322 d	average
Pt-188	10.2	195.1	18.6	47.3	41.3	*0.00*	*0.00*	*0.00*	*0.00*	49.4
		381.4	7.5	61.1	47.7	*0.00*	*0.00*	*0.00*	*0.00*	
Au-195	186.1	98.9	10.9	80.5	54.4	65.0	57.7	60.7	51.9	61.7

Table 25: Radionuclide production cross section measurements for Ta at 800 MeV as function of days after irradiation. Values in italics were not used in the average because of interference from other radionuclides or the radionuclide of interest had decayed over 5 half-lifes.

				cumulative production cross sections (mb)						
				Ta5 (25.5% uncertainty)						
	t_h	E_γ	branch ratio	with plates					without plates	
	(d)	(keV)	(%)	22 d	49 d	98 d	113 d	136 d	265 d	294 d
Sc-46	83.79	889.28	100.00	*8.13*	*4.26*	0.72	0.69	0.65	0.46	0.52
V-48	15.97	944.10	7.76			*0.00*	*0.00*	*0.00*	*0.00*	*0.00*
		983.52	100.00			*0.58*	*0.42*	*0.83*	*0.00*	*511*
		1312.10	97.50	0.41	0.46	*0.66*	*0.42*	*0.00*	*0.00*	*0.00*
Mn-54	312.30	834.85	100.00	*10.1*	1.05	0.92	0.85	0.85	0.81	0.78
Fe-59	44.50	1099.25	56.50	0.04					*0.00*	*0.00*
Zn-65	243.90	1115.55	50.60	*2.10*	*2.55*		0.59	0.47	1.19	0.97
As-74	17.78	595.85	59.00		0.51	*12.1*	*11.3*	*17.7*	*348*	*213*
Se-75	119.78	264.66	58.90	*23.6*	*18.2*	0.40	0.43	0.32	0.64	0.66
		400.66	11.50	*0.00*	*20.6*	2.15			0.63	2.00
Rb-83	86.20	520.39	44.70	4.65	3.87	0.22	0.51	0.35		0.58
		529.64	29.30			2.03	2.41	2.31	5.11	6.68
Y-88	106.60	898.04	93.70	4.79	2.21	5.07	4.88	5.02	8.91	10.3
Zr-88	83.40	392.87	100.00	*1.46*	*1.23*	0.30	0.28	0.34	0.25	0.39

(Table 25: Ta, 800 MeV continued)

				cumulative production cross sections (mb)						
				Ta5 (25.5% uncertainty)						
			branch	with plates					without plates	
	t_h	E_γ	ratio							
	(d)	(keV)	(%)	22 d	49 d	98 d	113 d	136 d	265 d	294 d
Nb-95	34.98	765.79	100.00	*2.40*	*0.69*	0.32	0.21	0.35	*0.00*	*0.00*
Rh-102	207.00	556.41	96.00	0.43	0.09	0.32	0.17	0.18	0.21	0.26
I-126	13.11	388.63	34.10			*0.00*	*0.00*	*0.00*	*0.00*	*0.00*
		753.82	4.16	55.6		*0.00*	*0.00*	*0.00*	*0.00*	*0.00*
I-131	8.02	284.31	6.14	10.4	*107*	*404*	*1E+03*	*8E+03*	*6E+08*	*9E+09*
		364.49	81.70		*0.00*	*23.3*	*47.4*	*0.00*	*0.00*	*2E+08*
		636.99	7.17		*0.00*	*6E+04*	*0.00*	*0.00*	*0.00*	*0.00*
Xe-127	36.40	374.99	17.20	*3.09*					*0.00*	*64.3*
Ba-131	11.80	496.33	47.00	1.03	2.65	*0.00*	*0.00*	*0.00*	*0.00*	*0.00*
Ba-133	3837.28	302.85	18.30	*1E+04*	*7E+03*					
		356.02	62.00						2.20	2.82
		383.85	8.94							
Ce-139	137.64	165.85	79.90		14.4	6.96	6.11	6.08	6.51	6.89
Pm-144	363.43	618.01	98.60	*3.79*	0.65					0.21
Pm-146	2017.14	453.88	65.00	9.86	4.05	4.69	2.64	1.44		
Eu-145	5.93	653.51	15.00	25.9	*329*	*0.00*	*0.00*	*0.00*	*0.00*	*0.00*

(Table 25: Ta, 800 MeV continued)

				cumulative production cross sections (mb)						
				Ta5 (25.5% uncertainty)						
			branch	with plates					without plates	
	t_h	E_γ	ratio							
	(d)	(keV)	(%)	22 d	49 d	98 d	113 d	136 d	265 d	294 d
Eu-147	23.96	601.45	5.88	*225*	*379*	53.8	59.3	*85.2*	*0.00*	*307*
		677.52	9.80	16.6	23.7	27.4	26.0	*28.9*	*0.00*	*0.00*
		1077.04	7.50	*1.11*	*2.26*	28.2	28.6	*28.8*	*0.00*	*0.00*
Eu-148	54.51	414.04	20.50			1.34	1.18	1.66		*0.00*
		571.96	9.56	*25.6*	*18.3*		1.95			*0.00*
		725.67	12.70	*215*	*200*					*206*
		869.89	5.49							*0.00*
		1033.99	7.77			1.09	0.85	0.95		*0.00*
Eu-149	93.06	327.53	4.03	35.4		44.5	40.6	42.0	37.6	42.3
Gd-149	9.38	149.74	48.20	48.3	*220*	*93.1*	*0.00*	*0.00*	*0.00*	*0.00*
		298.63	28.60	75.0	*421*	*80.1*	*60.9*	*0.00*	*0.00*	*0.00*
		788.88	7.34	27.5	*75.8*	*275*	*183*	*0.00*	*0.00*	*0.00*
Gd-151	123.96	174.70	2.96						23.0	23.3
Gd-153	241.60	97.43	27.60	*0.00*	*0.57*	34.0	31.1	30.4	34.0	36.1
Tm-168	93.10	184.24	17.50	*2.78*	*2.85*	1.53	1.01	0.79		1.27
		447.51	23.00			1.73	1.55	1.57	1.36	1.75
		631.70	8.91							5.80
		720.39	12.00							
		730.66	5.07					1.60		2.60
		815.99	49.00		*0.17*	1.60	1.58	1.67	2.10	

(Table 25: Ta, 800 MeV continued)

				cumulative production cross sections (mb)						
				Ta5 (25.5% uncertainty)						
			branch	with plates					without plates	
	t_h	E_γ	ratio							
	(d)	(keV)	(%)	22 d	49 d	98 d	113 d	136 d	265 d	294 d
Tm-168	93.10	821.16	11.50	*32.2*	*4.65*	1.27	1.46	1.18		1.78
		829.96	6.72				1.72	1.19		
Yb-169	32.01	130.52	11.30	*106*	*127*	58.9	56.5	54.4	*39.0*	*45.0*
		177.21	22.20	*0.30*	*0.54*	62.4	56.0	55.1	*67.0*	*56.3*
		307.74	10.10	*234*	*0.32*	65.3	60.8	62.6	*102*	*124*
Lu-173	500.03	171.40	18.50			98.4	42.5	40.2	39.7	52.3
		272.00	21.20	*6.79*	*3.76*	58.3	54.4	53.8	55.1	54.6
Lu-174	1208.70	1241.85	5.14						2.99	5.83
Hf-172	682.87	125.82	11.30	*1E+03*	*988*	*33.4*	*33.8*	*32.0*	34.6	37.2
Hf-175	70.00	343.40	84.00	*0.38*	*0.19*	52.5	48.2	47.6	48.6	49.7
Hf-181	42.40	133.02	43.30	*32.5*	*33.8*				*0.00*	*0.00*
		482.18	80.50			0.15	0.20	0.17	*1.05*	*1.94*
Ta-182	115.00	222.11	7.49	*83.5*	*28.3*			0.70		
		1189.05	16.20	1.28	1.31					
		1221.41	27.00	0.51						0.22
		1231.02	11.40	0.85			0.49			

(Table 25: Ta, 800 MeV continued)

				cumulative production cross sections (mb)						
				Ta7 (6.2% uncertainty)			Ta8 (25.5% uncertainty)			average
	t_h	E_γ	branch ratio	without plates			without plates			of Ta5,
	(d)	(keV)	(%)	58 d	86 d	148 d	59 d	87 d	182 d	Ta7, & Ta8
Sc-46	83.79	889.28	100.00	0.73	0.76	0.74	0.69	0.72	0.58	0.66
V-48	15.97	944.10	7.76		*0.00*	*0.00*		*0.00*	*0.00*	0.49
		983.52	100.00	0.52	*0.48*	*0.00*	0.51	*0.62*	*0.00*	
		1312.10	97.50	0.52	*0.50*	*0.00*	0.52	*0.53*	*0.00*	
Mn-54	312.30	834.85	100.00	0.96	1.10	1.10	0.94	1.04	1.10	0.96
Fe-59	44.50	1099.25	56.50	*0.18*	*0.20*	*0.22*	*0.18*	*0.22*	*0.20*	0.04
Zn-65	243.90	1115.55	50.60	0.80	0.66	0.52	0.79	0.63	0.46	0.71
As-74	17.78	595.85	59.00	0.46	0.59	*1.72*	0.40	0.51	*8.41*	0.49
		634.78	15.40			*2E+03*			*4E+03*	
Se-75	119.78	264.66	58.90	0.34	0.36	0.55	0.30	0.38	0.49	0.78
		400.66	11.50			0.81		1.78	0.94	
Rb-83	86.20	520.39	44.70	0.38	0.50	0.64	0.30	0.44	0.46	1.92
		529.64	29.30		2.34	2.77	1.10	1.69	2.94	
Y-88	106.60	898.04	93.70	4.09	4.07	4.86	3.82	3.73	5.09	5.14
Zr-88	83.40	392.87	100.00	0.27	0.29	0.33	0.28	0.29	0.31	0.30

(Table 25: Ta, 800 MeV continued)

				cumulative production cross sections (mb)						
				Ta7 (6.2% uncertainty)			Ta8 (25.5% uncertainty)			average
			branch	without plates			without plates			of Ta5,
	t_h	E_γ	ratio	58 d	86 d	148 d	59 d	87 d	182 d	Ta7, & Ta8
	(d)	(keV)	(%)							
Nb-95	34.98	765.79	100.00	0.16	0.21	0.31	0.21	0.18	*0.45*	0.24
Rh-102	207.00	556.41	96.00	0.11	0.18	0.14	0.09	0.12	0.16	0.19
I-126	13.11	388.63	34.10		*0.00*	*0.00*		*0.00*	*0.00*	55.6
		753.82	4.16		*0.00*	*75.1*		*0.00*	*0.00*	
I-131	8.02	284.31	6.14	*11.4*	*129*	*2E+04*	*7.47*	*176*	*4E+05*	10.4
		364.49	81.70		*16.3*	*1E+03*		*0.00*	*0.00*	
		636.99	7.17		*2E+04*	*2E+06*		*0.00*	*0.00*	
Xe-127	36.40	374.99	17.20	0.97			0.95		*0.00*	0.96
Ba-131	11.80	496.33	47.00	2.33	*2.39*	*0.00*	2.19	*2.17*	*0.00*	2.05
Ba-133	3837.28	302.85	18.30			2.08				2.15
		356.02	62.00			2.24			1.40	
		383.85	8.94							
Ce-139	137.64	165.85	79.90	5.70	6.09	6.79	5.47	5.71	5.93	6.89
Pm-144	363.43	618.01	98.60	0.19	0.16	0.26		0.24	0.22	0.28
Pm-146	2017.14	453.88	65.00	10.5	5.25	1.59	9.75	4.75	0.49	5.00
Eu-145	5.93	653.51	15.00	*19.0*	*78.6*	*0.00*	*15.8*	*0.00*	*0.00*	25.9

(Table 25: Ta, 800 MeV continued)

				cumulative production cross sections (mb)						
				Ta7 (6.2% uncertainty)			Ta8 (25.5% uncertainty)			average
			branch	without plates			without plates			of Ta5,
	t_h	E_γ	ratio							
	(d)	(keV)	(%)	58 d	86 d	148 d	59 d	87 d	182 d	Ta7, & Ta8
Eu-147	23.96	601.45	5.88	23.6	25.7	*5.83*	22.5	24.3	*29.7*	27.3
		677.52	9.80	22.8	24.2	*35.2*	21.2	23.1	*25.6*	
		1077.04	7.50	24.0	24.6	*34.8*	22.7	23.5	*22.5*	
Eu-148	54.51	414.04	20.50			1.38		1.15	1.31	1.44
		571.96	9.56	3.50	2.57	1.91	3.02	2.15	1.36	
		725.67	12.70							
		869.89	5.49	1.10	0.81	1.77	0.92	1.26	1.38	
		1033.99	7.77	0.99	0.73	1.09	0.82	0.70		
Eu-149	93.06	327.53	4.03	26.2	28.9	34.1	28.6	28.8	31.3	35.0
Gd-149	9.38	149.74	48.20	*24.9*	*29.1*	*0.00*	*23.5*	*45.6*	*0.00*	50.3
		298.63	28.60	*24.7*	*27.4*	*0.00*	*23.2*	*26.5*	*0.00*	
		788.88	7.34	*29.5*	*27.7*	*0.00*	*27.0*	*39.0*	*0.00*	
Gd-151	123.96	174.70	2.96	*568*		22.6	*532*		15.3	21.1
Gd-153	241.60	97.43	27.60	22.4	28.7	32.6	21.3	26.5	30.0	29.7
Tm-168	93.10	184.24	17.50			1.40				1.75
		447.51	23.00	1.37	1.45	1.61	1.05	1.26	1.31	
		631.70	8.91			9.56			6.77	
		720.39	12.00	2.21			5.69			
		730.66	5.07	0.45	1.10	1.47	0.99	0.90	0.86	
		815.99	49.00	1.39	1.46	1.68	1.35	1.41	1.58	

(Table 25: Ta, 800 MeV continued)

				cumulative production cross sections (mb)						
				Ta7 (6.2% uncertainty)			Ta8 (25.5% uncertainty)			average
	t_h	E_γ	branch ratio	without plates			without plates			of Ta5,
	(d)	(keV)	(%)	58 d	86 d	148 d	59 d	87 d	182 d	Ta7, & Ta8
Tm-168	93.10	821.16	11.50	0.98	1.22	1.37	0.95	1.11	1.09	
		829.96	6.72	1.03	1.20	1.32	0.95	1.11	1.15	
Yb-169	32.01	130.52	11.30	44.1	51.7	69.2	42.6	49.2	*46.9*	55.8
		177.21	22.20	50.3	54.1	71.0	47.9	51.4	*51.9*	
		307.74	10.10	48.6	54.2	75.5	46.1	52.4	*62.1*	
Lu-173	500.03	171.40	18.50	70.3	53.9	54.8	65.8	51.9	35.9	53.4
		272.00	21.20	48.5	50.9	51.0	45.6	48.3	48.1	
Lu-174	1208.70	1241.85	5.14		4.41	2.84		9.00	2.55	4.60
Hf-172	682.87	125.82	11.30	*21.8*	*28.2*	*32.2*	*19.2*	*26.9*	33.9	29.9
Hf-175	70.00	343.40	84.00	39.5	41.7	51.3	37.5	43.1	43.8	45.8
Hf-181	42.40	133.02	43.30	0.22	0.35		0.13			0.18
		482.18	80.50	0.11	0.14	0.21	0.03	0.14	0.30	
Ta-182	115.00	222.11	7.49			0.60	0.49	0.69	0.80	0.30
		1189.05	16.20	0.14	0.08	0.18	0.03	0.23		
		1221.41	27.00	0.17	0.14	0.21	0.21	0.15	0.13	
		1231.02	11.40		0.17	0.25	0.25		0.22	

Table 26: Radionuclide production cross section measurements for W at 800 MeV as function of days after irradiation. Values in italics were not used in the average because of interference from other radionuclides or the radionuclide of interest had decayed over 5 half-lifes.

				cumulative production cross sections (mb)					
				W7 (6.2% uncertainty)					
			branch	with plates			without plates		
	t_h	E_γ	ratio						
	(d)	(keV)	(%)	28 d	48 d	92 d	182 d	223 d	392 d
Sc-46	83.79	889.28	100.00	0.51	0.52	0.43	0.36	0.33	0.16
V-48	15.97	944.10	7.76				*0.00*	*0.00*	*0.00*
		983.52	100.00	0.10	0.11	*0.14*	*0.00*	*0.00*	*0.00*
		1312.10	97.50	0.12	0.13	*0.17*	*0.00*	*0.00*	*0.00*
Mn-54	312.30	834.85	100.00	0.46	0.39	0.33	0.39	0.37	0.41
Fe-59	44.50	1099.25	56.50	0.18	0.18	0.24	0.24	0.20	*0.00*
Zn-65	243.90	1115.55	50.60	0.71	0.80	0.62	0.51	0.48	
Se-75	119.78	264.66	58.90		1.13	1.08	1.32	1.34	1.98
		400.66	11.50				1.36	1.58	3.14
Rb-83	86.20	520.39	44.70	0.20	0.45	0.64	0.66	0.69	0.33
		529.64	29.30	2.13	1.73	2.46	3.90	4.86	14.0
Y-88	106.60	898.04	93.70			0.63		0.31	
Zr-88	83.40	392.87	100.00	0.31	0.34	0.36	0.38	0.36	0.50
Nb-95	34.98	765.79	100.00		0.31	0.28	*0.52*	*0.63*	*15.7*
Rh-102	207.00	556.41	96.00	0.20	0.08	0.17	0.19		
I-126	13.11	388.63	34.10				*0.00*	*0.00*	*0.00*
		753.82	4.16				*0.00*	*0.00*	*0.00*
Ba-131	11.80	496.33	47.00	1.92	1.87	*3.93*	*45.5*	*0.00*	*0.00*
Ba-133	3837.28	302.85	18.30				1.30	1.50	1.57
		356.02	62.00				1.39	1.44	1.34
		383.85	8.94		10.3		2.40	2.14	
Ce-139	137.64	165.85	79.90	2.95	3.89	4.29	4.49	4.74	4.31
Pm-144	363.43	618.01	98.60				0.15	0.22	0.15

(Table 26: W, 800 MeV continued)

				cumulative production cross sections (mb)					
				W7 (6.2% uncertainty)					
			branch	with plates			without plates		
	t_h	E_γ	ratio						
	(d)	(keV)	(%)	28 d	48 d	92 d	182 d	223 d	392 d
Eu-145	5.93	653.51	15.00	11.1	*11.0*	*0.00*	*0.00*	*0.00*	*0.00*
Eu-147	23.96	601.45	5.88	24.9	20.9	24.8	*39.5*	*49.5*	*0.00*
		677.52	9.80	23.3	19.4	20.1	*21.5*	*23.4*	*0.00*
		1077.04	6.15	24.0	19.6	19.7	*21.1*	*16.8*	*0.00*
Eu-148	54.51	414.04	20.50	0.68	0.93	0.86	0.96	0.76	*0.00*
		571.96	9.56		3.40	1.76	1.33	1.35	*0.00*
		725.67	12.70						*0.00*
		869.89	5.49	1.12	0.77	0.67	0.79		*0.00*
		1033.99	7.77	0.60	0.80	0.67	0.88	0.81	*0.00*
Eu-149	93.06	277.09	3.55	21.4	22.0	25.1	25.0	25.9	30.7
		327.53	4.03	24.2	22.1	28.3	26.0	26.3	28.4
Gd-149	9.38	149.74	48.20	20.5	22.8	*0.00*	*0.00*	*0.00*	*0.00*
		298.63	28.60	21.1	20.8	*23.1*	*0.00*	*0.00*	*0.00*
		788.88	7.34	12.2	21.5	*0.00*	*0.00*	*0.00*	*0.00*
Gd-151	123.96	174.70	2.96					11.0	24.3
Gd-153	241.60	97.43	27.60	21.6	18.6	19.8	27.3	27.0	28.8
Tm-168	93.10	184.24	17.50					0.30	
		447.51	23.00	0.96	1.05	0.76	0.87	0.88	0.79
		730.66	5.07		0.21	0.86	0.48	0.53	
		815.99	49.00	1.01	1.04	0.99	1.31	1.45	2.92
		821.16	11.50	0.56	0.70	0.62	0.76	0.77	
		829.96	6.72		0.78	0.51	0.81	0.75	
Yb-169	32.01	130.52	11.30	56.4	54.8	54.6	*54.0*	*58.2*	*0.00*
		177.21	22.20	57.9	56.5	52.6	*64.0*	*42.9*	*0.00*
		307.74	10.10	59.5	57.3	58.6	*68.7*	*74.9*	*347*
Lu-171	8.24	739.78	47.80	60.0	*62.6*	*0.00*	*0.00*	*0.00*	*0.00*
Lu-173	499.69	171.40	18.50	37.0	46.9	67.8	52.0	48.3	52.7
		272.00	21.20	83.5	61.4	56.1	57.3	57.0	58.2
Lu-174	1208.70	1241.85	5.14				1.99	1.63	2.19
Hf-172	682.40	125.82	11.30	*28.7*	*34.9*	*39.4*	41.3	43.1	45.1

(Table 26: W, 800 MeV continued)

				cumulative production cross sections (mb)					
				W7 (6.2% uncertainty)					
	t_h	E_γ	branch ratio	with plates			without plates		
	(d)	(keV)	(%)	28 d	48 d	92 d	182 d	223 d	392 d
Hf-175	70.00	343.40	84.00	53.4	51.9	53.6	54.5	54.3	*54.1*
Hf-181	42.40	133.02	43.30					*1.23*	*0.00*
		482.18	80.50	1.30	1.26	1.26	1.55	*1.90*	*13.5*
Ta-182	115.00	222.11	7.49	13.6	12.5	12.8	13.7	13.7	13.6
		1189.05	16.20	13.0	12.8	13.0	12.7	12.7	12.6
		1221.41	27.00	13.4	13.0	13.1	12.9	12.8	13.2
		1231.02	11.40	13.3	13.1	13.5	13.0	14.8	13.1
Re-183	70.02	162.33	23.30	1.80	1.22	2.19	2.08	2.12	*2.63*
Re-184	37.96	792.07	37.50	0.86	1.00	1.08	1.70	*2.27*	*15.4*
		894.76	15.60	*18.5*	3.43			*1.91*	*0.00*
		903.28	37.90						*0.00*

(Table 26: W, 800 MeV continued)

				cumulative production cross sections (mb)									
				W4 (6.2% uncertainty)				W8 (25.5% uncertainty)					average
			branch	without plates				without plates					of W7,
	t_h	E_γ	ratio										
	(d)	(keV)	(%)	56 d	93 d	123 d	176 d	57 d	80 d	122 d	185 d	315 d	W4, & W8
Sc-46	83.79	889.28	100.00	0.53	0.54	0.51	0.45	0.58	0.58	0.55	0.51	0.35	0.46
V-48	15.97	944.10	7.76			*0.00*	*0.00*			*0.00*	*0.00*	*0.00*	0.27
		983.52	100.00	0.30	*0.26*	*0.00*	*0.00*	0.41	0.40	*0.50*	*0.00*	*0.00*	
		1312.10	97.50		*0.37*	*0.25*	*0.00*	0.42	0.43	*0.56*	*0.00*	*0.00*	
Mn-54	312.30	834.85	100.00	*0.60*	*0.73*	*0.70*	*0.72*	*0.82*	*0.87*	*0.89*	*0.90*	*0.91*	0.39
Fe-59	44.50	1099.25	56.50	0.19	0.19	0.22	0.20	0.20	0.22	0.26	0.20	*0.00*	0.21
Zn-65	243.90	1115.55	50.60	0.67	0.58	0.77	0.48	0.49	0.59	0.51	0.50		0.59
Se-75	119.78	264.66	58.90	0.99	0.91	1.11	1.20		0.94	1.13	1.17	1.51	1.28
		400.66	11.50		0.80	0.89	1.10		0.80	0.93	1.16	1.97	
Rb-83	86.20	520.39	44.70	0.39	0.62	0.64	0.60	0.47	0.59	0.64	0.55	0.41	2.17
		529.64	29.30	1.67	2.20	2.54	3.33	2.87	1.99	2.47	3.50	7.59	
Y-88	106.60	898.04	93.70	4.18	0.59	4.81	0.68	4.23	0.55	4.73	6.25		2.70
Zr-88	83.40	392.87	100.00	0.31	0.33	0.32	0.34	0.33	0.32	0.32	0.34	0.40	0.35
Nb-95	34.98	765.79	100.00	0.26	0.23	0.32	*0.45*	0.24	0.26	0.31	*0.46*	*4.29*	0.28
Rh-102	207.00	556.41	96.00	0.09	0.13	0.20	0.18	0.08	0.12	0.14	0.18		0.15

(Table 26: W, 800 MeV continued)

				cumulative production cross sections (mb)									
				W4 (6.2% uncertainty)				W8 (25.5% uncertainty)					average
			branch	without plates				without plates					of W7,
	t_h	E_γ	ratio										
	(d)	(keV)	(%)	56 d	93 d	123 d	176 d	57 d	80 d	122 d	185 d	315 d	W4, & W8
I-126	13.11	388.63	34.10			*0.00*	*0.00*			*0.00*	*0.00*	*0.00*	0.60
		753.82	4.16	0.74		*0.00*	*0.00*	0.46		*0.00*	*0.00*	*0.00*	
Ba-131	11.80	496.33	47.00	1.79	*3.48*	*7.67*	*38.9*	1.73	*2.79*	*7.97*	*0.00*	*0.00*	1.83
Ba-133	3837.28	302.85	18.30				2.17			2.03		0.10	2.06
		356.02	62.00				0.84			1.02	0.81	0.73	
		383.85	8.94	3.97			1.59			2.59			
Ce-139	137.64	165.85	79.90	3.44	3.85	4.20	4.06	3.42	3.91	4.19	3.98	3.87	3.97
Pm-144	363.43	618.01	98.60	0.13	0.13	0.18	0.15		0.13	0.17	0.10	0.17	0.15
Eu-145	5.93	653.51	15.00	*12.3*	*0.00*	*0.00*	*0.00*	*10.0*	*0.00*	*0.00*	*0.00*	*0.00*	11.1
Eu-147	23.96	601.45	5.88	17.3	19.3	*19.7*	*25.1*	17.4	18.7	*20.5*	*23.2*	*0.00*	19.5
		677.52	9.80	16.4	18.2	*18.6*	*20.3*	16.3	18.1	*18.7*	*19.6*	*0.00*	
		1077.04	6.15	17.3	18.1	*20.6*	*17.5*	17.6	18.1	*18.6*	*17.5*	*0.00*	
Eu-148	54.51	414.04	20.50	0.79	0.74	0.84	0.83	0.73	0.77	0.75	0.82	*0.00*	0.94
		571.96	9.56		1.32	1.26	1.07		1.94	1.31	1.35	*0.00*	
		725.67	12.70									*0.00*	
		869.89	5.49	0.69	0.56	0.77	0.70	0.78	0.76	0.75	0.74	*0.00*	
		1033.99	7.77	0.46	0.59	0.70	0.72	0.62	0.85	1.00	0.69	*0.00*	

(Table 26: W, 800 MeV continued)

				cumulative production cross sections (mb)									
				W4 (6.2% uncertainty)				W8 (25.5% uncertainty)					average
			branch	without plates				without plates					of W7,
	t_h	E_γ	ratio										
	(d)	(keV)	(%)	56 d	93 d	123 d	176 d	57 d	80 d	122 d	185 d	315 d	W4, & W8
Eu-149	93.06	277.09	3.55	19.2	22.7	23.0	22.8		20.2	22.4	22.8	26.4	23.9
		327.53	4.03	20.3	22.6	23.8	25.0	22.6	23.7	24.0	20.0	26.3	
Gd-149	9.38	149.74	48.20	*18.7*	*7.96*	*33.3*	*0.00*	*19.4*	*25.8*	*30.2*	*0.00*	*0.00*	19.8
		298.63	28.60	*18.6*	*19.8*	*0.00*	*0.00*	*17.9*	*20.0*	*38.6*	*0.00*	*0.00*	
		788.88	7.34	*20.6*	*0.00*	*0.00*	*0.00*	*20.8*	*0.00*	*0.00*	*0.00*	*0.00*	
Gd-151	123.96	174.70	2.96			15.3	8.21	*522*		13.1	7.95	18.7	14.1
Gd-153	241.60	97.43	27.60	15.0	19.5	25.5	25.4	14.1	19.9	25.2	25.0	30.3	22.9
Tm-168	93.10	184.24	17.50			0.64				0.40			0.79
		447.51	23.00	0.69	0.81	0.82	0.75	0.65	0.75	0.71	0.74	1.01	
		730.66	5.07	0.29	0.72	0.65	0.40	0.41		0.63	0.73	0.45	
		815.99	49.00	0.87	0.99	1.05	1.14	0.92	0.95	1.03	1.13	1.76	
		821.16	11.50	0.53	0.69	0.70	0.65	0.54	0.64	0.75	0.64	0.66	
		829.96	6.72	0.41	0.75	0.79	0.66	0.76	0.55	0.82	0.79	1.65	
Yb-169	32.01	130.52	11.30	43.8	51.3	56.0	*50.3*	41.4	52.0	55.3	*48.3*	*25.7*	53.2
		177.21	22.20	51.8	55.3	55.9	*58.2*	45.2	54.3	53.3	*58.6*	*0.00*	
		307.74	10.10	44.1	54.5	57.8	*61.8*	45.8	54.0	57.3	*62.1*	*127*	
Lu-171	8.24	739.78	47.80	*61.6*	*0.00*	*4E+03*	*0.00*	*63.8*	*60.4*	*0.00*	*0.00*	*0.00*	60.0
Lu-173	499.69	171.40	18.50	51.0	45.9	51.8	38.0	58.8	53.4	53.9	38.2	49.3	52.3
		272.00	21.20	48.5	50.6	51.1	51.4	43.6	50.5	50.8	50.9	53.1	

(Table 26: W, 800 MeV continued)

				cumulative production cross sections (mb)									
				W4 (6.2% uncertainty)				W8 (25.5% uncertainty)					average
			branch	without plates				without plates					of W7,
	t_h	E_γ	ratio										
	(d)	(keV)	(%)	56 d	93 d	123 d	176 d	57 d	80 d	122 d	185 d	315 d	W4, & W8
Lu-174	1208.70	1241.85	5.14				1.68					2.18	1.94
Hf-172	682.40	125.82	11.30	*25.9*	*33.5*	*42.1*	*37.0*	*25.4*	*34.4*	*41.6*	36.4	39.5	41.1
Hf-175	70.00	343.40	84.00	43.4	48.5	49.3	49.8	40.4	47.9	48.8	48.8	45.6	49.3
Hf-181	42.40	133.02	43.30	0.23		1.02		0.21		1.09		*0.00*	1.11
		482.18	80.50	1.11	1.14	1.28	1.43		1.14	1.26	1.35	*3.49*	
Ta-182	115.00	222.11	7.49	10.3	12.1	12.5	12.5	9.97	11.7	12.1	12.3	12.8	12.2
		1189.05	16.20	11.0	11.3	11.5	11.5	11.1	11.3	11.5	11.5	11.8	
		1221.41	27.00	11.0	11.4	11.7	11.6	10.7	11.4	11.4	11.5	11.9	
		1231.02	11.40	11.2	11.4	11.6	11.7	11.3	11.7	11.5	11.5	12.1	
Re-183	70.02	162.33	23.30		1.42	2.09	2.07	1.69	1.51	1.84	2.07	2.02	1.86
Re-184	37.96	792.07	37.50	0.91	0.98	1.11	1.49		0.97	1.06	1.58	*5.66*	1.34
		894.76	15.60	1.89		0.85		1.62		0.97		*0.00*	
		903.28	37.90									*0.00*	

Table 27: Radionuclide production cross section measurements for Au at 800 MeV as function of days after irradiation. Values in italics were not used in the average because of interference from other radionuclides or the radionuclide of interest had decayed over 5 half-lifes.

				cumulative production cross sections (mb)				
				Au6 (25.5% uncertainty)				
	t_h	E_γ	branch ratio	with plates			without plates	
	(d)	(keV)	(%)	29 d	49 d	93 d	188 d	225 d
Sc-46	83.79	889.28	100.00	0.07	0.11	0.16	0.18	0.15
V-48	15.97	944.10	7.76			*0.00*	*0.00*	*0.00*
		983.52	100.00			*0.00*	*0.00*	*0.00*
		1312.10	97.50	0.04	0.02	*0.00*	*0.00*	*0.00*
Mn-54	312.30	834.85	100.00	0.31	0.31	0.27	0.30	0.30
Fe-59	44.50	1099.25	56.50		0.44	0.32	0.44	*0.39*
Zn-65	243.90	1115.55	50.60	0.59	0.48	0.55	0.54	0.54
As-74	17.78	595.85	59.00	1.31	1.09	*1.18*	*0.00*	*0.00*
Se-75	119.78	264.66	58.90	0.89	0.83	1.04	1.07	1.17
		400.66	11.50		1.30	1.29	1.69	1.85
Rb-83	86.20	520.39	44.70	*8.15*	*2.71*	1.81	1.95	2.03
		529.64	29.30	2.40	2.94	2.75	3.60	4.78
Sr-85	64.84	514.01	96.00		1.62	2.27	2.18	2.09
Y-88	106.60	898.04	93.70	1.52	1.63	1.98	2.31	2.63
Nb-95	34.98	765.79	100.00	1.31	1.34	1.76	*3.52*	*4.88*
Rh-102	207.00	556.41	96.00				0.15	
I-126	13.11	388.63	34.10			*0.00*	*0.00*	*0.00*
		753.82	4.16			*0.00*	*0.00*	*0.00*
Ba-131	11.80	496.33	47.00	1.99	3.69	*21.6*	*983*	*5E+03*
Ba-133	3837.28	302.85	18.30					
		356.02	62.00					
		383.85	8.94					
Ce-139	137.64	165.85	79.90	0.09		0.20	0.42	0.58

(Table 27: Au, 800 MeV continued)

				cumulative production cross sections (mb)				
				Au6 (25.5% uncertainty)				
	t_h	E_γ	branch ratio	with plates			without plates	
	(d)	(keV)	(%)	29 d	49 d	93 d	188 d	225 d
Eu-145	5.93	653.51	15.00	1.17	*0.00*	*0.00*	*0.00*	*0.00*
Eu-147	23.96	601.45	5.88	3.38	4.00	4.38	*33.2*	*78.6*
		677.52	9.80	2.61	2.91	2.96	*7.72*	*19.9*
Eu-148	54.51	414.04	20.50					
		571.96	9.56	*4.02*	*2.35*	1.63	1.87	2.87
		725.67	12.70					
		869.89	5.49	0.87				
		1033.99	7.77					
Eu-149	93.06	327.53	4.03	5.21	6.22	6.96	9.33	9.35
Gd-149	9.38	149.74	48.20	4.21	*4.39*	*0.00*	*0.00*	*0.00*
		298.63	28.60	3.27	*2.67*	*0.00*	*0.00*	*0.00*
		788.88	7.34	2.46	*3.06*	*0.00*	*0.00*	*0.00*
Gd-151	123.96	174.70	2.96					2.31
Tm-168	93.10	184.24	17.50					
		447.51	23.00		0.24			0.13
		631.70	8.91	*187*				
		720.39	12.00					
		730.66	5.07					
		815.99	49.00	0.18	0.23	0.30	0.52	0.58
		821.16	11.50					
		829.96	6.72	*56.4*	*17.6*	1.07		
Yb-169	32.01	130.52	11.30	34.9	34.1	35.7	*48.0*	*57.2*
		177.21	22.20	33.0	32.5	32.5	*29.0*	*32.5*
Lu-171	8.24	739.78	47.80	38.5	*38.9*	*35.6*	*0.00*	*0.00*
Lu-173	500.03	171.40	18.50	*79.8*	*66.2*	37.6	36.9	42.0
		272.00	21.20	43.4	39.6	42.1	42.4	43.0
Hf-172	682.87	125.82	11.30	*35.6*	*39.0*	*39.3*	36.8	35.6
Hf-175	70.00	343.40	84.00	43.6	43.5	42.6	42.0	45.9

(Table 27: Au, 800 MeV continued)

				cumulative production cross sections (mb)				
				Au6 (25.5% uncertainty)				
	t_h	E_γ	branch ratio	with plates			without plates	
	(d)	(keV)	(%)	29 d	49 d	93 d	188 d	225 d
Hf-181	42.40	133.02	43.30					*0.00*
		482.18	80.50		0.09	0.21	0.67	*1.40*
Ta-182	115.00	222.11	7.49	3.00	0.94		0.48	0.65
		1189.05	16.20					
		1221.41	27.00					
		1231.02	11.40	0.40	0.42			
Re-183	70.02	162.33	23.30	51.7	49.2	49.7	47.1	50.6
Re-184	37.96	792.07	37.50	0.49	0.49	0.82	2.36	*3.83*
		894.76	15.60	*2.18*	0.68			*4.33*
		903.28	37.90					*0.00*
Os-185	93.63	646.12	78.00	48.5	48.2	48.0	48.8	49.6
		874.81	6.29	48.4	50.3	50.6	49.1	49.6
		880.52	5.17	*91.0*	*74.4*	*63.3*		50.3
Ir-190	11.78	361.14	13.00	2.53	3.10	*0.00*	*0.00*	*0.00*
		371.26	23.00	3.93	4.05	*15.2*	*3E+03*	*0.00*
		397.39	6.54	3.58	3.93	*0.00*	*0.00*	*0.00*
		407.24	28.50	3.77	3.86	*0.00*	*0.00*	*0.00*
		518.55	34.00	6.53	5.96	*0.00*	*0.00*	*0.00*
		569.31	28.50	3.65	3.69	*2.96*	*0.00*	*0.00*
Ir-192	73.83	295.96	28.70	*1.04*	*2.54*	2.21	2.20	2.44
		316.51	82.80	2.16	2.24	2.32	2.31	2.43
		468.07	47.80	2.15	2.21	2.29	2.20	2.30
		604.41	8.23	*27.9*	*12.3*	2.06	2.57	2.47
Pt-188	10.19	195.05	18.60	32.6	32.9	*0.00*	*0.00*	*0.00*
		381.43	7.50	32.5	30.6	*0.00*	*0.00*	*0.00*
Au-196	6.18	426.00	7.00	48.2	*0.00*	*0.00*	*0.00*	*0.00*

Table 27: Au, 800 MeV continued)

				cumulative production cross sections (mb)							
				Au5 (25.5% uncertainty)				Au7 (6.2% uncertainty)			average
				without plates						with plates	of Au6,
	t_h	E_γ	branch ratio								
	(d)	(keV)	(%)	63 d	84 d	120 d	151 d	52 d	81 d	115 d	Au5, & Au7
Sc-46	83.79	889.28	100.00	*0.37*	*0.41*	*0.45*	*0.39*	*0.38*	*0.40*	*0.45*	0.14
V-48	15.97	944.10	7.76		*0.00*	*0.00*	*0.00*		*0.00*	*0.00*	0.03
		983.52	100.00	*0.42*	*0.45*	*0.58*	*0.00*	*0.40*	*0.49*	*0.40*	
		1312.10	97.50	*0.44*	*0.49*	*0.66*	*0.46*	*0.43*	*0.46*	*0.44*	
Mn-54	312.30	834.85	100.00	*0.98*	*1.05*	*1.09*	*1.08*	*0.97*	*1.00*	*1.25*	0.30
Fe-59	44.50	1099.25	56.50	0.27	0.51	0.50	0.46	0.48	0.53	0.56	0.45
Zn-65	243.90	1115.55	50.60	0.52	0.52	0.60	0.56	0.54	0.49	0.56	0.54
As-74	17.78	595.85	59.00	0.70	0.83	*1.48*	*2.20*	1.06	1.33	*1.57*	1.05
Se-75	119.78	264.66	58.90	0.92	1.03	1.07	1.10	0.92	0.99	1.02	1.17
		400.66	11.50	1.19	1.24	1.26	1.44		1.32	1.13	
Rb-83	86.20	520.39	44.70	1.93	1.93	1.89	1.92	*2.12*	1.94	2.03	2.69
		529.64	29.30	3.00	3.08	3.46	3.99	2.73	2.94	3.41	
Sr-85	64.84	514.01	96.00								2.04
Y-88	106.60	898.04	93.70	1.70	1.99	2.22	2.27	1.66	1.97	2.24	2.01
Nb-95	34.98	765.79	100.00	1.39	1.69	2.17	2.69	1.30	1.63	2.08	1.74

(Table 27: Au, 800 MeV continued)

				cumulative production cross sections (mb)							
				Au5 (25.5% uncertainty)				Au7 (6.2% uncertainty)			average
				without plates						with plates	of Au6,
	t_h	E_γ	branch ratio								
	(d)	(keV)	(%)	63 d	84 d	120 d	151 d	52 d	81 d	115 d	Au5, & Au7
Rh-102	207.00	556.41	96.00			0.17		*1.19*			0.16
I-126	13.11	388.63	34.10	3.26		*0.00*	*0.00*			*0.00*	3.26
		753.82	4.16			*0.00*	*0.00*			*0.00*	
Ba-131	11.80	496.33	47.00	*5.58*	*14.5*	*69.1*	*0.00*	3.87	*13.5*	*53.6*	3.18
Ba-133	3837.28	302.85	18.30								58.9
		356.02	62.00	58.9							
		383.85	8.94								
Ce-139	137.64	165.85	79.90		0.41	0.50	0.55		0.36	0.46	0.40
Eu-145	5.93	653.51	15.00	*0.00*	*0.00*	*0.00*	*0.00*	*0.00*	*0.00*	*0.00*	1.17
Eu-147	23.96	601.45	5.88	1.02	1.86	*7.73*	*14.6*	2.68	3.95	*6.24*	2.86
		677.52	9.80	2.70	2.73	*3.71*	*5.64*	2.34	2.58	*3.55*	
Eu-148	54.51	414.04	20.50								1.50
		571.96	9.56		1.55	1.42					
		725.67	12.70								
		869.89	5.49				0.26				
		1033.99	7.77								
Eu-149	93.06	327.53	4.03	6.55	8.49	8.36	8.31	3.66	7.11	7.95	7.29

(Table 27: Au, 800 MeV continued)

				cumulative production cross sections (mb)							
				Au5 (25.5% uncertainty)				Au7 (6.2% uncertainty)			average
			branch	without plates						with plates	of Au6,
	t_h	E_γ	ratio								
	(d)	(keV)	(%)	63 d	84 d	120 d	151 d	52 d	81 d	115 d	Au5, & Au7
Gd-149	9.38	149.74	48.20	*4.35*	*7.21*	*38.9*	*0.00*	*4.06*	*2.41*	*25.1*	3.31
		298.63	28.60	*0.00*	*0.00*	*0.00*	*0.00*	*3.74*	*0.00*	*469*	
		788.88	7.34	*0.00*	*101*	*0.00*	*0.00*		*89.9*	*67.6*	
Gd-151	123.96	174.70	2.96								2.31
Tm-168	93.10	184.24	17.50								0.51
		447.51	23.00	0.37	0.03	0.11		0.40			
		631.70	8.91								
		720.39	12.00								
		730.66	5.07								
		815.99	49.00	0.23	0.27	0.31	0.37	0.21	0.22	0.28	
		821.16	11.50		0.18						
		829.96	6.72	*8.65*	2.42			*14.5*	2.37	0.43	
Yb-169	32.01	130.52	11.30	33.1	36.7	37.5	39.9	30.4	35.1	35.5	34.0
		177.21	22.20	27.9	34.3	34.7	35.3	28.0	34.2	33.8	
Lu-171	8.24	739.78	47.80	*44.8*	*48.9*	*0.00*	*0.00*	*39.2*	*48.8*	*0.00*	38.5
Lu-173	500.03	171.40	18.50	41.1	49.7	43.3	41.2	46.1	37.1	44.0	41.0
		272.00	21.20	38.0	39.9	39.7	39.6	37.5	39.1	38.1	
Hf-172	682.87	125.82	11.30	*26.4*	*37.3*	*36.1*	*35.6*	*30.8*	*35.7*	*33.8*	36.2
Hf-175	70.00	343.40	84.00	37.0	42.3	43.8	43.5	35.8	40.9	43.2	42.0

(Table 27: Au, 800 MeV continued)

				cumulative production cross sections (mb)							
				Au5 (25.5% uncertainty)				Au7 (6.2% uncertainty)			average
				without plates						with plates	of Au6,
	t_h	E_γ	branch ratio	63 d	84 d	120 d	151 d	52 d	81 d	115 d	Au5, & Au7
	(d)	(keV)	(%)								
Hf-181	42.40	133.02	43.30								0.20
		482.18	80.50	0.13	0.17	0.14	0.12	0.06	0.14	0.25	
Ta-182	115.00	222.11	7.49	0.81	0.30			1.19	0.26		0.66
		1189.05	16.20				0.07			0.08	
		1221.41	27.00		0.04						
		1231.02	11.40								
Re-183	70.02	162.33	23.30	41.8	51.3		50.3	42.8	49.3	48.7	48.4
Re-184	37.96	792.07	37.50	0.68	0.77	1.06	1.48	0.65	0.76	0.97	0.94
		894.76	15.60			1.14	0.88			1.19	
		903.28	37.90								
Os-185	93.63	646.12	78.00	44.2	46.1	47.1	41.1	41.9	45.5	46.8	47.2
		874.81	6.29	46.4	47.8	46.7	46.6	45.4	47.4	46.3	
		880.52	5.17	*67.5*	*62.8*	*53.1*	*54.2*	*70.0*	*63.6*	*52.0*	
Ir-190	11.78	361.14	13.00	*3.33*	*3.20*	*22.8*	*0.00*	2.76	*3.47*	*0.00*	4.03
		371.26	23.00	*7.14*	*11.8*	*67.2*	*0.00*	4.88	*11.8*	*48.6*	
		397.39	6.54	*5.91*	*8.70*	*31.0*	*0.00*	4.19	*10.2*	*87.4*	
		407.24	28.50	*3.68*	*3.98*	*39.5*	*0.00*	3.43	*3.73*	*34.8*	
		518.55	34.00	*8.03*	*24.05*	*155*	*0.00*	5.44	*22.0*	*126*	
		569.31	28.50	*3.54*	*2.78*	*26.6*	*0.00*	3.29	*2.62*	*5.93*	

(Table 27: Au, 800 MeV continued)

				cumulative production cross sections (mb)							
				Au5 (25.5% uncertainty)				Au7 (6.2% uncertainty)			average
				without plates						with plates	of Au6,
	t_h	E_γ	branch ratio								
	(d)	(keV)	(%)	63 d	84 d	120 d	151 d	52 d	81 d	115 d	Au5, & Au7
Ir-192	73.83	295.96	28.70	1.65	2.21	2.30	2.33	*10.1*	1.97	2.20	2.26
		316.51	82.80	2.08	2.25	2.34	2.30	1.81	2.17	2.25	
		468.07	47.80	1.96	2.20	2.20	2.23	1.90	2.05	2.20	
		604.41	8.23	*6.06*	3.39	2.07	1.74	*9.82*	4.18	2.54	
Pt-188	10.19	195.05	18.60	*32.4*	*34.2*	*131*	*0.00*	*29.4*	*959*	*125*	32.1
		381.43	7.50	*29.4*	*32.8*	*0.00*	*0.00*	*27.1*	*41.4*	*59.7*	
Au-196	6.18	426.00	7.00	*0.00*	*604*	*0.00*	*0.00*	*62.6*	*480*	*0.00*	48.2

Summaries of all the radionuclide production cross section measurements with comparisons to previous measurements and theoretical predictions are found in Tables 28-33. Many of the radionuclides used to calculate inventory of the 1L target at LANSCE were measured and are in bold text in these tables. The theoretical predictions of CEM2k+GEM2 and Bertini are calculated by adding up all the independent cross sections to determine a cumulative cross section. The radionuclides used in determining the cumulative production cross section can be found in Appendix C. The only independent yields measured were from radionuclides that were "shadowed" from beta decay by stable isotopes or by isotopes such as ^{148}Gd that decay by alpha emission. The "shadowed" isotopes for which independent yields were measured are ^{144}Pm, ^{146}Pm, ^{148}Eu, ^{150}Eu, ^{152}Eu, ^{168}Tm, ^{174}Lu, and ^{184}Re.

Measurements from the Ta, W, and Au foils irradiated with 600- and 800-MeV protons compare well with the previous measurements. The theoretical predictions of CEM2k+GEM2 and Bertini compare better for the higher mass radionuclides than the lower mass radionuclides. Both models were a factor of two to four below the measurements, with CEM2k+GEM2 being slightly better than Bertini. At the higher masses, Bertini tended to compare better with the measurements, but both predictions were well within a factor of two of the measurements.

Table 28: Cumulative radionuclide production cross section measurements and comparisons to theoretical predictions and previous measurements for Ta2 at 600 MeV.

		cumulative production cross section (mb)				
		current	previous measurements		theoretical	
	t_h (d)	measurement 600 Mev	Asano [31] 500 MeV	Karamian [27] 660 MeV	CEM2k+GEM2	Bertini
Sc-46	83.79	0.163±0.018			0.078±0.011	0.034±0.009
V-48	15.97	0.025±0.004		0.023±0.002	0.009±0.004	0.016±0.006
Mn-54	312.30	0.154±0.017			0.118±0.013	0.036±0.010
Fe-59	44.50	0.033±0.007		0.180±0.013	0.124±0.014	0.068±0.013
Zn-65	243.90	0.367±0.050		0.300±0.021	0.178±0.016	0.078±0.014
As-74	17.78	0.332±0.066		0.320±0.022	0.276±0.020	0.070±0.014
Se-75	119.78	0.928±0.081		0.420±0.029	0.223±0.018	0.107±0.017
Rb-83	86.20	2.34±0.299	0.31±0.06	0.47±0.03	0.34±0.02	0.12±0.02
Zr-88	83.40	0.148±0.015		0.14±0.01	0.212±0.018	0.102±0.016
Nb-95	34.98	0.230±0.043		0.220±0.015	0.054±0.009	0.055±0.012
Rh-102	207.00	0.208±0.055		0.080±0.006	0.036±0.007	0.036±0.010
Xe-127	36.40	2.67±0.43			0.04±0.01	0.11±0.02
Ba-131	11.80	0.644±0.120		0.940±0.066	0.152±0.015	0.435±0.034
Ce-139	137.64	1.37±0.14	0.31±0.05	2.4±0.17	2.56±1.53	3.75±0.10
Pm-146	2017.14	1.00±0.16			0.01±0.00	0.08±0.01
Eu-145	**5.93**	**5.92±1.55**	**2±0.2**	**8.5±0.60**	**13.3±0.1**	**10.5±0.2**
Eu-147	**23.96**	**0.951±0.177**	**13±3**	**15±1.05**	**16.8±0.1**	**12.6±0.2**
Eu-148	54.51	0.933±0.096		0.73±0.05	0.30±0.02	1.60±0.06
Eu-149	93.06	20.6±2.4		28±1.96	21.3±0.2	15.6±0.2
Gd-149	**9.38**	**13.3±1.4**	**4.3±0.4**	**27±1.89**	**23.6±0.2**	**15.5±0.2**
Gd-151	123.96	13.8±2.6		19±1.33	21.1±0.2	17.9±0.2
Gd-153	**241.60**	**19.3±2.3**		**22±1.54**	**22.3±0.2**	**22.1±0.2**
Tm-167	**9.24**	**53.3±9.9**	**53±7**	**66±4.62**	**50.2±0.3**	**54.8±0.4**
Tm-168	93.10	1.30±0.07		1.3±0.09	1.50±0.05	1.23±0.06

(Table 28: Ta summary, 600 MeV continued)

		cumulative production cross section (mb)				
		current	previous measurements		theoretical	
	t_h	measurment	Asano [31]	Karamian [27]	CEM2k+GEM2	Bertini
	(d)	600 Mev	500 MeV	660 MeV		
Yb-169	**32.01**	**59.1±4.5**	**43±2**	**69±4.8**	**48.7±0.3**	**53.5±0.4**
Lu-171	**8.24**	**69.2±9.1**	**67±5**	**65±4.55**	**45.7±0.3**	**52.8±0.4**
Lu-173	**500.03**	**56.7±4.0**	**90±10**	**61±4.3**	**46.5±0.3**	**55.6±0.4**
Lu-174	1208.70	4.36±0.48	8		4.70±0.08	6.29±0.13
Hf-172	**682.87**	**39.7±10.4**	**29±5**	**47±3.29**	**39.6±0.2**	**41.3±0.3**
Hf-175	**70.00**	**51.7±5.2**	**54±4**	**56±3.9**	**44.1±0.3**	**46.4±0.4**
Hf-181	**42.40**	**0.216±0.031**		**0.14±0.01**	**0.000±0.000**	**0.057±0.012**
Ta-182	**115.00**	**0.372±0.036**			**0.000±0.000**	**0.000±0.000**

Table 29: Cumulative radionuclide production cross section measurements and comparisons to theoretical predictions and previous measurements for W at 600 MeV.

		cumulative production cross section (mb)			
		current	prev meas	theoretical	
	t_h (d)	measurement 600 Mev	Asano [31] 500 MeV	CEM2k+GEM2	Bertini
Sc-46	83.79	0.127±0.006		0.051±0.015	0.037±0.010
V-48	15.97	0.037±0.004		0.011±0.007	0.026±0.008
Mn-54	312.30	0.152±0.007		0.104±0.021	0.071±0.014
Fe-59	44.50	0.186±0.012		0.129±0.023	0.106±0.017
Zn-65	243.90	0.304±0.034		0.154±0.025	0.103±0.016
As-74	17.78	0.315±0.035		0.298±0.035	0.098±0.016
Se-75	119.78	1.66±0.06	0.20±0.06	0.225±0.030	0.140±0.019
Rb-83	86.20	0.373±0.019		0.307±0.035	0.216±0.024
Y-88	106.60	0.422±0.047		0.391±0.040	0.227±0.024
Zr-88	83.40	0.201±0.009	0.29±0.04	0.224±0.030	0.148±0.020
Nb-95	34.98	0.359±0.020		0.046±0.014	0.077±0.014
Rh-102	207.00	0.348±0.028		0.039±0.012	0.055±0.012
Xe-127	36.40	3.14±0.21		0.022±0.009	0.063±0.013
Ba-131	11.80	0.574±0.063		0.076±0.017	0.177±0.022
Ba-133	3837.28	3.39±0.37		0.129±0.022	0.375±0.031
Ce-139	137.64	0.746±0.031		1.20±0.07	2.12±0.07
Pm-144	363.43	0.031±0.003		0.057±0.015	0.343±0.030
Pm-146	2017.14	0.598±0.047		0.007±0.005	0.066±0.013
Eu-148	54.51	0.640±0.038		0.106±0.021	1.140±0.055
Eu-149	93.06	11.5±0.5		16.3±0.2	10.7±0.2
Gd-149	**9.38**	**9.04±1.38**	**2.8±0.4**	**16.2±0.2**	**10.7±0.2**
Gd-151	123.96	15.8±1.3		15.8±0.2	13.5±0.2
Gd-153	**241.60**	**12.4±1.3**		**17.2±0.2**	**16.2±0.2**
Tm-167	**9.24**	**50.1±13.2**		**49.1±0.5**	**50.0±0.4**
Tm-168	93.10	0.932±0.026		0.836±0.060	0.615±0.040
Yb-169	**32.01**	**59.4±2.2**	**40±6**	**50.9±0.5**	**52.3±0.4**
Lu-173	**499.69**	**57.8±4.2**	**90±10**	**49.2±0.5**	**59.6±0.4**
Lu-174	1208.70	1.62±0.09	43±4	2.19±0.10	2.70±0.08
Hf-172	**682.40**	**49.9±3.2**	**35±4**	**46.3±0.4**	**46.7±0.4**
Hf-175	**70.00**	**59.4±6.4**	**57±5**	**46.4±0.4**	**53.9±0.4**
Hf-181	**42.40**	**1.17±0.15**	**0.4±0.1**	**0.550±0.049**	**2.005±0.073**
Ta-182	**115.00**	**11.6±0.6**		**10.0±0.2**	**14.1±0.2**
Re-183	70.02	3.23±0.15	3.3±0.6	5.98±0.16	4.96±0.11
Re-184	**37.96**	**1.40±0.17**		**3.46±0.13**	**2.29±0.08**

Table 30: Cumulative radionuclide production cross section measurements and comparisons to theoretical predictions and previous measurements for Au2 at 600 MeV.

		cumulative production cross section (mb)					
		current	previous measurements			theoretical	
	t_h (d)	measurement 600 Mev	Asano [31] 500 MeV	Ross [32] 580 MeV	Michel [33] 600 MeV	CEM2k+GEM2	Bertini
Sc-46	83.79	0.0678±0.0081		0.075±0.019		0.0810±0.0114	0.0500±0.0118
Mn-54	312.30	0.219±0.029		0.181±0.075		0.224±0.019	0.117±0.018
Fe-59	44.50	0.382±0.072		0.375±0.088		0.257±0.035	0.222±0.025
Zn-65	243.90	0.361±0.043				0.534±0.029	0.178±0.022
As-74	17.78	0.842±0.166	0.63±0.06			1.10±0.04	0.197±0.023
Se-75	119.78	1.07±0.10	1.4±0.3			1.12±0.04	0.28±0.03
Rb-83	86.20	2.87±0.28	1.4±0.2	2.27±0.39		2.47±0.06	0.49±0.04
Sr-85	64.84	2.32±0.36				2.07±0.06	0.36±0.03
Y-88	106.60	1.76±0.24				2.94±0.07	0.65±0.04
Zr-88	83.40	0.557±0.061		0.584±0.248	0.61±0.05	1.49±0.05	0.397±0.033
Nb-95	34.98	1.85±0.29			1.36±0.11	0.93±0.04	0.34±0.03
Rh-102	207.00	0.155±0.020				0.787±0.035	0.172±0.022
Xe-127	36.40	2.21±0.33				0.09±0.01	0.13±0.02
Ba-131	11.80	3.11±0.58				0.03±0.01	0.09±0.02
Ba-133	3837.28	0.915±0.240				0.037±0.008	0.111±0.018
Eu-148	54.51	0.363±0.095				0.005±0.003	0.150±0.020
Eu-149	93.06	6.22±1.63				1.10±0.03	1.15±0.05
Eu-150	13459.63	3.23±0.60				0.00±0.00	0.03±0.01
Gd-149	9.38	1.82±0.48				1.10±0.03	1.05±0.05
Tm-168	93.10	1.31±0.13	0.5±0.1			0.02±0.01	0.07±0.01
Yb-169	32.01	24.67±2.66	8±1		20.7±0.9	28.26±0.21	26.42±0.27
Lu-171	8.24	39.8±7.4	19±1		27.3±1.2	32.8±0.2	31.0±0.3
Lu-173	500.03	35.1±2.8	30±5		65.6±2.4	38.2±0.2	38.2±0.3
Hf-172	682.87	32.8±6.1			24.2±1	38.5±0.3	31.4±0.3

(Table 30: Au summary, 600 MeV continued)

		cumulative production cross section (mb)					
		current	previous measurements			theoretical	
	t_h (d)	measurment 600 Mev	Asano [31] 500 MeV	Ross [32] 580 MeV	Michel [33] 600 MeV	CEM2k+GEM2	Bertini
Hf-175	70.00	43.1±4.6	30±2		42.6±2.5	41.8±0.3	41.4±0.3
Hf-181	42.40	0.398±0.077				0.005±0.003	0.000±0.000
Ta-182	115.00	0.397±0.065				0.030±0.007	0.019±0.007
Re-183	70.02	60.8±6.6	47±7			48.71±0.28	59.28±0.40
Re-184	37.96	0.959±0.146	47±8			1.14±0.04	0.84±0.05
Os-185	93.63	60.5±4.1	61±5		60.3±3	45.6±0.3	54.0±0.4
Ir-190	11.78	5.24±0.55	2.1±0.1			4.01±0.08	5.42±0.12
Ir-192	73.83	2.42±0.15	1.6±0.1			1.55±0.05	3.74±0.10
Pt-188	10.19	49.4±6.6	41±7			41.5±0.3	44.1±0.4
Au-195	186.09	61.7±6.7			69.4±3.1	37.1±0.2	41.5±0.3

Table 31: Cumulative radionuclide production cross section measurements and comparisons to theoretical predictionsfor Ta at 800 MeV.

	t_h (d)	cumulative production cross section (mb)		
		current measurement	theoretical	
			CEM2k+GEM2	Bertini
Sc-46	83.79	0.659±0.042	0.110±0.013	0.054±0.012
V-48	15.97	0.490±0.041	0.012±0.004	0.048±0.011
Mn-54	312.30	0.958±0.060	0.152±0.015	0.065±0.013
Fe-59	44.50	0.036±0.009	0.118±0.013	0.081±0.015
Zn-65	243.90	0.708±0.052	0.220±0.018	0.143±0.020
As-74	17.78	0.492±0.043	0.200±0.018	0.116±0.018
Se-75	119.78	0.776±0.058	0.254±0.020	0.140±0.020
Rb-83	86.20	1.92±0.14	0.365±0.024	0.197±0.023
Y-88	106.60	5.14±0.36	0.326±0.022	0.210±0.024
Zr-88	83.40	0.303±0.020	0.196±0.017	0.132±0.019
Nb-95	34.98	0.244±0.019	0.053±0.009	0.062±0.013
Rh-102	207.00	0.189±0.014	0.045±0.008	0.035±0.010
I-126	**13.11**	**55.6±14.2**	**0.002±0.002**	**0.075±0.014**
I-131	**8.02**	**10.4±2.6**	**0.000±0.000**	**0.000±0.000**
Xe-127	36.40	0.962±0.125	1.31±0.04	2.37±0.08
Ba-131	11.80	2.05±0.23	3.73±0.08	4.54±0.11
Ba-133	3837.28	2.15±0.20	5.68±0.09	5.73±0.12
Ce-139	137.64	6.89±0.49	11.9±0.1	14.6±0.2
Pm-144	363.43	0.275±0.028	0.258±0.020	1.21±0.06
Pm-146	2017.14	5.00±0.38	0.051±0.009	3.74±0.10
Eu-145	**5.93**	**25.9±6.6**	**28.1±0.2**	**20.2±0.2**
Eu-147	**23.96**	**27.3±1.4**	**30.0±0.2**	**22.5±0.2**
Eu-148	54.51	1.44±0.06	0.645±0.032	2.60±0.08
Eu-149	93.06	35.0±2.4	32.3±0.2	23.2±0.2
Gd-149	**9.38**	**50.3±7.9**	**35.8±0.2**	**23.0±0.2**
Gd-151	123.96	21.1±2.3	28.8±0.2	22.9±0.2
Gd-153	**241.60**	**29.7±2.0**	**26.5±0.2**	**27.3±0.3**
Tm-168	93.10	1.75±0.06	1.30±0.04	1.28±0.06
Yb-169	**32.01**	**55.8±2.3**	**37.4±0.2**	**40.6±0.3**
Lu-173	**500.03**	**53.4±2.6**	**36.8±0.7**	**41.8±0.3**
Lu-174	1208.70	4.60±0.49	3.97±0.08	5.72±0.12
Hf-172	**682.87**	**33.9±5.0**	**29.4±0.2**	**29.5±0.3**
Hf-175	**70.00**	**45.8±3.1**	**36.9±0.2**	**36.0±0.3**
Hf-181	**42.40**	**0.178±0.010**	**0.00±0.00**	**0.137±0.019**
Ta-182	**115.00**	**0.403±0.025**	**0.00±0.00**	**0.00±0.00**

Table 32: Cumulative radionuclide production cross section measurements and comparisons to theoretical predictions and previous measurements for W at 800 MeV.

		cumulative production cross section (mb)				
	t_h	current	previous 800 MeV measurements		theoretical	
	(d)	measurement	Titeranko [24]	Henry [23]	CEM2k+GEM2	Bertini
Sc-46	83.79	0.461±0.021		0.2±0.1	0.111±0.022	0.084±0.015
V-48	15.97	0.272±0.024		0.03±0.01	0.016±0.008	0.041±0.011
Mn-54	312.30	0.391±0.010		0.2±0.0	0.140±0.024	0.079±0.015
Fe-59	44.50	0.209±0.009		0.2±0.0	0.125±0.023	0.139±0.019
Zn-65	243.90	0.593±0.022			0.290±0.034	0.183±0.022
Se-75	119.78	1.28±0.04			0.273±0.034	0.302±0.029
Rb-83	86.20	2.17±0.09		0.7±0.1	0.426±0.042	0.518±0.038
Y-88	106.60	2.70±0.23		0.4±0.0	0.376±0.039	0.343±0.031
Zr-88	83.40	0.351±0.014		0.29±0.02	0.268±0.033	0.218±0.024
Nb-95	34.98	0.277±0.016			0.058±0.016	0.131±0.019
Rh-102	207.00	0.145±0.006			0.121±0.023	0.071±0.014
I-126	**13.11**	**0.599±0.063**			**0.000±0.000**	**0.035±0.010**
Ba-131	11.80	1.83±0.12			2.10±0.09	3.00±0.09
Ba-133	3837.28	2.06±0.06			3.53±0.12	4.16±0.11
Ce-139	137.64	3.97±0.16	4.85±0.21	4.0±0.1	8.66±0.19	10.47±0.17
Pm-144	363.43	0.153±0.007		0.2±0.02	0.20±0.03	0.956±0.051
Eu-145	**5.93**	**11.1±0.7**	**11.39±0.46**		**23.9±0.3**	**16.8±0.2**
Eu-147	**23.96**	**19.5±0.6**	**18.44±0.82**	**18.8±1.0**	**26.2±0.3**	**18.9±0.2**
Eu-148	54.51	0.939±0.022		0.71±0.03	0.387±0.040	2.28±0.08
Eu-149	93.06	23.9±0.6		22.5±0.7	29.4±0.3	20.2±0.2
Gd-149	**9.38**	**19.8±0.5**	**21.72±0.98**		**29.1±0.3**	**19.9±0.2**
Gd-151	123.96	14.1±1.1		15.4±1.1	25.7±0.3	21.1±0.2
Gd-153	**241.60**	**22.9±0.9**	**25.34±1.23**		**24.7±0.3**	**24.1±0.3**
Tm-168	93.10	0.791±0.016		0.77±0.04	0.650±0.053	0.654±0.042
Yb-169	**32.01**	**53.2±1.5**	**59.89±2.25**	**57.1±1.7**	**38.5±0.4**	**40.5±0.3**

(Table 32: W summary, 800 MeV continued)

	t_h	cumulative production cross section (mb)				
		current	previous 800 MeV measurements		theoretical	
	(d)	measurement	Titeranko [24]	Henry [23]	CEM2k+GEM2	Bertini
Lu-171	**8.24**	**60.0±3.7**	**59.70±2.12**		**37.3±0.4**	**41.7±0.3**
Lu-173	**499.69**	**52.3±1.5**	**61.66±3.09**	**55.3±2.4**	**37.9±0.4**	**44.7±0.4**
Lu-174	1208.70	1.94±0.12		0.36±0.05	2.09±0.09	2.58±0.08
Hf-172	**682.40**	**41.1±2.9**	**48.91±2.80**	**43.9±2.2**	**34.5±0.4**	**34.1±0.3**
Hf-175	**70.00**	**49.3±1.4**	**56.04±2.13**	**53.2±2.1**	**35.2±0.4**	**39.9±0.3**
Hf-181	**42.40**	**1.11±0.04**		**1.4±0.0**	**0.434±0.044**	**2.18±0.08**
Ta-182	**115.00**	**12.2±0.2**	**16.95±0.85**	**13.0±0.4**	**8.07±0.19**	**14.9±0.2**
Re-183	70.02	1.86±0.09		3.6±0.1	3.42±0.12	3.54±0.10
Re-184	**37.96**	**1.34±0.05**		**1.5±0.1**	**2.07±0.10**	**1.50±0.06**

Table 33: Cumulative radionuclide production cross section measurements and comparisons to theoretical predictions and previous measurements for Au at 800 MeV.

		cumulative production cross section (mb)					
	t_h	current	previous 800 MeV measurements			theoretical	
	(d)	measurement	GSI [28, 29]	ITEP [34]	Michel [30]	CEM2k+GEM2	Bertini
Sc-46	83.79	0.137±0.016	0.225±0.032		0.166±0.016	0.192±0.018	0.166±0.022
V-48	15.97	0.030±0.006	0.029±0.011			0.083±0.012	0.140±0.020
Mn-54	312.30	0.298±0.034	0.312±0.051		0.390±0.045	0.432±0.027	0.290±0.029
Fe-59	44.50	0.450±0.029	0.476±0.035		0.563±0.05	0.252±0.023	0.310±0.030
					0.5±0.03		
Zn-65	243.90	0.541±0.035	0.466±0.024		0.554±0.160	0.958±0.040	0.427±0.035
As-74	17.78	1.05±0.09	1.101±0.111	1.42±0.11	1.37±0.111	1.20±0.04	0.48±0.04
Se-75	119.78	1.17±0.06	0.909±0.033		1.16±0.089	1.50±0.05	0.55±0.04
					0.97±0.07		
Rb-83	86.20	2.69±0.14	1.806±0.122	2.67±0.24	1.99±0.14	2.69±0.07	0.91±0.05
					2.32±0.32		
Sr-85	64.84	2.04±0.26	1.317±0.121	2.34±0.16	1.94±0.148	2.29±0.06	0.79±0.05
					1.77±0.14		
Y-88	106.60	2.01±0.13	2.117±0.179	2.82±0.200	2.45±0.192	3.05±0.07	1.15±0.06
					2.23±0.16		
Nb-95	34.98	1.74±0.12	1.115±0.078	2.03±0.13	1.65±0.13	0.614±0.032	0.467±0.037
					1.25±0.15		
Rh-102	207.00	0.162±0.029	0.541±0.107			0.631±0.032	0.353±0.032
I-126	13.11	3.26±0.83				0.003±0.002	0.049±0.012
Ba-131	11.80	3.18±0.36				0.106±0.013	0.421±0.035
Ba-133	3837.28	58.9±15.0				0.165±0.016	0.613±0.042
Ce-139	137.64	0.396±0.032		0.757±0.05	0.569±0.04	0.721±0.035	2.17±0.08
Eu-145	5.93	1.17±0.30	2.761±0.155	1.69±0.16	1.42±0.15	4.82±0.07	5.02±0.11
					1.21±0.10		
Eu-147	23.96	2.86±0.17	4.655±0.260	3.08±0.30	2.66±0.25	6.37±0.09	6.24±0.13

(Table 33: Au summary, 800 MeV continued)

		cumulative production cross section (mb)					
	t_h	current	previous 800 MeV measurements			theoretical	
	(d)	measurement	GSI [28, 29]	ITEP [34]	Michel [30]	CEM2k+GEM2	Bertini
Eu-148	54.51	1.50±0.16	0.080±0.010		0.149±0.0141	0.046±0.009	0.914±0.051
Eu-149	93.06	7.29±0.50	3.521±0.167		72.2±6.24	9.19±0.10	7.08±0.13
Gd-149	9.38	3.31±0.50	6.898±0.349	3.91±0.30	4.49±0.34	9.17±0.10	6.43±0.13
					2.76±0.25		
Gd-151	123.96	2.31±0.59	3.310±0.190			9.11±0.11	8.59±0.15
Tm-168	93.10	0.510±0.038	0.040±0.005		0.283±0.0472	0.041±0.008	0.083±0.015
Yb-169	32.01	34.0±1.7	34.42±1.92	39.4±2.40		34.1±0.2	31.3±0.3
Lu-171	8.24	38.5±9.8	37.79±2.14	48.1±2.90		35.1±0.2	33.7±0.3
Lu-173	500.03	41.0±1.9	43.45±2.04	47.60±3.10	62.4±5.13	37.1±0.3	38.2±1.3
					73.6±5.3		
Hf-172	682.87	36.2±6.5	40.75±2.20	44.60±2.80		39.4±0.3	31.6±0.3
Hf-175	70.00	42.0±2.7	45.65±2.45	52.90±3.50	49.6±3.76	38.2±0.3	38.3±0.3
					42±3		
Hf-181	42.40	0.199±0.020				0.00±0.00	0.00±0.00
Ta-182	115.00	0.665±0.067	0.010±0.008			0.026±0.007	0.023±0.008
Re-183	70.02	48.4±3.2	51.97±2.95	62.9±4.1	49.7±4.27	38.2±0.3	45.4±0.4
Re-184	37.96	0.944±0.063	1.18±0.15			1.01±0.04	0.883±0.050
Os-185	93.63	47.2±2.1	30.10±1.88	60.5±3.8	63.3±4.76	35.8±0.2	40.5±0.3
					53.7±3.8		
Ir-190	11.78	4.03±0.21	6.02±0.77	4.36±0.27		3.45±0.07	5.01±0.12
			4.67±0.40				
Ir-192	73.83	2.26±0.08	4.18±0.54	2.76±0.17	2.91±0.23	1.42±0.05	3.67±0.10
			2.91±0.23				
Pt-188	10.19	32.1±4.1	39.66±2.48	48.0±3.0	46±3.70	31.2±0.2	31.6±0.3
Au-196	6.18	48.2±12.3	57.98±5.46	82.8±5.0	66±7.04	39.4±0.3	74.6±0.5
			66±7				

CHAPTER VI

DISCUSSION AND CONCLUSION

"The only relevant thing is uncertainty-the extent of our knowledge and ignorance. The actual fact of whether the events considered are in some sense determined, or known by other people is of no consequence." Kristian Zarb Adami

Two tungsten targets at LANSCE's accelerator complex interact with 800-MeV protons to produce high- and low-energy neutrons. These targets also produce hundreds of different nuclides ranging from the atomic number of hydrogen to nuclides with atomic number justs above that of the target. These radionuclide products are distributed somewhat heterogeneously throughout the thick target because of the energy dependence of the cross sections and energy loss of the proton beam within the target. The U. S. Department of Energy requires hazard classification analyses to be performed on these facilities and limits the radionuclide inventories in the targets to avoid characterizing the facilities as "nuclear facilities." Gadolinium-148 is one radionuclide produced from the spallation of tungsten. Allowed isotopic inventories are particularly low for this isotope because it is an alpha-particle emitter with a 75-year half-life. It's activity level is low, but encompasses almost two-thirds of the total dose burden for the two tungsten targets based on present yield estimates. From a hazard classification standpoint, this severely limits the lifetime of the tungsten targets.

The ^{148}Gd production cross section has not been well measured for tungsten within the energy range of the upper Lujan target, 600 to 800 MeV. A series of experiments at LANSCE's WNR Blue Room facility irradiated 3-μm thin W, Ta, and Au foils with 600- and 800-MeV protons to measure the ^{148}Gd production cross section, and other radionuclides of interest to the spallation target community. The foils were sufficiently thin so that no secondary spallation reactions would likely occur, yielding a discrete energy dependent production cross section. The foils also had to be thin enough to allow ^{148}Gd decay alphas

to later escape and be detected. The proton flux was measured during the irradiation with current monitors upstream of the Blue Room, and with aluminum activation foils irradiated with the stack of W, Ta, and Au foils to produce ^{22}Na. The proton flux from the current monitors agreed within 10% of the ^{22}Na activation measurements.

The 600-MeV irradiation consisted of W, Ta, Au, and Al foils in stacks of three, where the middle foil accounted for recoil gains and losses from the surrounding foils of the same material. The 800-MeV experiments used this stacked foil method for one irradiation each of W, Ta, and Au. In addition, another 800-MeV irradiation used single foils of W, Ta, and Au, surrounded by aluminum catcher foils to determine what percentage of the ^{148}Gd recoiled onto the surrounding foils and compare methods for measuring the cross section.

The ^{148}Gd production cross sections were measured by charged particle spectroscopy, while all other radionuclide yields were measured with γ-ray spectroscopy. All of the cross sections measured from the stacked and single foils agreed well within the uncertainty of the measurements. A summary of the ^{148}Gd measurements and predictions can be found in Table 34. The ^{148}Gd recoils were $\sim$10% of the total ^{148}Gd measured, with the majority of the recoils scattered forward.

The ^{148}Gd production cross section measurements at 800-MeV for W and Au were within 20% of the previous measurements, which used radiochemical analysis and inverse kinematics via a fragment separator. This lends credibility to the charged particle thin foil method used here. The theoretical predictions by CEM2k+GEM2 were within a factor of two of the measurements, with Bertini giving better agreement to the measurement. This is partly due to the large contribution from ^{152}Er in CEM2k+GEM2 versus Bertini. The physics models are so different, a particular part of the codes cannot be pinpointed as the root of this difference.

Other radionuclide production cross sections compared well with previous measurements for low, medium, and high mass nuclide products. Like the ^{148}Gd comparison, the theoretical predictions were within a factor of two of the other radionuclide production measurements. The worst agreements were for those products that had a low Z and mass

Table 34: Summary of cumulative ^{148}Gd production cross section measurements and comparisons to theoretical predictions and previous measurements

		^{148}Gd cumulative production cross section (mb)			
	Energy	Current	Previous	Theoretical	
Target	(MeV)	Measurement	Measurement	CEM2k+GEM2	Bertini
Ta	600	15.2±4.0		29.4±0.2	15.5±0.2
	800	28.6±3.5		45.6±0.3	24.4±0.3
W	600	8.31±0.92		21.6±0.3	10.9±0.2
	800	19.4±1.8	16.4±0.8	41.4±0.4	20.9±1.6
Au	600	0.591±0.155		1.41±0.04	0.929±0.049
	800	3.69±0.50	3.74±0.19	12.9±0.1	7.23±0.14

significantly lower than the target mass. In this region, Bertini and CEM2k+GEM2 typically underpredicted by a factor of two to three. In the region of higher mass radionuclide products, the codes tended to slightly overpredict the cross section, but agreed well within a factor of two of the cumulative measurements.

The absolute uncertainties in the cross section measurements are difficult to quantify but the reproducibility of the cross sections at 800 MeV over several experiments with different methods lends confidence that the cross sections measured are valuable to the spallation target community. However, more measurements over broader energy ranges are needed with isotopically pure tungsten foils, and the ability to measure shorter-lived (<3 d half-life) radionuclides that feed into the ^{148}Gd cumulative production cross section.

The fifteen radionuclides analyzed for the Lujan 1L tungsten target hazard classification agreed well within a factor of two of previous measurements and theoretical predictions, lending some confidence in the codes' abilities to predict radionuclide production for spallation targets within 600 to 800 MeV. Bertini compared much better than CEM2k+GEM2 with the radionuclides of interest that were measured. Bertini's predictions were higher than the measurements for the radionuclides listed in Table 1 that are most limited by the amount of curies that can be produced. Bertini's predictions were then slightly lower than the measurements for radionuclides in Table 1 least limited by the amount of curies that can be produced. Bertini overpredicted the most limiting cases, where the curie limits are

several orders of magnitude less than the other radionuclides (Tables 1 and 2). Therefore, it is the recommendation of this work that Bertini be used to calculate the radionuclide inventory for the spallation targets at LANSCE. Furthermore, the factor of 1.5 that has been applied to the cumulative inventory to account for uncertainties in the predictions and for radionuclides without dose conversion factors should be reduced to 1.0 for the radionuclide measurements presented in this work. For all other radionuclides of interest that were not measured, the factor 1.5 should remain the same. As a result, the anticipated cumulative dose at 960 m should decrease by 30% and therefore the tungsten targets at LANSCE would have an extended lifetime of 30%.

APPENDIX A

DECAY FEEDING ^{148}GD SCHEMES

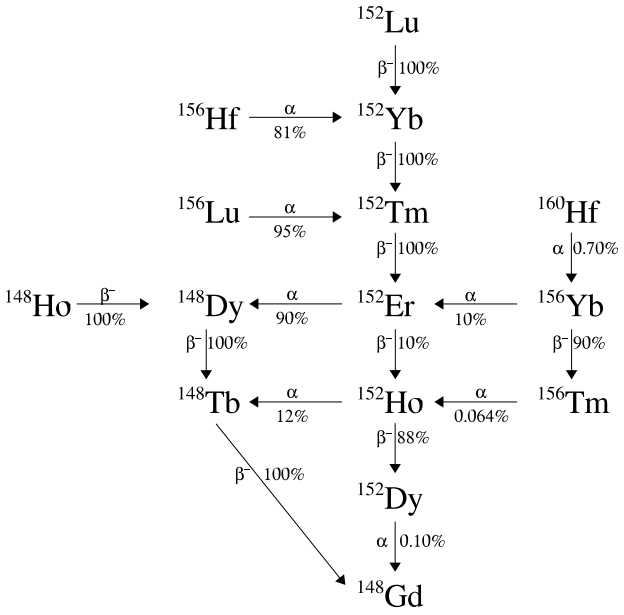

Figure A.1: Decay diagram feeding ^{148}Gd

Table A.1: Half-lifes of ^{148}Gd decay feeding diagram radionuclides

radionuclide	half-life	radionuclide	half-life
^{160}Hf	13.6 s	^{152}Er	10.3 s
^{156}Hf	25 ms	^{152}Ho	161.8 s
^{156}Lu	494 ms	^{148}Ho	2.2 s
^{152}Lu	0.7 s	^{152}Dy	2.38 h
^{156}Yb	26.1 s	^{148}Dy	3.1 m
^{152}Yb	3.04 s	^{148}Tb	60 m
^{156}Tm	83.8 s	^{148}Gd	74.6 y
^{152}Tm	8.0 s		

APPENDIX B

RADIONUCLIDE LIBRARY

Table B.1: Radionuclide library used in PCGAP with lists of contaminants and their half-lifes for each energy. Half-lifes, emitting energies, and branching ratios were obtained from [53].

Isotope	half-life	E_γ (keV)	branching ratio (%)	contaminants
4 Be 7	53.1 d	477.60	10.52	
11 Na 22	2.6 y	1274.53	99.94	
21 Sc 46	83.8 d	889.28	99.98	Lu-171 (8.3 d)
		1120.55	99.99	Ta-182 (115 d), Re-182 (2.7 d)
23 V 48	16.0 d	944.10	7.76	
		983.52	99.98	Lu-170 (2 d)
		1312.10	97.50	
25 Mn 54	312.3 d	834.85	99.98	Lu-172 (6.7 d)
26 Fe 59	44.5 d	1099.25	56.50	
27 Co 57	271.8 d	14.41	9.16	
		122.06	85.60	
		136.47	10.68	
27 Co 58	70.9 d	810.78	99.00	Lu-172 (6.7 d)
27 Co 60	5.3 y	1173.24	99.97	
		1332.50	99.99	
30 Zn 65	243.9 d	1115.55	50.60	Lu-172 (6.7 d)
33 As 73	80.3 d	53.44	10.34	
33 As 74	17.8 d	595.85	59.00	
		634.78	15.40	Eu-146 (4.6 d), Ge-77 (11.3 h)
33 As 76	1.1 d	559.10	45.00	
		657.04	6.20	
34 Se 75	119.8 d	121.12	17.20	Eu-152 (13.5 y), Co-57 (272 d)
		136.00	58.30	Hf-181 (42.4 d), Co-57 (272 d)
		264.66	58.90	Gd-149 (9.3 d), Lu-172 (6.7 d)
		279.54	24.99	Eu-149 (93.1 d), Re-182 (2.7 d)

(Table B.1 continued)

Isotope	half-life	E_γ (keV)	branching ratio (%)	contaminants
34 Se 75	119.8 d	400.66	11.47	Lu-172 (6.7 d)
35 Br 77	2.4 d	239.00	23.00	
		520.64	22.40	
36 Kr 79	1.5 d	261.35	13.00	
		397.54	9.30	
		606.09	8.12	
37 Rb 83	86.2 d	520.39	44.70	Ir-190 (11.8 d), Br-77 (2.4 d)
		529.64	29.30	
		552.63	16.00	Eu-148 (54.5 d)
38 Sr 83	1.4 d	381.53	14.10	
		762.65	30.00	
38 Sr 85	64.8 d	514.01	96.00	
39 Y 87	3.3 d	388.53	82.00	
		484.81	89.70	
39 Y 88	106.6 d	898.04	93.70	
		1836.06	99.20	
40 Zr 88	83.4 d	392.87	100.00	
41 Nb 95	35.0 d	765.79	100.00	
45 Rh 101	3.3 y	127.23	68.00	Hf-172 (1.9 y)
		197.99	73.00	
		325.23	11.83	
45 Rh 102	207.0 d	475.10	38.40	Pm-144 (363 d)
		556.41	96.00	Ir-190 (11.8 d)
45 Rh 105	1.5 d	306.25	5.10	
		319.14	19.00	
49 In 111	2.8 d	171.28	90.00	
		245.40	94.00	
50 Sn 113	115.1 d	391.69	64.00	
51 Sb 122	2.7 d	564.12	71.00	
53 I 124	4.2 d	602.73	63.00	
		722.79	10.35	Tm-168 (93.1 d), Eu-148 (54.5 d)
		1690.98	10.88	

(Table B.1 continued)

Isotope	half-life	E_γ (keV)	branching ratio (%)	contaminants
53 I 125	60.1 d	35.49	6.68	
53 I 126	13.1 d	388.63	34.10	Y-87 (3.3 d)
		666.33	33.10	Lu-171 (8.2 d), Eu-146 (4.6 d)
		753.82	4.16	
53 I 131	8.0 d	284.31	6.14	Re-182 (2.7 d)
		364.49	81.70	
		636.99	7.17	
54 Xe 127	36.4 d	124.60	69.00	Ba-131 (11.8 d), Hf-172 (1.9 y)
		172.50	37.90	Lu-173 (1.4 y), Gd-151 (124 d)
		172.13	25.50	Lu-173 (1.4 y), Gd-151 (124 d)
		202.86	68.30	Lu-172 (6.7 d)
		374.99	17.20	Ba-131 (11.8 d)
55 Cs 129	1.3 d	371.92	30.60	
		411.49	22.31	
56 Ba 131	11.8 d	123.81	28.97	Xe-127 (36.4 d)
		216.08	19.66	Re-184m (165 d)
		373.25	14.04	Xe-127 (36.4 d)
		496.33	47.00	
56 Ba 133	10.5 y	80.99	34.10	
		276.40	7.16	Eu-149 (93 d), Re-182 (2.7 d)
		302.85	18.33	
		356.02	62.05	Ta-183 (5.1 d), Au-196 (6.2 d)
		383.85	8.94	
58 Ce 139	137.6 d	165.85	79.90	
60 Nd 140	3.4 d	35.55	21.00	
		36.03	38.30	
		40.75	7.08	
61 Pm 143	265.0 d	741.98	38.50	
61 Pm 144	363.4 d	476.78	42.00	Be-7 (53.1 d), Rh-102 (207 d)
		618.01	98.60	Ag-106m (8.3 d)
		696.49	99.50	Lu-172 (6.7 d)
61 Pm 145	17.7 y	67.20	0.55	
		72.40	1.85	
61 Pm 146	5.5 y	453.88	65.00	Eu-145 (5.9 d), Hf-179m2 (25 d)
		735.72	22.50	Eu-150 (36.9 y)
		747.16	34.00	Eu-146 (4.6 d), Eu-150 (36.9 y), Gd-149 (9.4 d)

(Table B.1 continued)

Isotope	half-life	E_γ (keV)	branching ratio (%)	contaminants
62 Sm 145	340.0 d	61.22	12.20	
63 Eu 145	5.9 d	653.51	15.00	
		893.73	66.00	Gd-147 (1.6 d), Re-184 (38.0 d)
		1658.53	14.90	
		1997.00	7.20	
63 Eu 146	4.6 d	633.08	35.90	As-74 (17.8 d), Ir-188 (1.7 d)
		634.14	45.00	As-74 (17.8 d), Ir-188 (1.7 d)
		665.42	7.23	I-126 (13.1 d), Lu-171 (8.2 d)
		747.16	98.50	Pm-146 (5.5 y), Eu-150 (36.9 y)
		1297.03	5.39	
		1533.71	6.08	
63 Eu 147	24.0 d	121.22	22.90	Se-75 (120 d), Eu-152 (13.5 y)
		197.30	27.00	Yb-169 (32 d), Rh-101 (3.3 y)
		601.45	5.88	I-124 (4.2 d)
		677.52	9.80	
		1077.04	6.15	Re-182 (2.7 d)
63 Eu 148	54.5 d	414.03	10.33	
		414.06	10.15	
		550.23	98.60	Rb-83 (86.2 d)
		553.23	12.90	Rb-83 (86.2 d)
		553.26	5.00	Rb-83 (86.2 d)
		571.96	9.56	Ir-190 (11.8 d)
		611.25	20.10	Ir-192 (73.8 d)
		629.93	70.50	Tm-168 (93.1 d)
		725.67	12.73	
		869.89	5.49	
		1033.99	7.77	
63 Eu 149	93.1 d	22.51	2.40	
		277.09	3.55	Re-182 (2.7 d), Ba-133 (10.5 y), Se-75 (120 d)
		327.53	4.03	Rh-101 (3.3 y)
63 Eu 150	36.9 y	333.97	96.00	Au-196 (6.2 d)
		439.40	80.40	
		584.27	52.60	
		737.46	9.60	Pm-146 (5.5 y), Lu-171 (8.2 d)
		748.06	5.18	Pm-146 (5.5 y)
		1049.04	5.38	
63 Eu 152	13.5 y	121.78	28.58	Se-75 (120 d)
		244.70	7.58	Gd-151 (124 d), Ta-183 (5.1 d), Ir-189 (13.2 d), In-111 (2.8 d)
		344.28	26.50	
		778.90	12.94	

(Table B.1 continued)

Isotope	half-life	E_γ (keV)	branching ratio (%)	contaminants
63 Eu 152	13.5 y	964.08	14.61	
		1085.87	10.21	
		1112.07	13.64	
		1408.01	21.01	
64 Gd 146	48.3 d	114.71	44.00	Lu-177 (6.7 d), Re-184 (38.0 d)
		115.51	44.00	Lu-177 (6.7 d), Re-184 (38.0 d)
		154.57	46.60	Gd-151 (124 d), Ta-182 (115 d)
64 Gd 147	1.6 d	229.32	63.00	
		370.00	17.20	
		396.00	34.30	
		559.07	6.45	
		765.81	11.30	
		893.50	8.10	
		929.01	20.20	
		1069.35	7.20	
		1130.90	6.40	
64 Gd 149	9.4 d	149.74	48.20	
		298.63	28.60	
		346.65	23.90	Eu-152 (13.5 y), Hf-181 (42.4 d)
		748.60	8.22	Eu-150 (36.9 y)
		788.88	7.34	
64 Gd 151	124.0 d	153.60	6.20	Gd-146 (48 d), Ta-182 (115 d)
		174.70	2.96	Lu-172 (6.7 d)
		243.29	5.60	Ta-182 (115 d), Eu-152 (13.5 y)
64 Gd 153	241.6 d	69.67	2.32	
		97.43	27.60	Au-195 (186.1 d), Ta-183 (5.1 d)
		103.18	19.60	Re-184m (165 d)
65 Tb 153	2.3 d	82.84	5.90	
		102.26	6.40	
		109.76	6.76	
		170.45	6.30	
		212.00	31.00	
65 Tb 155	5.3 d	86.55	31.80	
		105.32	24.90	
		180.08	7.40	
		262.32	5.29	
65 Tb 157	150.1 y	54.50	0.01	
66 Dy 159	144.4 d	58.00	2.22	
69 Tm 165	1.3 d	47.16	16.90	

(Table B.1 continued)

Isotope	half-life	E_γ (keV)	branching ratio (%)	contaminants
69 Tm 165	1.3 d	54.42	7.21	
		242.92	35.50	
		297.37	12.71	
		806.37	9.50	
69 Tm 167	9.2 d	207.80	41.00	
69 Tm 168	93.1 d	79.80	10.53	
		184.24	17.45	Gd-149 (9.3 d)
		198.24	52.60	Yb-169 (32 d), Rh-101 (3.3 y)
		447.51	23.00	
		631.70	8.92	
		720.39	12.00	
		730.66	5.07	
		741.36	12.32	
		815.99	49.00	
		821.16	11.54	
		829.96	6.72	
70 Yb 166	2.4 d	82.29	100.00	
70 Yb 169	32.0 d	63.12	44.20	
		109.78	17.47	Re-184 (38 d)
		130.52	11.31	Rh-101 (3.3 y), Re-182 (2.7 d)
		177.21	22.16	Tb-155 (5.3 d)
		197.96	35.80	Rh-101 (3.3 y), Tm-168 (93.1 d)
		307.74	10.05	Ir-192 (73.8 d)
71 Lu 169	1.4 d	191.21	20.60	
		889.75	5.36	
		960.62	23.40	
		1149.74	9.92	
71 Lu 170	2.0 d	84.25	9.00	
		985.10	5.54	
		1280.25	8.18	
		2041.88	6.10	
		2126.11	5.13	
71 Lu 171	8.2 d	19.39	13.70	
		75.88	6.08	
		667.40	11.04	
		739.78	47.80	Eu-150 (36.9 y), Tm-168 (93.1 d)
71 Lu 172	6.7 d	52.39	49.50	
		78.74	10.60	
		181.53	20.60	
		203.44	5.02	
		697.30	6.13	

(Table B.1 continued)

Isotope	half-life	E_γ (keV)	branching ratio (%)	contaminants
71 Lu 172	6.7 d	810.06	16.63	
		900.72	29.80	
		912.13	15.25	
		1002.75	5.25	
		1093.66	62.50	
71 Lu 173	1.4 y	78.70	11.10	
		100.70	4.51	Ta-182 (115 d)
		171.40	18.50	
		272.00	21.23	
71 Lu 174	3.3 y	76.47	5.93	
		1241.85	5.14	
71 Lu 177	6.7 d	112.95	6.40	
		208.37	11.00	
71 Lu-m 174	142.0 d	44.68	12.40	
		67.06	7.25	
72 Hf 172	1.9 y	23.98	20.30	
		67.35	5.31	
		125.82	11.30	Xe-127 (36.4 d), Rh-101 (3.3 y)
72 Hf 173	1.0 d	123.67	83.00	
		139.63	12.70	
		162.01	6.46	
		296.97	33.90	
		306.57	6.42	
		311.24	10.75	
72 Hf 175	70.0 d	343.40	84.00	Eu-152 (13.5y)
72 Hf 181	42.4 d	133.02	43.30	Ba-131 (11.8 d)
		136.27	5.85	Co-57 (272 d)
		345.93	15.10	Hf-175 (70 d), Eu-152 (13.5 y), Gd-149 (9.4 d)
		482.18	80.50	Y-87 (3.3 d)
73 Ta 177	2.4 d	112.95	7.20	
73 Ta 182	115.0 d	67.75	41.20	
		100.11	14.10	Lu-173 (1.4 y)
		152.43	6.93	Gd-151 (124 d)
		222.11	7.50	Re-182 (2.7 d)
		1121.30	34.90	Sc-46 (83.8 d)
		1189.05	16.23	Re-182 (2.7 d)
		1221.41	27.00	Re-182 (2.7 d)
		1231.02	11.44	Re-182 (2.7 d)

(Table B.1 continued)

Isotope	half-life	E_γ (keV)	branching ratio (%)	contaminants
73 Ta 183	5.1 d	46.48	5.80	
		52.60	5.80	
		99.08	6.70	
		107.93	11.00	Tb-153 (2.3 d), Yb-169 (32 d)
		161.35	8.90	
		244.26	8.50	Eu-152 (13.5 y)
		246.06	27.00	
		353.99	11.20	
75 Re 182	2.7 d	67.75	22.20	
		100.11	16.40	
		130.80	7.50	
		152.43	8.50	
		156.39	7.20	
		169.15	11.30	
		191.38	6.70	
		221.59	6.40	
		222.11	8.50	
		229.32	26.00	
		247.44	5.00	
		256.45	9.50	
		276.31	8.70	
		281.46	5.70	
		286.55	7.00	
		339.06	5.60	
		351.07	10.30	
		1076.30	10.50	
		1121.30	22.00	
		1189.05	9.00	
		1221.41	17.40	
		1231.02	14.90	
		1427.37	9.79	
75 Re 183	70.0 d	46.48	7.97	
		162.33	23.30	Ta-183 (5.1 d)
75 Re 184	38.0 d	111.21	17.10	Yb-169 (32 d), Lu-177 (6.7 d), Ta-177 (2.4 d)
		792.07	37.50	
		894.76	15.63	
		903.28	37.90	Eu-145 (5.9 d)
75 Re 186	3.8 d	137.16	9.42	
75 Re-m 184	165.5 d	104.73	13.40	
		216.55	9.43	Ba-131 (11.8 d)
		252.84	10.70	
		920.93	8.14	

(Table B.1 continued)

Isotope	half-life	E_γ (keV)	branching ratio (%)	contaminants
76 Os 185	93.6 d	646.12	78.00	
		874.81	6.29	
		880.52	5.17	Re-184 (32.8 d)
77 Ir 188	1.7 d	155.03	29.70	
		477.99	15.00	
		632.99	18.00	
		634.98	5.00	
		829.49	5.14	
		1209.80	6.90	
		1715.67	6.20	
		2059.67	7.10	
		2096.90	5.70	
		2214.62	18.70	
77 Ir 189	13.2 d	245.09	6.00	Eu-152 (13.5 y)
77 Ir 190	11.8 d	186.72	52.40	Pt-188 (10.2 d)
		294.75	6.60	Ir-192 (73.8 d)
		361.14	13.00	Pt-191 (2.9 d)
		371.26	23.00	Ba-131 (11.8 d)
		397.39	6.54	
		407.18	23.90	Pt-191 (2.9 d)
		407.54	4.60	
		518.55	34.00	
		557.97	30.10	Rh-102 (207 d)
		569.31	28.50	Eu-148 (54.5 d)
		605.24	39.90	Ir-192 (73.8 d)
77 Ir 192	73.8 d	295.96	28.67	Ir-190 (11.7 d)
		308.46	30.00	Yb-169 (32 d)
		316.51	82.81	
		468.07	47.83	
		604.41	8.23	I-124 (4.2 d), Ir-190 (11.7 d)
		612.47	5.31	Eu-148 (54.5 d)
78 Pt 188	10.2 d	187.59	19.40	Ir-190 (11.8 d)
		195.05	18.60	
		381.43	7.50	Ba-133 (10.5 y)
78 Pt 191	2.9 d	359.90	6.00	
		409.44	8.00	
		538.90	13.70	
79 Au 194	1.6 d	293.55	10.40	
		328.46	61.00	
		1468.91	6.40	

(Table B.1 continued)

Isotope	half-life	E_γ (keV)	branching ratio (%)	contaminants
79 Au 195	186.1 d	98.85	10.90	
79 Au 196	6.2 d	332.98	22.90	Eu-150 (36.9 y)
		355.68	87.00	Ba-133 (10.5 y), Ta-183 (5.1 d)
		426.00	7.00	
80 Hg-m 195	1.7 d	37.09	1.84	
		261.75	30.90	
		387.87	2.15	
		560.27	4.00	
80 Hg 197	2.7 d	77.35	18.70	

APPENDIX C

CUMULATIVE PRODUCTION CROSS SECTIONS

Table C.1: Radionuclides used in calculating cumulative production cross sections

Cumulative Radionuclide	Sum of Independent Radionuclides and their contribution
^{46}Sc	^{46}Sc
^{48}V	^{48}V+^{48}Cr+^{48}Mn+^{48}Fe+^{48}Co
^{54}Mn	^{54}Mn
^{59}Fe	^{59}Fe+^{59}Mn+^{59}Cr
^{58}Co	^{58}Co
^{65}Zn	^{65}Zn+^{65}Ga+^{65}Ge+^{65}As+^{65}Se
^{74}As	^{74}As
^{75}Se	^{75}Se+^{75}Br+^{75}Kr+^{75}Rb+^{75}Sr
^{83}Rb	^{83}Rb+^{83}Sr+^{83}Y
^{88}Y	^{88}Y+^{88}Zr+^{88}Nb+^{88}Mo+^{88}Tc+^{88}Ru
^{88}Zr	^{88}Zr+^{88}Nb+^{88}Mo+^{88}Tc+^{88}Ru
^{95}Nb	^{95}Nb+^{95}Zr+^{95}Y+^{95}Sr+^{95}Rb+^{95}Kr+^{95}Br
^{101}Rh	^{101}Rh+^{101}Pd+^{101}Ag+^{101}Cd+^{101}In+^{101}Sn
^{102}Rh	^{102}Rh
^{124}I	^{124}I
^{126}I	^{126}I
^{131}I	^{131}I+^{131}Te+^{131}Sb+^{131}Sn+^{131}In

(Table C.1 continued)

Cumulative Radionuclide	Sum of Independent Radionuclides and their contribution
^{127}Xe	^{127}Xe+^{127}Cs+^{127}Ba+^{127}La+^{127}Ce+^{127}Pr
^{131}Ba	^{131}Ba+^{131}La+^{131}Ce+^{131}Pr+^{131}Nd+^{131}Pm+^{131}Sm
^{133}Ba	^{133}Ba+^{133}La+^{133}Ce+^{133}Pr+^{133}Nd+^{133}Pm+^{133}Sm
^{139}Ce	^{139}Ce+^{139}Pr+^{139}Nd+^{139}Pm+^{139}Sm+^{139}Eu+^{139}Gd
^{144}Pm	^{144}Pm
^{146}Pm	^{146}Pm
^{145}Eu	^{145}Eu+^{145}Gd+^{145}Tb+^{145}Dy+^{145}Ho+^{145}Er+^{149}Tb(0.167) +^{149}Dy(0.167)+^{149}Ho(0.167)+^{149}Er(0.167)+^{149}Tm(0.167) +^{153}Er(0.088)+^{153}Tm(0.152)+^{153}Yb(0.0835)
^{146}Eu	^{146}Eu+^{146}Gd+^{146}Tb+^{146}Dy+^{146}Ho+^{146}Er+^{146}Tm(0.550) +^{150}Dy(0.360)+^{150}Ho(0.360)+^{150}Er(0.360)+^{150}Tm(0.360) +^{154}Tm(0.158)+^{154}Yb(0.345)+^{154}Lu(0.345)+^{154}Hf(0.345) +^{158}Hf(0.152)+^{158}Ta(0.332)+^{158}W(0.345)+^{162}W(0.071) +^{162}Re(0.316)+^{162}Os(0.345)+^{166}Os(0.051)+^{166}Ir(0.297)
^{147}Eu	^{147}Eu+^{147}Gd+^{147}Tb+^{147}Dy+^{147}Ho+^{147}Er+^{147}Tm(0.900) +^{151}Tb(9.5e-5)+^{151}Dy(0.056)+^{151}Ho(0.264)+^{151}Er(0.264) +^{151}Tm(0.264)+^{151}Yb(0.264)+^{151}Lu(0.185)+^{155}Er(1.23e-5) +^{155}Tm(0.005)+^{155}Yb(0.235)+^{155}Lu(0.258)+^{155}Hf(0.264) +^{159}Lu(2.01e-6)+^{159}Hf(0.097)+^{159}Ta(0.226)+^{159}W(0.264) +^{163}Ta(4.02e-9)+^{163}W(0.040)+^{163}Re(0.159)+^{163}Os(0.264) +^{167}Re(2.81e-11)+^{167}Os(0.027)+^{167}Ir(0.159)+^{171}Ir(2.81e-11) +^{171}Pt(0.026)+^{175}Au(2.64e-11)+^{175}Hg(0.026)
^{148}Eu	^{148}Eu
^{149}Eu	^{149}Eu+^{149}Gd+^{149}Tb(0.833)+^{149}Dy(0.833)+^{149}Ho(0.833) +^{149}Er(0.833)+^{153}Er(0.441)+^{153}Tm(0.798)+^{153}Yb(0.815) +^{157}Lu(0.798)+^{157}Hf(0.813)+^{161}Ta(0.040)+^{161}W(0.674)
^{149}Gd	^{149}Gd+^{149}Tb(0.833)+^{149}Dy(0.833)+^{149}Ho(0.833)+^{149}Er(0.833) +^{153}Er(0.441)+^{153}Tm(0.798)+^{153}Yb(0.815)+^{157}Lu(0.798) +^{157}Hf(0.813)+^{161}Ta(0.040)+^{161}W(0.674)
^{150}Eu	^{150}Eu

(Table C.1 continued)

Cumulative Radionuclide	Sum of Independent Radionuclides and their contribution
^{152}Eu	^{152}Eu
^{151}Gd	^{151}Gd+^{151}Tb+^{151}Dy(0.938)+^{151}Ho(0.732)+^{151}Er(0.732) +^{151}Tm(0.697)+^{151}Yb(0.697)+^{151}Lu(0.488)+^{155}Er(2.06e-4) +^{155}Tm(0.014)+^{155}Yb(0.653)+^{155}Lu(0.688)+^{155}Hf(0.688) +^{159}Lu(5.64e-6)+^{159}Hf(0.268)+^{159}Ta(0.604)+^{163}Ta(1.12e-8) +^{163}W(0.110)+^{163}Re(0.426)
^{153}Gd	^{153}Gd+^{153}Tb+^{153}Dy+^{153}Ho+^{153}Er(0.470)+^{153}Tm(0.042) +^{153}Yb(0.021)+^{157}Yb(0.235)+^{157}Lu(0.223)+^{157}Hf(0.049)
^{167}Tm	^{167}Tm+^{167}Yb+^{167}Lu+^{167}Hf+^{167}Ta+^{167}W+^{167}Re+^{167}Os(0.33) +^{171}Pt(0.337)+^{171}Ir+^{171}Os(0.017)+^{175}Pt(0.011)+^{175}Au(0.94) +^{175}Hg(0.337)+^{179}Hg(0.006)
^{168}Tm	^{168}Tm
^{169}Yb	^{169}Yb+^{169}Lu+^{169}Hf+^{169}Ta+^{169}W+^{169}Re+^{169}Os(0.890) +^{173}Os(2.1e-4)+^{173}Ir(0.070)+^{173}Pt(0.759)+^{177}Pt(1.18e-5) +^{177}Au(0.028)+^{177}Hg(0.649)+^{181}Hg(4.23e-6)
^{171}Lu	^{171}Lu+^{171}Hf+^{171}Ta+^{171}W+^{171}Re+^{171}Os(0.983)+^{175}Ir(0.0085) +^{175}Pt(0.629)
^{172}Lu	^{172}Lu+^{172}Hf+^{172}Ta+^{172}W+^{172}Re+^{172}Os(0.990)+^{172}Ir(0.970) +^{172}Pt(0.058)+^{176}Ir(0.021)+^{176}Pt(0.990)+^{176}Au(0.970) +^{176}Hg(0.058)+^{180}Au(3.78e-4)+^{180}Hg(0.475)
^{172}Hf	^{172}Hf+^{172}Ta+^{172}W+^{172}Re+^{172}Os(0.990)+^{172}Ir(0.970) +^{172}Pt(0.058)+^{176}Ir(0.021)+^{176}Pt(0.990)+^{176}Au(0.970) +^{176}Hg(0.058)+^{180}Au(3.78e-4)+^{180}Hg(0.475)
^{173}Lu	^{173}Lu+^{173}Hf+^{173}Ta+^{173}W+^{173}Re+^{173}Os+^{173}Ir(0.93) +^{173}Pt(0.149)+^{177}Pt(0.113)+^{177}Ir(0.060)+^{177}Au(0.440) +^{177}Hg(0.192)+^{181}Au(7.8e-4)+^{181}Hg(0.041)
^{174}Lu	^{174}Lu
^{175}Hf	^{175}Hf+^{175}Ta+^{175}W+^{175}Re+^{175}Os+^{175}Ir+^{175}Pt+^{179}Pt(0.0024) +^{179}Au(0.222)+^{179}Hg(0.634)
^{181}Hf	^{181}Hf+^{181}Lu+^{181}Yb
^{182}Ta	^{182}Ta+^{182}Hf+^{182}Lu

(Table C.1 continued)

Cumulative Radionuclide	Sum of Independent Radionuclides and their contribution
^{183}Ta	^{183}Ta+^{183}Hf+^{183}Lu
^{183}Re	^{183}Re+^{183}Os+^{183}Ir+^{183}Pt+^{183}Au(0.997)+^{183}Hg(0.880)
^{184}Re	^{184}Re
^{185}Os	^{185}Os+^{185}Ir+^{185}Pt+^{185}Au+^{185}Hg(0.94)
^{189}Ir	^{189}Ir+^{189}Pt+^{189}Au+^{189}Hg
^{190}Ir	^{190}Ir
^{192}Ir	^{192}Ir
^{188}Pt	^{188}Pt+^{188}Au+^{188}Hg
^{195}Au	^{195}Au+^{195}Hg
^{196}Au	^{196}Au

REFERENCES

[1] Jim Clow, Robin DeVore, John Elder, George Heindel, William Inkret, Guthrie Miller, "Specific Activities and DOE-STD-1027-92, Hazard Category 2 Thresholds," DOE Technical Standard DOE-STD-1027-92, 1992.

[2] Bruce Takala "WNR Target-4 Nuclide Inventory Control," LANL Report, LANSCE-3-ROP-20, 2002.

[3] Jeffrey S. Bull, Joey B. Donahue, David Fuehne, Floyd Gallegos, Kevin Jones, George Heindel, Roger Klaffky, Cetin Unal, Richard D. Werbeck, "Basis for Interim Operation (BIO) for the 1L Target, 2000-2002 Beam Delivery Periods," LANL Report 53-BIO-004, Rev.2, 2000.

[4] Jeffrey S. Bull, LANL Internal Report CN-LANSCEFM-00-001, 2000.

[5] Jeffrey S. Bull, "1L Target Isotope Inventory Calculation Procedure," LANL Report, LANSCE-7-OP-1-10.00, 2000.

[6] L. S. Waters, Ed., "MCNPX User's Manual, Version 2.4.0," LANL Report, LA-CP-02-408, 2002.

[7] S. G. Mashnik, K. K. Gudima, A. J. Sierk, "Merging the CEM2k and LAQGSM Codes with GEM2 to Describe Fission and Light-Fragment Production," LANL Report, LA-UR-03-2261, 2003.

[8] S. G. Mashnik, A. J. Sierk, K. K. Gudima, "Complex Particle and Light Fragment Emission in the Cascade-Exciton Model of Nuclear Reactions," LANL Report, LA-UR-02-0608, 2002.

[9] J. F. Briesmeister, Ed., "MCNP4B-A General Monte Carlo N-Particle Transport Code," LANL Report, LA-12625-M, 1997.

[10] R. E. Prael and H. Lichtenstein, "User Guide to LCS: The LAHET Code System," LANL Report, LA-UR-89-3014, 1989.

[11] M. B. Chadwick, P. G. Young, S. Chiba, S. C. Frankle, G. M. Hale, H. G. Hughes, A. J. Koning, R. C. Little, R. E. MacFarlane, R. E. Prael, and L. S. Waters, "Cross-section Evaluations to 150 MeV for Accelerator-Driven Systems and Implementation in MCNPX," *Nuclear Science and Engineering* 131, 1999, 293-328.

[12] Hugo W. Bertini, "Low-Energy Intranuclear Cascade Calculation," *Physical Review* 131(4), 1963, 1801-1821.

[13] Hugo W. Bertini, " Intranuclear-Cascade Calculation of the Secondary Nucleon Spectra from Nucleon-Nucleus Interactions in the Energy Range 340 to 2900 MeV and Comparisons with Experiment," *Physical Review* 188(4), 1969, 1711-1730.

[14] R. E. Prael and Michael Bozoian, "Adaptation of the Multistage Preequilibrium Model for the Monte Carlo Method," LANL Report, LA-UR-88-3238, 1988.

[15] R. E. Prael, "A Review of Physics Models in the LAHET Code," *Intermediate Energy Nuclear Data: Models and Codes, Prodceedings of a Specialists' Meeting*, OECD, 1994, 145.

[16] F. Atchison, "Spallation and Fission in Heavy Metal Nuclei under Medium Energy Proton Bombardment," *Targets for Neutron Beam Spallation Sources* Jül-Conf-34, Kernforschungsanlage Jülich GmbH, 1980.

[17] S. Furihata, "The GEM code–A Simulation Program for the Evaporation and Fission Process of an Excited Nucleus," JAERI-Data/Code 2001-015, JAERI, 2001.

[18] K. K. Gudima, S. G. Mashnik, V. D. Toneev, "Cascade-exciton model for nuclear reactions," *Nuclear Physics* A401, 1983, 329-361.

[19] S. G. Mashnik and V. D. Toneev, "MODEX-the Program for Calculation of the Energy Spectra of Particles Emitted in the Reactions of Pre-Equilibrium and Equilibrium Statistical Decays," Communications of the Joint Institute for Nuclear Research, P4-8417, Dubna, 1974.

[20] A. V. Ignatyuk, G. N. Smirenkin, A. S. Tishin, "Phenomenological description of energy dependence of the level density parameter," *Soviet Journal of Nuclear Physics* 21(3), 1975, 485-490.

[21] Arnold J. Sierk and Stepan G. Mashnik,"Modeling Fission in the Cascade-Exciton Model," *Proceedings of the Fourth Workshop on Simulating Accelerator Radiation Environments (SARE4)*, 1998, 53-67.

[22] D. L. Quintana, R. L. Barber, M. J. Baumgartner, R. D. Brown, J. N. Edwards, B. A. Faulkner, T. L. Figueroa, J. J. Jarmer, R. Kidman, P. D. Olivas, M. A. Paciotti, L. S. Waters, R. D. Werbeck, G. J. Willcutt, K. A. Woloshun, "Measurement of Radioactive Decay Heat in a Tungsten Target Irradiated by a High-Power Proton Beam," *Proceedings of the Fourth International Topical Meeting on Nuclear Applications of Accelerator Technology*, American Nuclear Society 2000, 405-414.

[23] E. A. Henry and K. J. Moody, "Decay Heat and Spallation Product Yields from Thin Tungsten Foils," APT Internal Report, LLNL 1999.

[24] Y. E. Titarenko, "Experimental and Theoretical Study of the Yields of Residual Product Nuclei Produced in Thin Targets Irradiated by 100-2600 MeV Protons," Technical Report of ISTC 839B-99, 2001.

[25] J. L. Ullmann, A. Gavron, J. King, R. Laird, D. Mayo, L. Waters, C. Zoeller, P. Staples, D. Jagnow, J. Koster, P. W. Lisowski, R. O. Nelson, S. A. Wender, G. Butler, R. Gritzo, M. A. Yates, M. Fowler, J. Wilhelmy, W. Wilson, C. E. Laird, D. H. Mullins, "APT Radionuclide Production Experiment Technical Report," LANL Report LA-UR-95-3327, 1995.

[26] Johanna Sabine Becker, Wolfgang Kerl, Hans-Joachim Dietze, "Nuclide analysis of an irradiated tantalum target of a spallation neutron source using high performance

ion chromatography and inductively coupled plasma mass spectrometry," *Analytica Chimica Acta* 387, 1999, 145-154.

[27] S. A. Karamian, J. Adam, D. V. Filossofov, D. Henzlova, V. Henzl, V. G. Kalinnikov, N. A. Lebedev, A. F. Novgorodov, C. B. Collins, I. I. Popescu, C. A. Ur, "Accumulation of the ^{178m2}Hf isomeric nuclei through spallation with intermediate-energy protons of tantalum and rhenium targets," *Nuclear Instruments and Methods in Physics Research A*489, 2002 448-468.

[28] J. Benlliure, P. Armbruster, M. Bernas, A. Boudard, J. P. Dufour, T. Enqvist, R. Legrain, S. Leray, B. Mustapha, F. Rejmund, K. -H. Schmidt, C. Stéphan, L. Tassan-Got, C. Volant, "Isotopic production cross sections of fission residues in ^{197}Au-on-proton collisions at 800 *A* MeV," *Nuclear Physics A* 683, 2001 513-539.

[29] F. Rejmund, B. Mustapha, P. Armbruster, J. Benlliure, M. Bernas, A. Boudard, J. P. Dufour, T. Enqvist, R. Legrain, S. Leray, K. -H. Schmidt, C. Stéphan, J. Taieb, L. Tassan-Got, C. Volant, "Measurement of isotopic cross sections of spallation residues in 800 *A* MeV ^{197}Au+p collisions," *Nuclear Physics A* 683, 2001, pp. 540-565.

[30] R. Michel, R. Bodemann, H. Busemann, R. Daunke, M. Gloris, H. -J. Lange, B. Klug, A. Krins, I. Leya, M. Lüpke, S. Neumann, H. Reinhardt, M. Schnatz-Büttgen, U. Herpers, Th. Schiekel, F. Sudbrock, B. Holmqvist, H. Condé, P. Malmborg, M. Suter, B. Dittrich-Hannen, P. -W. Kubik, H. -A. Synal, D. Filges, "Cross sections for the production of residual nuclides by low- and medium-energy protons from the target elements C, N, O, Mg, Al, Si, Ca, Ti, V, Mn, Fe, Co, Ni, Cu, Sr, Y, Zr, Nb, Ba and Au," *Nuclear Instruments and Methods in Physics Research B* 129, 1997, pp. 153-193.

[31] Y. Asano, S. Mori, M. Noguchi, M. Sakano, K. Katoh, K. Kondo, "Spallation and fission yields in the interactions of tantalum, tungsten, and gold with 500-MeV protons," *Journal of the Physical Society of Japan* 54(10), 1985, pp.3734-41.

[32] Von E. Ross, K. Bachmann, "Fission of gold with 580-MeV protons," *Radiochimica Acta* 21(1-2), 1974, pp. 13-20.

[33] R. Michel, B. Dittrich, U. Herpers, F. Peiffer, T. Schiffmann, P. Cloth, P. Dragovitsch, D. Filges, "Proton-induced spallation at 600 MeV," *Analyst* 114, 1989, 89.

[34] Yu. E. Titarenko, V. F. Batyaev, V. M. Zhivun, A. B. Koldobsky, Yu. V. Trebukhovsky, E. I. Karpikhin, R. D. Mulambetov, S. V. Mulambetova, Yu. V. Nekrasov, A. Yu Titeranko, K. A. Lipatov, S. G. Mashnik, R. E. Prael, K. Gudima, M. Baznat, "Cross Sections for Nuclide Production in 1 GeV Proton-Irradiated ^{208}Pb and 0.8 GeV Proton-Irradiated ^{197}Au," *Proceedings of the Sixth International Meeting on Nuclear Applications of Accelerator Technology, Accelerator Applications in a Nuclear Renaissance*, American Nuclear Society 2003.

[35] Stepan G. Mashnik, Richard E. Prael, Arnold J. Sierk, Vyacheslav F. Batyaev, Svetlana V. Kvasova, Ruslan D. Mulambetov, and Yury E. Titeranko, "Benchmarking Ten Codes Against the Recent GSI Measurements of the Nuclide Yields from ^{208}Pb, ^{197}Au, and ^{238}U + p Reactions at 1 GeV/nucleon," LANL Report, LA-UR-01-5391, 2001.

[36] G. Friedlander, J. Hudis, and R. L. Wolfgang, "Disintegration of Aluminum by Protons in the Energy Range 0.4 to 3.0 BeV," *Physical Review* 99(1), 1955, p. 263.

[37] J. E. Cline and E. B. Nieschmidt, "Measurements of spallation cross sections for 590 MeV protons on thin targets of copper, nickel, iron, and aluminum," *Nuclear Physics A*169, 1971, pp. 437-448.

[38] J. Tobailem, "Sections Efficaces des Reactions Nucleaires Indutes par Protons, Deuterons, Particles Alphas. V. Silicium," Report CEA-N-1466(5), Saclay, 1981.

[39] A. Grütter, "Cross Sections for Reactions with 593 and 540 MeV Protons in Aluminum, Arsenic, Bromine, Rubidium and Yttrium," *International Journal of Applied Radiation and Isotopes* 33(9), 1982, pp. 725-732.

[40] G. L. Morgan, K. R. Alrick, A. Saunders, F. C. Cverna, N. S. P. King, F. E. Merrill, L. S. Waters, A. S. Carroll, A. L. Hanson, R. P. Liljestrand, R. T. Thompson, E. A. Henry, "Total cross sections for production of ^{22}Na and ^{24}Na in proton-induced reactions on ^{27}Al from 0.4 to 22 GeV," *Nuclear Instruments and Methods in Physics Research B* 211, 2003, pp. 297-304.

[41] R. Michel, M. Gloris, H. -J. Lange, I. Leya, M. Lüpke, U. Herpers, B. Dittrich-Hannen, R. Rösel, Th. Schiekel, D. Filges, P. Dragovitsch, M. Suter, H. -J. Hofmann, W. Wölfli, P. W. Kubik, H. Baur, R. Wieler, "Nuclide production by proton-induced reactions on elements ($6 \leq Z \leq 29$) in the energy range from 800 to 2600 MeV," *Nuclear Instruments and Methods in Physics Research B* 103, 1995, pp. 183-222.

[42] T. N. Taddeucci, J. Ullmann, L. J. Rybarcyk, G. W. Butler, T. E. Ward, "Total cross sections for production of ^{7}Be, ^{22}Na, and ^{24}Na in p+^{7}Li and p+^{27}Al reactions at 495 and 795 MeV," *Physical Review C* 55, 1997, pp. 1551-1554.

[43] H. R. Heydegger, Anthony L. Turkevich, A. Van Ginneken, P. H. Walpole, "Production of ^{7}Be, ^{22}Na, and ^{28}Mg, from Mg, Al, and SiO_2 by protons between 82 and 800 MeV," *Physical Review C* 14(4), 1976, pp. 1506-1514.

[44] G. I. Krupnyi, D. V. Snitko, A. A. Yanovich, "Cross sections of the reactions ^{27}Al(p,*spall*)^{7}Be, ^{27}Al(p,*3p3n*)^{22}Na, and ^{27}Al(p,*3pn*)^{24}Na in the proton energy range 37 MeV-70 GeV," *Atomic Energy* 89(5), 2000, pp. 939-941.

[45] H. Vonach, A. Pavlik, A. Wallner, M. Drosg, R. C. Haight, D. M. Drake, S. Chiba, "Spallation reactions in ^{27}Al and ^{56}Fe induced by 800 MeV protons," *Physical Review C* 55(5), 1997, pp. 2458-2467.

[46] G. M. Raisbeck and F. Yiou, "Cross sections for the spallation production of ^{10}Be in targets of N, Mg, and Si and their astrophysical applications," *Physical Review C* 9(4), 1974, pp. 1385-1395.

[47] J. F. Ziegler and J. P. Biersack, "SRIM–The stopping and range of ions in matter," SRIM version 2000.40, 2000. SRIM website http://www.srim.org

[48] "ORTEC-Introduction to Charged-Particle Detectors," ORTEC website, http://www.ortec-online.com/detectors/chargedparticle/sel_guide.htm.

[49] "ORTEC ULTRA and ULTRA-AS Ion-Implanted-Silicon Charged-Particle Detectors," ORTEC website, http://www.ortec-online.com/detectors/chargedparticle/ultra.htm.

[50] "B2.2 ORTEC Detector Element–GAMMA-X HPGe Coaxial Detectors," ORTEC website, http://www.ortec-online.com/detectors/photon/b2_2.htm.

[51] "Efficiency as a function of energy," ORTEC website, http://www.ortec-online.com/detectors/photon/a5a.htm.

[52] E. Wayne Killian and Jack K. Hartwell, "PCGAP: Users Guide and Algorithm Description," INEEL Report, INEEL/EXT-2000-00908, 2000.

[53] S. Y. F. Chu, L. P. Ekstrom, and R. B. Firestone, "The Lund/LBNL Nuclear Data Search, Version 2.0," http://nucleardata.nuclear.lu.se/nucleardata/toi/, 1999.

[54] Chris Worley, private communication, 2003.BNL Nuclear Data Search Version 2.0, February 1999.